THUTO KE THEBE

UNIVERSITY
of
BOTSWANA

FACULTY OF ENGINEERING AND TECHNOLOGY

DEPARTMENT OF MECHANICAL ENGINEERING

CHARACTERISTIC INFLUENCE OF THERMO-MECHANICAL STRESSES LEADING TO PREMATURE FAILURE OF COMPRESSOR TURBINE BLADES OF SHORT-HAUL AIRCRAFT FLEET

JOSHUA KIMTAI NGORET

STUDENT ID: 201501995

SUPERVISOR: PROF. VENKATA PARASURAM KOMMULA

A THESIS SUBMITTED IN FULFILLMENT OF THE REQUIREMENTS FOR DEGREE
OF
DOCTOR OF PHILOSOPHY IN ENGINEERING
AT THE UNIVERSITY OF BOTSWANA

26TH FEBRUARY, 2019

CERTIFICATION

The undersigned certifies that he has read and guided the work, and hereby recommends for acceptance by the Department of Mechanical Engineering the thesis titled, “**Characteristic influence of thermo-mechanical stresses leading to premature failure of compressor turbine (CT) blades of short-haul aircraft fleet**”, as part of the requisite work in fulfillment of the requirements for the degree of Doctor of Philosophy in Engineering at the University of Botswana.

…………………………….	…………………….….
Signature (Supervisor)	Date

STATEMENT OF ORIGINALITY

I, Joshua Kimtai Ngoret, hereby declare to the best of my knowledge, that all the work reported in this thesis for award of Doctor of Philosophy in Engineering at the University of Botswana, is my own original research both in conception and execution, and that I have not received any assistance from elsewhere apart from the normal guidance from my supervisor and that acknowledged. No material contained herein has been previously submitted or presented for examination in the University of Botswana or any other institution for award of any degree.

………………………….	…………………….....
Signature	Date

DEDICATION

To my family.

ACKNOWLEDGEMENTS

First and foremost, glory goes to The Almighty God, that by His grace and love, I have successfully completed this research task I set to accomplish.

My heartfelt gratitude goes to my advisor Prof. Ing. V. P. Kommula, Associate Professor and Programs Coordinator for Industrial Engineering, University of Botswana for his consistent thoughtfulness and invaluable guidance throughout all the stages of my research and thesis writing.

My deepest appreciation goes to Mobility to Enhance Training of Engineering Graduates in Africa (METEGA) for the scholarship grant not only to me, but, to a number of other engineering postgraduate students spread out throughout Africa under their sponsorship.

I wish to specially acknowledge, two institutions; University of Botswana (UB) – the host, and more specifically, the Faculty of Engineering and Technology (FET) for providing the conducive and enabling environment to make it possible for me to work diligently until the completion of my research. My heartfelt appreciations go to The Office of Research and Development (ORD) which was instrumental in funding of my experiments and publications. The second institution, Jomo Kenyatta University of Agriculture and Technology (JKUAT) – the origin, for granting me ample study leave to enable me uninterruptedly pursue this research.

I want to sincerely thank Vector Aerospace Kenya Limited, for enabling me to collect samples and data from their premises.

Finally, sincere thanks go to my fellow colleagues undertaking different research interests in PhD, FET for their consistent friendship, assistance, encouragement when the going seemed tough and support as we toiled together.

SYNOPSIS

Short-haul aircrafts play an integral role in air transport network, facilitating; passenger and cargo transport, security drills, ambulance services, disaster, wildlife and environment management, tourism amongst others. Unlike medium and long-hauls, these aircrafts are missioned to fly for under 3 hours and distances not exceeding 2000 km. As a result of short but, voluminous flight turnovers, changes in power settings, starts and stops; the compressor turbine (CT) blades of the engines are subjected to intense cyclic thermo-mechanical stresses.

Compressor turbine blades are specially profiled aerodynamic engine components specially designed to extract energy from high-temperature, high-pressure gases produced by the combustors. Due to severity of their operational environment, the CT blades degrade over time and often catastrophically fail without warning. In this regard, monitoring of CT blade life is crucial to ensure their proper health in service.

The current techniques employed to investigate the life of CT blades only inform of failure after exposure to service with scanty information on the numerous prematurely occurring failures. Consequently, accounting for CT blade life still poses a great challenge to air operators. This research therefore probed characteristic influence of thermo-mechanical stresses leading to premature failure of high pressure (HP), PT6A-114A engine CT blades from an assimilative approach. The prematurely retired HP, CT blades were collected from Vector Aerospace Kenya Limited after being in service for only 6378 creep-fatigue hours contrary to 10000 creep-fatigue hours preset by the manufacturer.

The CT blade was modeled for thermo-mechanical degradation in an environment that mimics the operational conditions to determine service life and resulting damage using commercial ANSYS tools version 15.0. A detailed microstructural and metallographic characterization was then performed using x-ray florescence (XRF), x-ray diffraction (XRD) and energy dispersive spectroscope-scanning electron microscopy (EDS-SEM) on the protective coating and the substrate material. Mechanical testing was ultimately executed to ascertain the micro hardness and residual strength at time of retire from service.

The modeling results revealed that the tip of the CT blade had been rigorously attacked by exposure to heat as compared to the airfoil and the base. Notwithstanding this, it was noted that the CT blade could have served for another 1.44% more of the time it was in service, being exploited in the transient regime. The XRF results affirmed the existence of the bulk constituent elements that matched the manufacturers' specification. The XRD analyses enabled positive identification of the resultant compounds which constituted the protective coating and the substrate material. The EDS-SEM results established that the protective coating of the tips was more attacked compared to the airfoils and the bases. As such, the substrate material degraded from evolution of creep and fatigue. The pores at the bases of the CT blades were found not influence distribution of uniform cuboidal phase at the bases in comparison the rafted tips and airfoils. This confirmed that degradation of the substrate material occurred as a result of creep and fatigue and not from manufacturing defects. Though micro hardness testing indicated that the material was still of high strength, continued safe service was not warrantied.

From this research, a robust assimilative approach was adopted for investigating life of CT blades enabling determination of instantaneous material status, magnitude of damage and remaining useful life (RUL). This work will assist air operators improve flight safety, enhance availability of aircrafts for operations while planning for maintenance will be made easier.

Premature failure of the CT blades can further be averted by; adhering to the engine's operation limits, avoiding long and overexploitation of the engine and sticking to preset flight environments. In a move to improve heat, oxidation and corrosion resistance of the protective coating, inclusion of rare earth element such as yttrium, cesium and lanthanum would be noble. The substrate material could similarly be improved by addition of refractory elements such as ruthenium, iridium and rhenium in the composition of Inconel 713LC.

ARTICLES PUBLISHED FROM THIS RESEARCH

1. Ngoret, J. K., & Kommula, V. P. (2016, May). Monitoring Material Degradation in Aircraft Turbine Blades: A Comprehensive Survey on Current Techniques. *Proceedings of Sustainable Research and Innovation (SRI) Conference, 4-6th May 2016*, pp. 21-29. (https://doi.org/10.5281/zenodo.1247445).
2. Ngoret, J. K., & Kommula, V. P. Influence of Thermal Stress on the Strength of Compressor Turbine (CT) Blades of Short-Haul Aircraft Fleet. *Botswana Institution of Engineers (BIE) 15th International Biennial Conference, Gaborone, Botswana, 17-19th October 2017.*
3. Ngoret, J. K., & Kommula, V. P. Extended Abstract: Role of Aluminide coating degradation on Inconel 713 LC used for Compressor Turbines (CT) of Short-haul Aircrafts. *9th International Conference of the African Materials Research Society (AMRS2017) Gaborone, Botswana, 11-14th December 2017.*
4. Ngoret, J. K, & Kommula, V. P. (2018). Role of Aluminide coating degradation on Inconel 713 LC used for Compressor Turbines (CT) of Short-haul Aircrafts. MRS Advances, 1-16. (https://doi.org/10.1557/adv.2018.207).
5. Ngoret, J. K, & Kommula, V. P. (2018, February). Microstructural Investigation into Premature Failure of Compressor Turbine (CT) Blade Material of PT6A-114A Engine. Article code: A-10-1676-1 (Iranian Journal of Materials Science and Engineering).
6. Ngoret, J. K, & Kommula, V. P. Modeling Premature Failure of Compressor Turbine (CT) Blades for Short-Haul Aircraft Fleet (In Press - International Journal of Engineering Research in Africa).
7. Ngoret, J. K, & Kommula, V. P. Study of Damage Evolution in Compressor Turbine (CT) Blades of Short-Haul Aircraft Fleet under Thermo-Mechanical Stresses.

Proceedings of SADC International Conference on Postgraduate Research for Sustainable Development, Gaborone, Botswana, October 28-31st, 2018.

8. Ngoret, J. K., & Kommula, V. P. (2018, May). Importance of Quality Sample Preparation for Microstructural and Metallurgical Analyses: Inconel 713 LC used for Compressor Turbine Blades of Short-Haul Aircrafts. *Sustainable Research and Innovation (SRI) Conference, Jomo Kenyatta University of Agriculture and Technology (JKUAT) Main Campus, 8-10th May 2019.*

TABLE OF CONTENTS

LIST OF FIGURES

LIST OF TABLES

LIST OF ABBREVIATIONS AND NOTATIONS

Acronyms	**Expansion**
Al	Aluminium
Al_2O_3	Aluminium Oxide
ASTM	American Society for Testing and Materials
BHSI	Borescope Hot Section Inspection
B	Boron
C	Carbon
^{0}C	Celsius Degree
Co	Cobalt
Cr	Chromium
Cr_2O_3	Chromium Oxide
CT	Compressor Turbine
Cu	Copper
EDS	Energy Dispersive Spectroscopy
Eq.	Equation
Fe	Iron
FE	Finite Element
Fig.	Figure
HP	High Pressure
HSI	Hot Section Inspection
MPa	Mega Pascal
Mo	Molybdenum
Na	Sodium
Nb	Niobium
Ni	Nickel
Ni_2Al_3	Nickel Aluminium Intermetallic
OVH	Overhaul
O_2	Oxygen
Pt	Platinum
RUL	Remaining Useful Life
S	Sulphur
SEM	Scanning Electron Microscope

Si	Silicon
STP	Standard Temperature and Pressure
Ti	Titanium
XRD	X-ray Diffraction
XRF	X-yay Fluorescent
V	Vanadium
Zr	Zirconium
$\beta - NiAl$	Nickel Aluminium diffusion phase

CHAPTER 1: INTRODUCTION

1.1. Preamble

This chapter briefly describes the Compressor Turbine (CT) blade assembly, the CT blade and their respective roles. It discusses the materials used in manufacture of the CT blades, the composition as well as function of the constituent elements of the substrate material, Inconel 713LC and the protective coating. Finally, it sheds light on mechanisms that degrade of the CT blades while in service.

1.2. CT assembly of short-haul aircraft engines

Modern aircraft engines are classified as; turbofan, turbojet, turboprop, or turboshaft. Though these engine designs and utilization could be uniquely different, their principle of operation is virtually similar (El-Sayed, 2017). A turboprop engine shown in Fig. 1.1 (Pratt&Whitney, 2014) is used for short-haul aircraft fleet due to its capability to take-off and land on relatively shorter runways. This type of engine comprises of a gas generator assembly (CT section), whose key function is to generate and convert high pressure, high velocity gases into kinetic energy, while the power section assembly rotates the propellers with the help of the reduction gear boxes to thrust the aircraft forward.

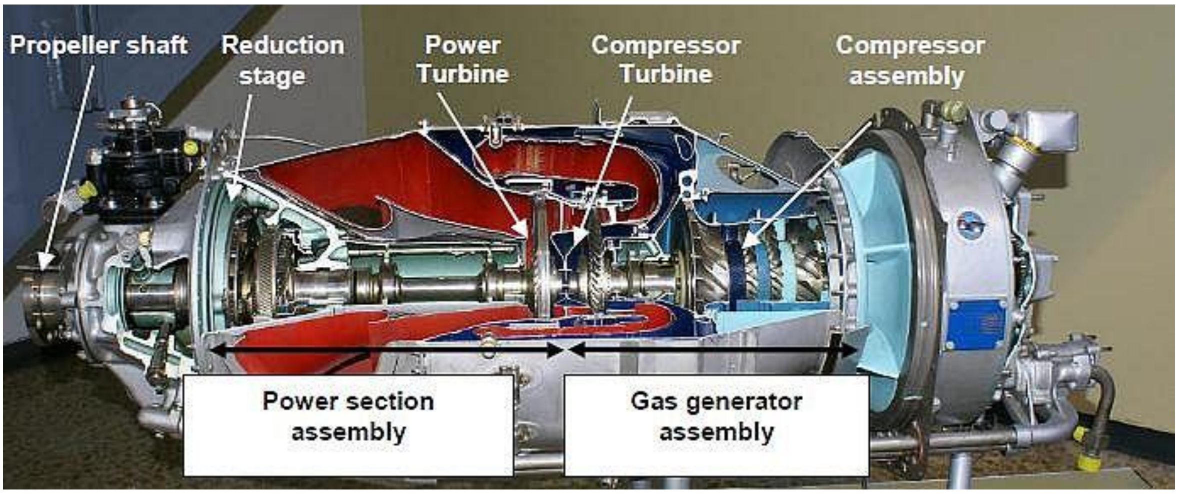

Figure 1. 1: PT6A-114A engine (Source: Pratt & Whitney, 2014)

A typical CT assembly appearing in Fig. 1.2 (Pratt&Whitney, 2014) is a turbo-machine that revolves a rotor which is responsible for engaging and disengaging the power turbine to drive the propellers. The assembly constitutes of CT blades that rotate along with the shaft and vanes which are stationery in alternating rows (Mattingly, 2002).

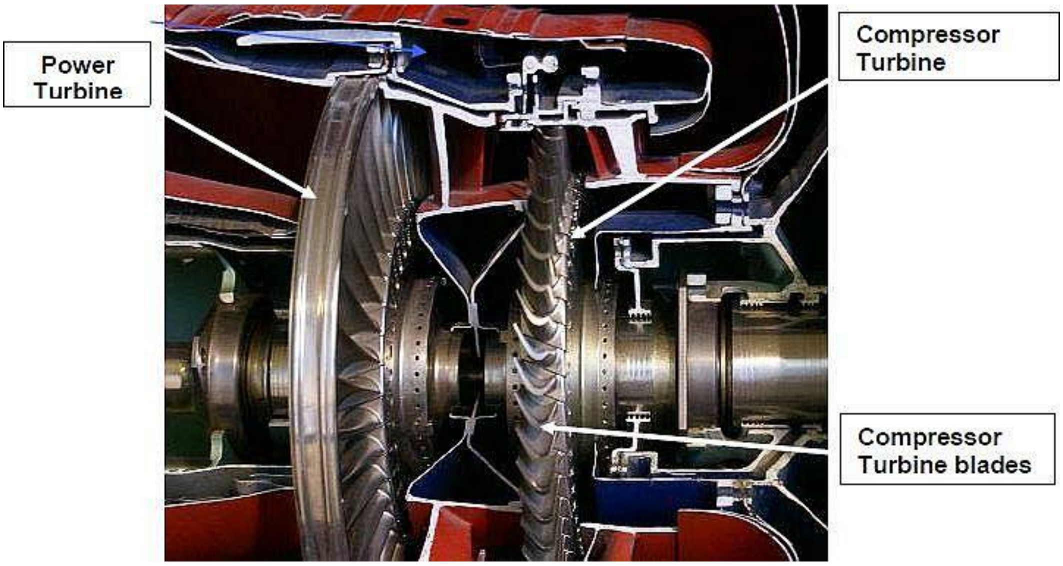

Figure 1. 2: The CT section (Source: Pratt & Whitney, 2014)

Figs. 1.3 and 1.4 represent a section of the CT blade assembly and a CT blade respectively (Aero Assurance, 2015). The CT blades are firmly attached and locked onto the rotor with the aid of the fir tree root connections. When an engine is started, the CT blades are rotated with the help of an auxiliary power unit, pneumatic or an electrical stator. Since the CT assembly and the compressor are connected of the same shaft, the compressor is then capable of drawing sufficient air by itself to sustain continuous combustion. The CT blades on the other hand are specially profiled aerodynamic turbine components capable of reactively or impulsively extracting energy from the high-temperature, high-pressure gases produced by the combustors as they impinge and rotate them. The number of CT blades on the assembly varies from engine to another with a typical PT6A-114A engine having 58 HP CT blades.

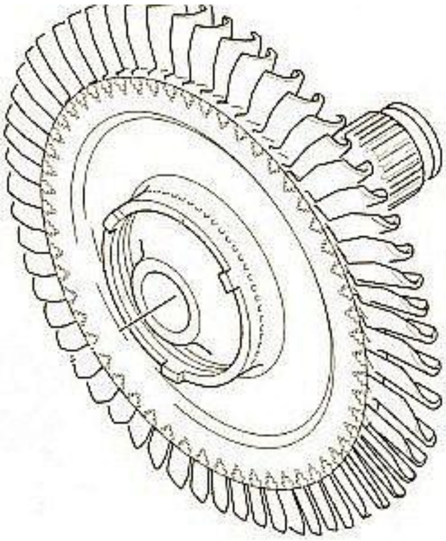

Figure 1. 3: The CT blade assembly (Source: Aero Assurance, 2015)

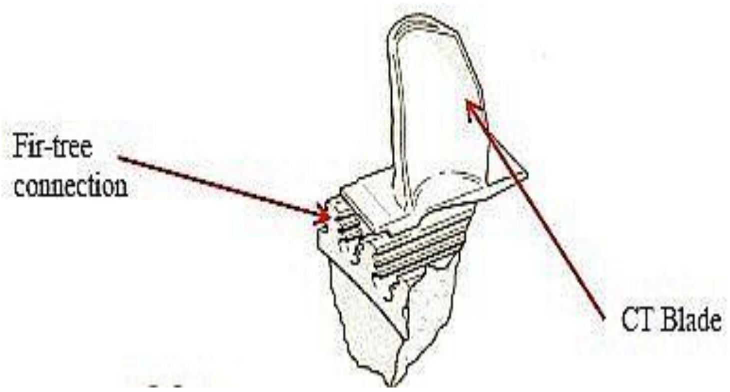

Figure 1. 4: The CT blade (Source: Aero Assurance, 2015)

1.3. Materials for CT blades

Predominantly, the earlier CT blades were manufactured from Cu-base alloys used for British whittle engines. With advances in technology however, Ni-base super alloys have become popular owing to their; high strength, toughness, the ability to form stable alloys without phase instability, little attack from atmospheric elements as well as high corrosion and oxidation resistance at elevated temperatures. In current research, polycrystalline Ni-base super alloy, Inconel 713LC, whose composition is recorded in Table 1.1 is utilized in manufacture of PT6A-114A engine CT blades.

Table 1. 1: Elemental Composition of Inconel 713LC by % mass (Zielińska et al., 2011)

Ni	Al	Cr	Ti	Mo	Fe	C	B	P	S	Nb	Zr
74	6.1	12.5	0.8	4.2	-	0.05	0.012	0.006	0.004	2.1	0.1

The constituent elements of the Inconel 713LC listed on Table 1.1 play the following vital roles.

1.3.1. γ Solid solution strengtheners

The primary aim of these elements is to increase resistance to dislocations. When the material is subjected to temperature rise, these elements develop lower diffusivity in Ni, as a result creep resistance is augmented (Durand-Charre, 2017). In Inconel 713LC, Mo improves resistance against non-oxidizing acids, pitting and crevice corrosions while impacting strength to the alloy at elevated temperatures. It however significantly reduces the material's density. Cr is a good strength enhancer, an oxidation and sulphidation inhibitor. Owing to its good solubility in Ni, solid solution hardening is boosted by the ease with which it precipitates into intergranular carbides. With admirable strength and creep resistant properties, Co is a perfect inhibitor to carburization and sulphidation as it increases solubility of C in Ni (Balikci et al., 2000).

1.3.2. γ' Precipitate formers

Niobium (Nb) is a key refractory grain boundary strengthener in the γ'solvus phase and serves to increases the material's yield strength and density compromised by Mo (Wu et al., 2014). It presence nonetheless, accelerates the rate of fatigue crack growth (Smith et al., 2005). Aluminium (Al) is well known for resistance to oxidation and oxide spalling (Yeh, 2013), carburization, chlorine attack, increases adherence and the volume of the alloys γ' phase at elevated temperature (Durand-Charre, 2017). However, too much of the γ'solvus phase weakens the material.

1.3.3. Carbide formers

Presences of carbides improve the material's corrosion and creep resistance at elevated temperatures besides preventing grain-boundary sliding and migration. Carbides however compromise the material's ductility, rendering it susceptible to cracking (Qin et al., 2007). In Inconel 713LC, Ti, Cr and Nb play this role and in turn promotes age hardening. Being a high

Cr content Ni-based alloy, formation of $M_{23}C_6$ is inevitable from the reaction $MC + \gamma \rightarrow M_{23}C_6 + \gamma'$ at the grain boundaries (Liu et al., 2003; Pollock et al., 2002; Qin, Guo, Yuan, Chen, et al., 2008); where M is the carbide former. Titanium (Ti) also actively combines with carbon to reduce intergranular corrosion arising from carbides of Cr.

1.3.4. Phase stabilizers

Phase stabilizers are classified as either external or internal. External stabilizers protect the alloy from oxidation when exposed to high temperatures in the presence of O_2, S, Na, Va or other contaminants that may occasion hot corrosion (Yoo et al., 2010). Addition of Cr into the material leads to oxide formation which inhibits oxidation and hot corrosion attacks while allowing S to readily diffuse in it than in Ni at elevated temperatures (Locq et al., 2011; Talbot et al., 2018). At temperatures of about 950°C, Al further compliments Cr by exhibiting better oxidation resistance, as Cr_2O_3 tends to turn gaseous (Li et al., 2013). Internal stabilizers are primarily $M_{23}C_6$ whose key function is to check sliding and migration of grain boundaries at elevated temperatures. Boron (B) segregates to the grain boundaries decelerating formation of $M_{23}C_6$ carbides (Yan et al., 2008). This leads to improving the alloys ductility, cushioning against premature cracking and lengthen rupture life at elevated temperatures (Kontis et al., 2016). Inclusion of Nb appreciably decreases the amount of $M_{23}C_6$ carbide formation best known for making the material brittle, increasing the tendency to cracking (Barbosa et al., 2005; Qin, Guo, Yuan, Hou, et al., 2008). As Cr depletes within the material, undesirable grain boundary carbides form with an increase in solubility of precipitates which potentially compromise the strength of the alloy. Boron (B) once again comes in handy to retard this. Zirconium (Zr) also serves to counter potential weakening of the material from presence of S in fuels and operational environment. It however, has to be checked to avoid formation of phases with low melting points. Presence of Mo as a refractory material counters acid attacks but, quickly leads to formation of M_6C carbides as depicted by the expression $MC + \gamma \rightarrow M_6C + \gamma'$ (Qin et al., 2012).

1.3.5. Protective coatings

Other than the elements constituting the substrate material, the protective coatings play a vital role in guarding the material from high temperature oxidation, hot corrosion, attack by chemical constituents in the fuel and the environment in which the engine operates (Becker et al., 2002; Zielińska et al., 2011). Evolution, development and application of protective surface coatings for hot engine sections dates back to the early 1980s (Muktinutalapati, 2011). Protective coatings are thus classified as; diffusion, overlay, thermal barrier and smart coatings.

1.3.5.1. Diffusion coatings

These are Cr rich, aluminides or Pt modified aluminides coatings whose core function is to enrich surface of an alloy's bulk element with Al, Cr or Si (Pomeroy, 2005). Diffusion coatings function by either inward or outward diffusion. Inward diffusion is characterized by high activity of Al diffusing inwards faster than Ni outwards between the $NiAl$ intermetallic compounds (Stolle, 2009). This process occurs at temperatures of between 700-950°C with Ni_2Al_3 and $\beta - NiAl$ forming. However, heat treatment is critical to enable formation a fully homogeneous $\beta - NiAl$ layer. Outward diffusion on the other hand is characterized by high activity of Ni diffusing outward faster than Al, between the $NiAl$ intermetallic compounds and manifests at much elevated temperatures of between 1050-1100°C (Hardwicke et al., 2013; Juliš et al., 2010; Lee, 2006).

1.3.5.2. Overlay coatings

These coatings belong to M–Cr–Al–Y family, where M is the alloy base metal of Ni, Co, or a combination of both deposited on the substrate material using the electron beam physical vapor deposition (EBPVD) technique to yield high quality finishes (Eliaz et al., 2002).

1.3.5.3. Thermal barrier coatings (TBCs)

These are coatings designed to insulate the substrate material from hot burnt gases leaving the combustors. As they are from composite coating systems; they constitute of an outer ceramic coating, usually stabilized zirconia overlaid on an oxidation resistant bond coat from an M–Cr–Al–Y family or a diffusion aluminide coating (Rajendran, 2012).

1.3.5.4. Smart coatings

These are functionally graded overlay coatings produced using a combination of both plasma-spray and diffusion techniques. They are rich in sandwiched Cr layer that counters pitting corrosion in between aluminide rich overcoat to protect against high temperature oxidation and corrosion.

Despite the critical role played by protective coatings, their life cycle is limited to between 2000-4000 flight cycles making it cost intensive maintenance practice, coming approximately four times in the life of an aircraft (Stolle, 2009).

In this research, diffusion aluminide protective coating was used on the CT blades to improve thermal stress concentration and increase resistance of the material through formation of a continuously growing protective Al_2O_3 at temperatures over 1000 °C to mitigate against damage initiation and propagation (Bai et al., 2004; Choux et al., 2008; Hetmańczyk et al., 2007; Kianicová, 2009; Onyszko et al., 2009; Poręba et al., 2008; Sieniawski, 2003; Sudhangshu, 2007; Tamarin, 2002; Yavorska et al., 2008; Zielińska et al., 2009). This protective coating likewise increases engines efficiency by allowing higher operational temperatures, protects the core material from attack by chemical constituents in the fuel and the environment in which the engine operates as well as high temperature oxidation and hot corrosion (Fernandes et al., 2012; Fernandes et al., 2011; Gatto et al., 2004; Nicholls, 2003). Presence of Cr and Mo in this protective coating significantly improves the microstructure and deter development of interdiffusion zones (Zhang & Zhao, 2016).

Application of diffusion aluminide protective coating on Inconel 713LC is through pack cementation process whose merits amongst others include; suitability for small components, coat duplicability and low cost. With this method however, achieving uniform composition and the thickness of the protective coating is not guaranteed. Failure of this type of protective coating majorly occurs from micro cracking which evolve into cracks and eventual spallation or disintegration of Al_2O_3 (Evans et al., 2001; Nijdam et al., 2006).

1.4. Degradation of CT blades

Short-haul aircraft fleet experience high flight turnovers, frequent changes in power settings, numerous starts and stops. As a result, repeated mechanical loads; centrifugal forces and vibrations loads, thermal and aerodynamic loads are imparted on the CT blades. Repetitive exposure of CT blades to such harsh environment coupled with contaminants in fuel and air results in both internal and external damages of the CT blade material (Huang et al., 2006; Tamarin, 2002).

Internal damages manifest through phase aging (rafting), grain growth, grain boundary creep (Pollock et al., 2006), voiding, carbide precipitation and formation of brittle phases (Yoshioka et al., 2010).

External deterioration on the other hand presents as corrosion, oxidation, micro-crack formation, erosion and fretting (Carter, 2005). These damages lead to loss of material's and protective coating's strength (fatigue), (Pineau et al., 2009), manifestation of high-temperature time-dependent deformation (creep) (Pollock et al., 2006), cracking and propagation or even rupture from accumulated stress (Carter, 2005).

With the CT being the power harness of an engine, its failure means engine outage. Unfortunately, failure of CT blades account for 42% of all gas turbine outages (Rao et al., 2014; Simmons, 2004). In one such instances, on the 5th September 2010, a ten-seater Cessna 208B grand caravan aircraft operated by Tropic Airlines crashed without prior warning as a result engine in-flight shutdown elicited by CT blades failure (FCAA, 2014). The flight which was expected to last an average of 45 minutes was never to be despite the aircraft's previous successful flight having been made at the end of the morning.

The recommended maintenance practices required that overhaul (OVH) be carried out after every 3600 creep-fatigue hours, hot section inspection (HSI) after every 1800 creep-fatigue hours and borescope hot section inspection (BHSI) be conducted after every 400 creep-fatigue hours. On the fateful day however, the CT blades had only accumulated 3202 creep-fatigue hours < 3600 creep-fatigue hours; a stretch check had been conducted after 1411 creep-fatigue hour < 1800 creep-fatigue hours, while a BHSI had been performed 264 creep-fatigue hours < 400 creep-fatigue hours before the accident occurred. Despite these maintenance practices having been carried out in strict compliance with the manufacturer’s specifications, no defects on the CT blades were identified (Callister et al., 2011).

1.5. Closure

This chapter describes the CT blade assembly and the CT blade alongside their respective roles. It discusses the materials used in manufacture of the CT blades, highlights the composition and function of the constituent elements of the substrate material and protective coating used in Inconel 713LC. Finally, it shades light on mechanisms that degrade of the CT blades in service. The literature review chapter follows with the various techniques currently used to investigate degradation of CT blade material.

CHAPTER 2: LITERATURE REVIEW

2.1. Preamble

This chapter explores the various methods used to investigate CT blade material degradation with a view of developing road map to research implementation. The aim, the objectives and the scope of research are defined with structure of the thesis well outlined.

2.2. Techniques used to investigate degradation of CT blade materials.

2.1.1 Advanced diagnostics and prognostics for gas turbine engine risk assessment (Bovsunovskii et al., 2010). This is a probabilistic-modeling approach which relies on parameters sensed by engine health monitoring systems (EHMS), conducting inspections as well as referring to historical reliability data for inputs to predict failure. The approach entails evaluation of sensed data to identify fundamental EHMS failure modes. Fault identification is done with the use of selected diagnostic algorithms which are probabilistic or physics-based models taking into account design parameters and operating condition, systematically combined with fusion techniques (Gelman et al., 2009). Two procedures then have to be carried out; signal processing involving detection and diagnosis of sensor anomalies with no dependence on monitored system's characteristics, and physics-based modeling which facilitates sensor recovery from prior knowledge of the system characteristics (Loboda et al., 2007; Petrunin et al., 2008). Using a correlation matrix, tracking the degree of co-linearity between signals to detect noise is effected (Ricci et al., 2012). By applying stochastic models, neural network or probabilistic-based systems RUL of a component within conditions for a particular fault can be predicted (Bovsunovsky et al., 2015).

2.1.2 Modal analysis, Campbell and interference diagrams (Hou et al., 2002). This is an experimental-numerical simulation approach that was performed on a gas turbine that abruptly failed during morning start-up. Out of a total of 81 CT blades in the first row, only one blade was broken at its root. Stress analysis of the broken CT blade revealed that surpassing of maximum stress occurred due to pressure profiles developed during operation. Modal analysis was carried out to find out natural frequencies and modal shapes for fixed boundary conditions both experimentally and numerically, while Campbell and interference diagram were then drawn to check the dynamic characteristics of the CT blades, while vibration was measured using accelerometers in the operation condition (Boyce, 2011).

2.1.3 Health monitoring and prognosis of blades and disks with blade tip sensors are sensor based techniques employed to monitor blade tip clearance (BTC) and vibration (Goel et al., 2008; Kargarnejad et al., 2012; Kim et al., 2011; Naeem et al., 2009; Sujata et al., 2010a, 2010b; Tarafder et al., 2013; Von Flotow et al., 2000). Use of sensors varying from capacitors, inductors, optical aids, microwave signals, infrared, eddy-currents, pressure transducers, acoustic signals, magnetic signals among others are employed. The sensors acquire signals of say crack growth from CT blade lengthening over time with the crack signal getting isolated and distinguished using data reduction differentiators for processing the magnitude of damage. A practical capacitive sensor assemblage for example will constitute of heavy-duty probes, high frequency signal output, signal amplifier and a sophisticated integrated electronic circuit for signal processing. This techniques is handy for analyses of magnitudes of vibrations, eccentricity or rotational anomalies to interpret changes in microstructure of CT blade material (Steiner, 2000).

2.1.4 Microstructural observations techniques are dedicated to account for damages of CT blades after exposure to service to establish engine operating conditions. Against preset standards for permissible limits to degradation, designers and manufacturers can then advice on the best course of action to be taken on a CT blade sample. Complementary to microstructural study is metallographic examination (Pollock et al., 2006; Zhao et al., 2008). In application of microstructural change observations, the alloying system (metallurgical composition) threshold and engine operating conditions which are usually preset by the CT blades material manufacturers (Everitt, 2012; Gelman et al., 2009; Kartal et al., 2011; Roemer et al., 2000).

2.1.5 Health risk assessment and prognosis of gas turbine blades by simulation and statistical methods make use Monte Carlo simulations for operational data of CT blades to model health assessment for future life prediction. (Bovsunovskii et al., 2010; Khajavi et al., 2004; Poursaeidi et al., 2008; Roemer et al., 2000; Sujata et al., 2010b). As it is an algorithmic based approach, input data has to be formulated for adoption to monitor BTC. Operational sensed data collected are processed in probabilistic distributions (lognormal and normal) and then treated with regression analysis for turbine blade life prognosis. One example of one such methods is hybrid mathematical model, the extremum selection method (ESM), for nonlinear reliability analysis of radial deformation of gas turbine blades which arguably can yielded results of accuracy levels up to 99.972% (Fei et al., 2012).

2.1.6 Optical methods are known to be complimentary of microstructural and metallographic examination methods. Optical aids range from; visual, metallographic scans, microscopy, quantitative examination of the base alloy, x-rays, microprobe analysis, deposit analysis and examination of laboratory specimens (Eliaz et al., 2002; Singh et al., 2007). Optical inspections for example can done to check microstructural changes of hot corrosion by attacks of deposition of alkali metal sulfates on the blade and vane surfaces from fuels containing contaminants such as sulfur, sodium, potassium, vanadium, lead, and molybdenum (Gelman et al., 2009; Petrunin et al., 2008; Ricci et al., 2012).

2.1.7 Component diagnostic and prognostic modeling (CDPM) is a reliability-modeling approach which works by evaluating the distribution of RUL of a component as a dependent of uncertainties for a specific fault (Von Flotow et al., 2000). Normally, neural networks containing collected, diagnostic, current condition assessment and operational profile data are used to make real-time failure predictions which inform of decisions to be taken; a corrective measure, to repair or replace the part, or a compensatory one to lower the systems' operational loads in order to extend the life of the faulty part (Bryg et al., 2008; Byington et al., 2002; Jaw, 2005; Joly et al., 2004; Litt et al., 2004; Pinelli et al., 2001; Roemer et al., 2000; Romessis et al., 2007; Simon, 2010; Simon et al., 2008; Singh et al., 2007; Wang et al., 2004). The methods employed in CDPM include:

2.1.7.1 Gas path analysis (GPA) is a physical approach that is capable of acquiring, processing and relate measured data with health parameters as well as assign a decision-making process. GPA can be used for example to represent the aero-thermodynamic processes occurring in the engine components with the mechanical coupling linking them to a black box's mathematical model to relate measured signals with health parameters. The output of which could either be a specified pattern recognition technique or an artificial intelligence based expert system. The elements constituting the model are operationally classified as being: steady or transient states, mathematical or physical based, and artificial intelligence or conventional methods (Stamatis, 2014).

2.1.7.2 Expert systems (ES) make use of expert knowledge of automated inference engines from computer programs to provide solutions for engine problems which could be; rule, case, or model-based. In practice, specific expert knowledge from condition monitoring is never understood when making solutions and for this reason, undisclosed information and solution formulation is necessary for ES to be robust in problem solving (Stamatis, 2014).

2.1.7.3 Hybrid and fusion information techniques are genetic algorithm or artificial neural network integrated fault diagnostic models for identifying shifts in component performance and sensor faults (Kong, 2014). These models operate in two categorical cases; the first is use of response surfaces to compute objective functions to improve exploration potential associated with a fault in order to make computational burden lighter. The second is application of neural networking with genetic algorithm to create a hybrid diagnostics model. The neural network serves as a pre-processor to minimize the number of fault groups to be investigated by the genetic algorithm based model to improve accuracy, reliability and consistency as well as total run time (Zwingenberg et al., 2012).

2.1.8 Monitoring low cycle fatigue (LCF) is an experimental-modeling approach that makes use of a rotating Timoshenko beam with taper twist to model a turbine blade with frequency data is derived from finite element analysis (FEA). An experiment is carried out with a model subjected to continuum damage mechanics to accurately capture the non-linear nature of LCF damage (Madhavan et al., 2014). Changes in rotating frequencies recorded during the experiment are interpreted for the magnitude of LCF within the CT blade material. With the help of simulated deterioration curves relating frequencies vs. damage, thresholds can be assigned before 90% percent of CT blade life is damaged (Kumar et al., 2007; Li et al., 2009; Scott-Emuakpor et al., 2015; Simon, 2010; Simon et al., 2008; Vakhtin et al., 2009).

2.1.9 New Chirp-Wigner higher order spectra (HOS) for transient signals with any known nonlinear frequency variation is a use of sensor-simulation based approach for detecting nonlinear behavior of transient signals with nonlinear polynomial time variation of the instantaneous frequency based on the Fourier transform (Yang et al., 2012). Independent synchronous measurements from sensors and tachometers are used as sources of data for the system. The challenges associated with the technique however lies with estimation of signal amplitude with known time variation of the instantaneous frequency as well as being limited to applications with only stationary HOS (Kumar et al., 2007; Procházka et al., 2011; Szczepanik et al., 2012).

2.1.10 Adaptive diagnosis of bilinear mechanical systems is a numerical modeling approach based on free oscillation for diagnosis of bilinear mechanical systems by varying of resonance frequency from free oscillations. Two cases of signal occurrence are then analyzed; occurrence of frequency-independent and the frequency-dependent internal damping (Roemer et al., 2000). Evaluation of effectiveness for the suitable case to be adapted is conducted through numerical simulation (Chen et al., 2012; Gelman, 2007, 2010; Natke et al., 2012; Procházka et al., 2011; Witek, 2011; Witoś et al., 2009).

2.1.11 Non-linear vibro-acoustical free oscillation is a vibro-experimental and modeling for crack detection approach. It is based-on excitation of a specimen free of oscillations to produce vibro-acoustical signals with oscillations varying with the appearance of an existing one. Normally, a decrease in free oscillations would indicate crack occurrence (Bovsunovsky et al., 2015). Further decrement would possibly indicate relative crack size, factor of damping without crack, relative factor of damping and model's natural frequency. In analysis of decrements, the following four cases are crucial; frequency-dependent and frequency-independent, external and internal friction effects. Validation of method to be adapted relies on the estimated value of natural frequency and interfering parameter. Experimental results are then likened to the theoretical prognosis by the considered nonlinear model (Gelman et al., 2016; Kucher et al., 2009; Matveev et al., 2006; Matveev et al., 2010; Ramezanpour et al., 2012; Tadayon, 2014).

2.1.12 Higher order coherence (HOC) for fatigue crack detection is a technique designed to detect fatigue crack from the vibration responses due to known excitation, natural excitation from rotating speed of machines or wind excited structures (Broda et al., 2014). Two such classical examples are the bi-spectrum and tricoherence methods formulated from double and triple Fourier transformation of third and fourth order moment of time signals associated with two and three frequency components respectively (Zhang, Peng, et al., 2016). These methods could reveal HOC between exciting frequencies and their related harmonics since breathing of the cracks generates harmonics in the exciting frequencies. In view of this, computational effort and time is saved without losing any information related to the crack detection process (Chen et al., 2013; El-Maksoud, 2013; Gelman, 2010; Gelman et al., 2004; Gelman et al., 2000).

2.3. Findings from review of literature

Monitoring of protective coating and substrate material of the CT blades is crucial to avert un forewarned catastrophic failures and maintain healthy status (Kargarnejad et al., 2012). The techniques used to investigate degradation in CT blade material could be classified as;

optical methods, microstructural-metallurgical approaches, use of sensors, experimental approaches, numerical modeling approaches, probabilistic-modeling approaches, statistical modeling approaches, reliability modeling approaches and vibro-modeling approaches as summarized in Table 2.1. Synthesis through literature reveals that:

1. Current techniques used to investigate failure of CT blades either estimate the life or only inform of after exposure to service with hardly any information accounting for numerous premature failures. As such, the health of CT blade material; the real-time material status, the magnitude of accrued damage and the RUL cannot be told.
2. Very little work has been done on assimilating existing, new and emerging techniques to investigate degradation of CT blade material.
3. In this regard, current research opted to assimilate FEA, microstructure and metallurgical studies as well as mechanical testing, to offer a more formidable, robust and an easy to adopt approach in CT blade material investigations. This will enhance safety, increases operational availability of aircrafts and make planning for maintenance easier.

Table 2. 1: Techniques used to investigate degradation of CT blades

Technique	Surveyed Papers	Classification
1. Advanced diagnostics and prognostics for risk assessment	(Bovsunovskii et al., 2010; Bovsunovsky et al., 2015; Gelman et al., 2009; Loboda et al., 2007; Petrunin et al., 2008; Ricci et al., 2012)	Probabilistic Modeling Approach
2. Modal analysis, Campbell and Interference diagrams	(Boyce, 2011; Choi et al., 2010; Hou et al., 2002)	Experimental Numerical Simulation
3. Health monitoring and prognostics of blades and disks using lade tip sensors	(Goel et al., 2008; Kargarnejad et al., 2012; Kim et al., 2011; Naeem et al., 2009; Steiner, 2000; Sujata et al., 2010a; Tarafder et al., 2013; Von Flotow et al., 2000)	Use of Sensors
4. Microstructural study	(Everitt, 2012; Gelman et al., 2009; Kartal et al., 2011; T. M. Pollock et al., 2006; Roemer et al., 2000; Zhao et al., 2008)	Microstructural Metallurgical Investigations
5. Health risk assessment and prognosis of gas turbine blades by simulation and statistical methods	(Bovsunovskii et al., 2010; Fei et al., 2012; Khajavi et al., 2004; Poursaeidi et al., 2008; Roemer et al., 2000; Sujata et al., 2010b)	Simulation Statistical Approach
6. Optical methods	(Bovsunovsky et al., 2015; Cardwell et al., 2008; Choi et al., 2010; Eliaz et al., 2002; Gelman et al., 2009; Giggins et al., 1980; Gurrappa, 2001; Hou et al., 2002; Petrunin et al., 2008; Rapp et al., 1981; Ricci et al., 2012; Singh et al., 2007; Steiner, 2000; Tappert et al., 2001; Young et al., 1995)	Optical Approach
7. Component diagnostic and prognostic modeling	(Bryg et al., 2008; Byington et al., 2002; Jaw, 2005; Joly et al., 2004; Kong, 2014; Li et al., 2009; Litt et al., 2004; Pinelli et al., 2001; Roemer et al., 2000; Romessis et al., 2007; Simon, 2010; Simon et al., 2008; Singh et al., 2007; Stamatis, 2014; Von Flotow et al., 2000; Wang et al., 2004; Zwingenberg et al., 2012)	Reliability Modeling Approach
8. Monitoring low cycle fatigue	(Kumar et al., 2007; Li et al., 2009; Madhavan et al., 2014; Scott-Emuakpor et al., 2015; Simon, 2010; Simon et al., 2008; Vakhtin et al., 2009)	Experimental Modeling Approach
9. New Chirp-Wigner higher order spectra	(Kumar et al., 2007; Procházka et al., 2011; Szczepanik et al., 2012; Yang et al., 2012)	Sensor Simulation Approach
10. Adaptive diagnosis of bilinear mechanical systems	(Chen et al., 2012; Gelman, 2007, 2010; Natke et al., 2012; Procházka et al., 2011; Roemer et al., 2000; Witek, 2011; Witoś et al., 2009)	Numerical Modeling Approach
11. Non-linear vibro-acoustical free oscillation	(Gelman et al., 2016; Kucher et al., 2009; Matveev et al., 2006; Matveev et al., 2010; Ramezanpour et al., 2012; Tadayon, 2014)	Vibro-Modeling and Experimental Approach
12. Higher order coherences for fatigue crack detection	(Broda et al., 2014; Chen et al., 2013; El-Maksoud, 2013; Gelman, 2010; Gelman et al., 2004; Gelman et al., 2000; Zhang, Peng, et al., 2016)	Vibro-Modeling Approach
13. Assimilative approach (current work)	Ngoret, J. K., & Kommula, V. P.	Modeling-Characterization-Strength Testing

2.4. Aim of this research

To characterize the influence of thermo-mechanical stresses leading to premature failure of CT blades of short-haul aircraft fleet, using an assimilative approach.

2.5. Research objectives

1. To review the techniques currently used to investigate CT blade material degradation.
2. To model, extract and evaluate thermo-mechanical degradation on the CT blade using finite element analysis (FEA).
3. To characterize microstructural and metallurgical degradation of the protective coating and the substrate material of the CT blades using XRF, XRD and EDS-SEM.
4. To determine mechanical strength of the prematurely retired CT blades.
5. To validate the research results against the manufacturer’s specifications and actual operator’s data.

2.6. Scope of research

In line with the research aim and objectives, the scope of present work is limited to:

1. Carry out FE modeling, extraction and evaluation of thermo-mechanical degradation on CT blades, in an environment that mimics the actual operational conditions to ascertain CT blade life and resulting damage.
2. Characterize the diffusion aluminide protective coating and substrate material of CT blades prematurely retired from a HP, PT6A-114A engine of a Cessna 208B.
3. Determine the mechanical strength of the prematurely retired CT blade samples.

2.7. Structure of the thesis

Chapter 1 describes the CT blade assembly, the CT blade and their respective functions; it discusses the materials used to manufacture the CT blades in research, its composition as well as function of the constituent elements of the substrate material and the diffusion aluminide protective coating used. It finally sheds light on mechanisms that degrade of the CT blades in service.

Chapter 2 presents a comprehensive survey and categories of available methods used to investigate degradation of CT blades. It gives direction to implementation of research through the aim, objectives and scope of the research. The chapter finally provides the structure of the thesis.

In Chapter 3, FE modeling of thermo-mechanical stresses on CT blade in an environment that mimics the actual operational conditions was conducted to evaluate CT blade life and resulting damage.

Chapter 4 elaborately characterizes the microstructure and metallurgical degradation on the protective coating as well as the substrate material of the CT blade.

Chapter 5, presents mechanical testing of the CT blades to establish the residual mechanical strength the CT blades at the time of retire from service.

The concluding chapter 6 is dedicated to validating the results obtained in FE modeling, characterization and strength tests chapters against the manufacturer’s and operator’s data. The chapter also submits the novel contributions to body of knowledge and scope of future work.

2.8. Closure

Chapter 2 surveyed and synthesized the various techniques used to track the life of CT blade material. This enabled forging of a plan for implementation of the outlined objectives in this work. The scope of research and the structure of the thesis were similarly drawn in this chapter. This chapter is followed by FE modeling of the CT blade chapter in an environment that mimics the operational one in order to evaluate CT blade life and resulting damage thereof.

CHAPTER 3: MODELING, EXTRACTING AND EVALUATING THERMO-MECHANICAL DEGRADATION ON THE CT BLADE

3.1 Preamble

This chapter presents step by step FEA of thermo-mechanical degradation mentioned in section 1.4, which account for the greatest percentage of the flight loads on the HP CT blade (Kargarnejad et al., 2012) in an environment that resembles the actual operational conditions, to enable evaluation of CT blade life and resulting damage.

3.2 FE Modeling

Stress analyses in CT blades are invariably complex tasks rendering many such problems extremely difficult and tedious to obtain analytical solutions. Consequently, FEA permits locating of approximate solutions to a vast range of numerical problems, sophisticated geometries and boundary conditions.

Commercial ANSYS Workbench was used for these analyses owing to easy interface and integration between simulation modules and solvers, ready interaction with other computer aided drawing (CAD) packages, ability to yield step wise solution schemes between modules, ability to offer high precision solutions by minimizing on contact errors, ability to allow for rectification of error as and when they arise, as well as updating of geometries, initial, boundary conditions amongst other parameters.

Finite element analysis (FEA) had three main executional stages; the preprocessing, solution and post processing phases as illustrated in the computational flow chart in Fig. 3.1.

The preprocessing phase involved development of a solid three-dimensional, PT6A-114A engine HP CT blade model in commercial CAD-SolidWorks environment, taking into account its dimensions from idealized National Aeronautics and Space Administration (NASA) blade design (Thulin et al., 1982) without much simplification as conveyed in Fig. 3.2. Subsequently, the CT blade model was imported to ANSYS Workbench 15.0 for FEA.

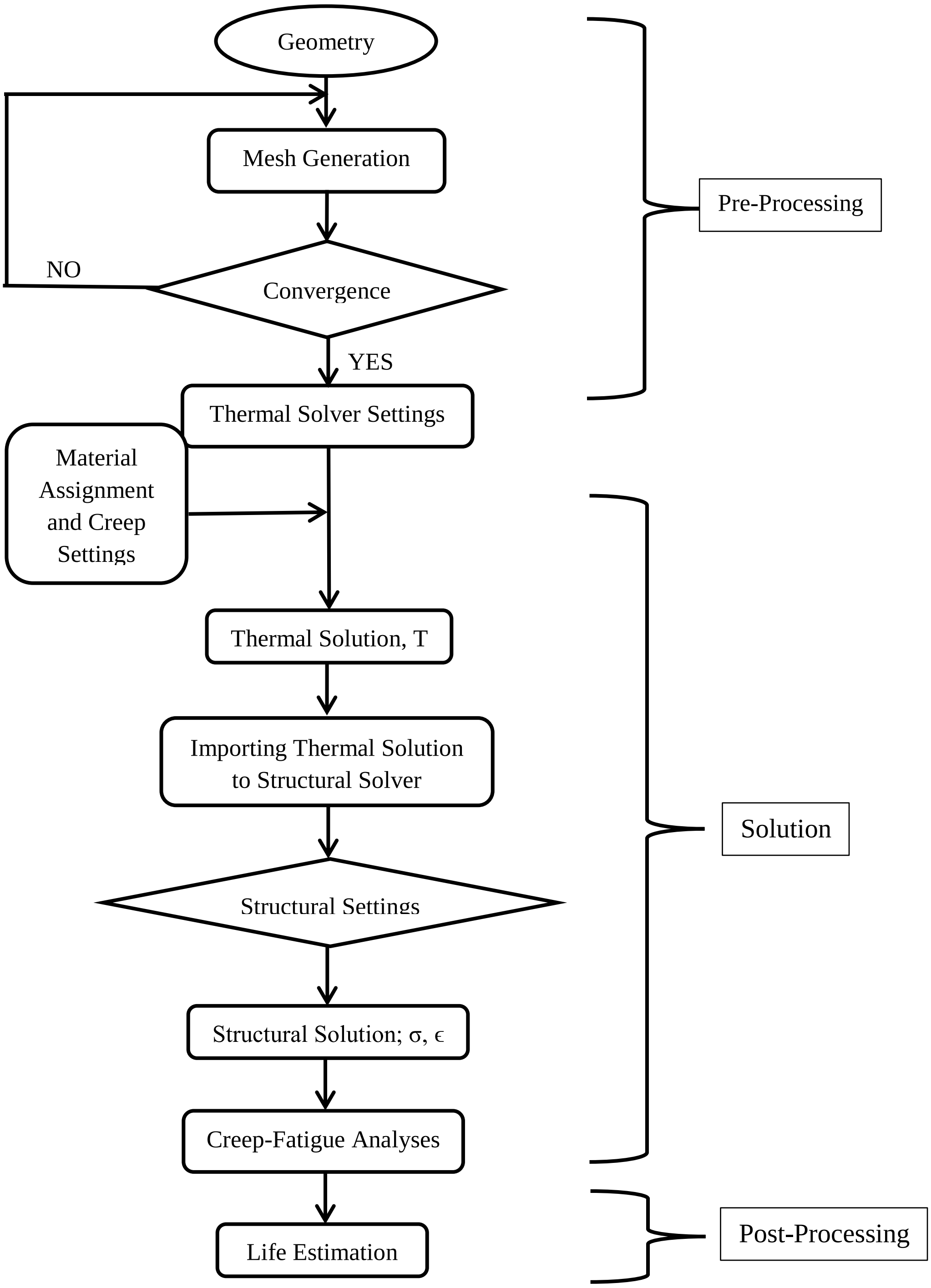

Figure 3. 1: Flowchart for numerical computational

In the solution phase, the CT blade was treated for transient thermal stresses which are occasioned by the heat generated from the combustors and static structural stresses originating from rotational velocities of the engine and accounting for 80% of inertial field during flight (Cookson et al., 2008). Modeling of the thermo-mechanical stresses and strains experienced by the CT blade in such an environment were done to establish the life of the CT blade and accrued damage. In this research segment a platform on which simultaneous and parametric use of stress and strain models in temperature fields as well as optimization of creep-fatigue damage modules were integrated.

The last phase of modeling was the post-processing, in which graphical presentations of figures and plots to illustrate the response behavior of the CT blade in the modeling environment.

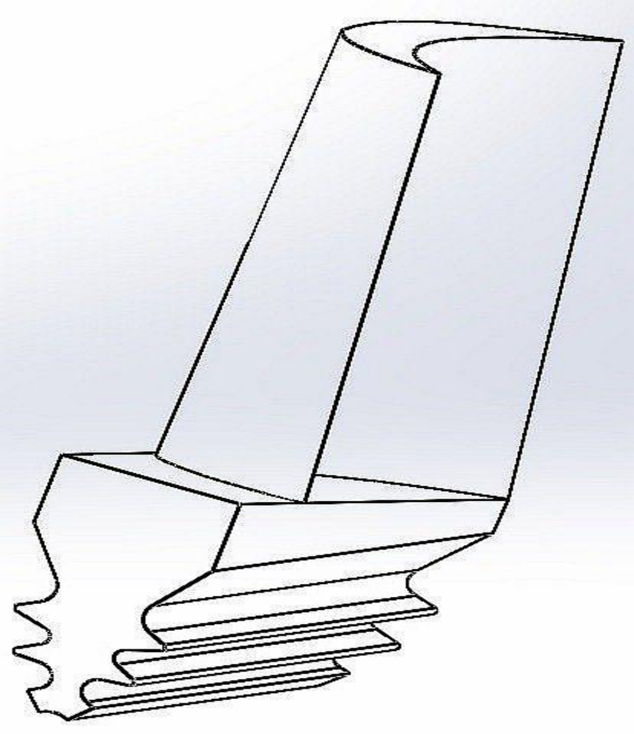

Figure 3. 2: A three-dimension geometrical model of PT6A-114A HP CT blade

3.2.1. Thermal analyses

By solving the governing Eq. 3.1, thermal stresses and temperature fields were evaluated.

$$[C^t]\{\dot{T}\} + [K^t]\{T\} = \{Q\} \qquad 3.1$$

By applying the principle of virtual temperatures, Eq. 3.1 was transformed to Eq. 3.2 (Žmindák et al., 2008):

$$C^t\dot{T} + (K^{tm} + K^{th} + K^{tc}).T = Q^f + Q^c + Q^g \qquad 3.2$$

Where C^t is thermal capacity matrix, K^{tm} is mass transport conductivity matrix, K^{th} is diffusion conductivity matrix, K^{tc} is convection surface conductivity matrix, T is temperature vector, Q^f is mass flux vector, Q^c is convection surface heat flow vector, Q^g is heat generation load vector.

3.2.1.1 Mesh generation

Prior to computing solutions in the thermal solver, mesh of the model was generated. Global mesh density was selected to minimize discretization errors in the failure regions. During meshing; mesh control, element shape, size and node placements were set. Systematic mesh refinement was then carried out at critical locations of the model to ensure accuracy of solution was maintained. This was achieved by gradually increasing the number of elements until converged solutions of the resulting stresses were achieved.

After varying mesh densities, the discretized CT blade thermal model yielded 1013089 elements and 687125 nodes confirming convergence as depicted in Fig. 3.3.

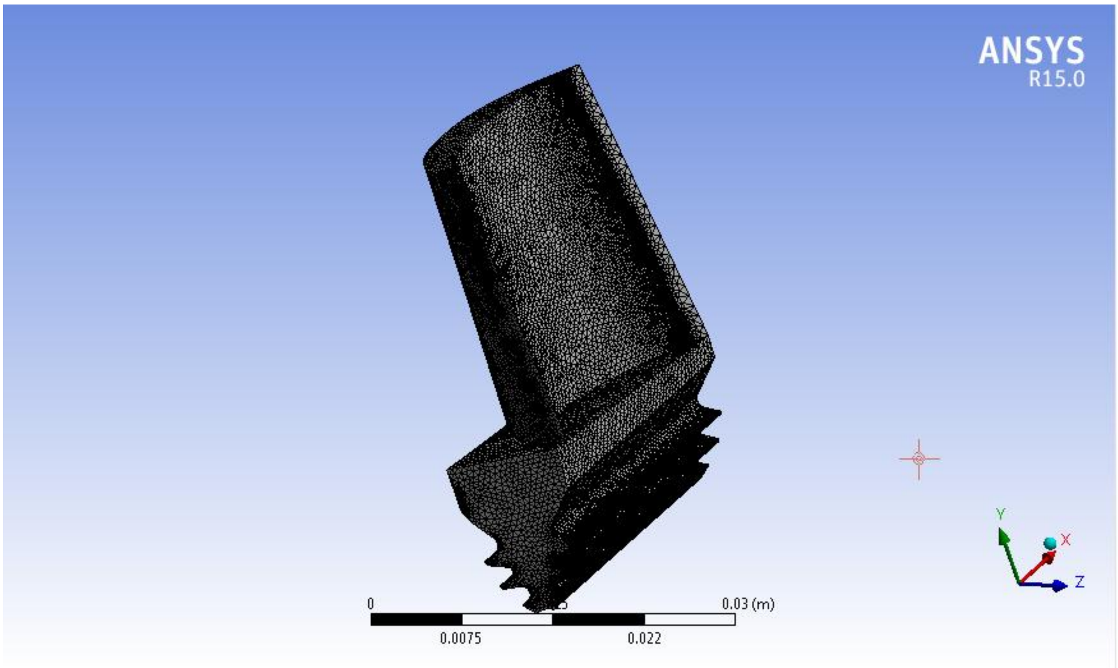

Figure 3. 3: Discretized CT blade thermal model

The final parametric mesh quality assessment was performed within FEM Workbench framework with the key indicators being orthogonal quality and skewness. The computed element metrics which are functions of element shape geometry with respect to percentage mesh volume ascertained that the mesh was of high quality. The more the elements associated with orthogonal quality tend towards unity, the more accurate is the mesh, while the more the elements tend towards zero, the more accurate is the mesh as illustrated in Figs 3.4 and 3.5.

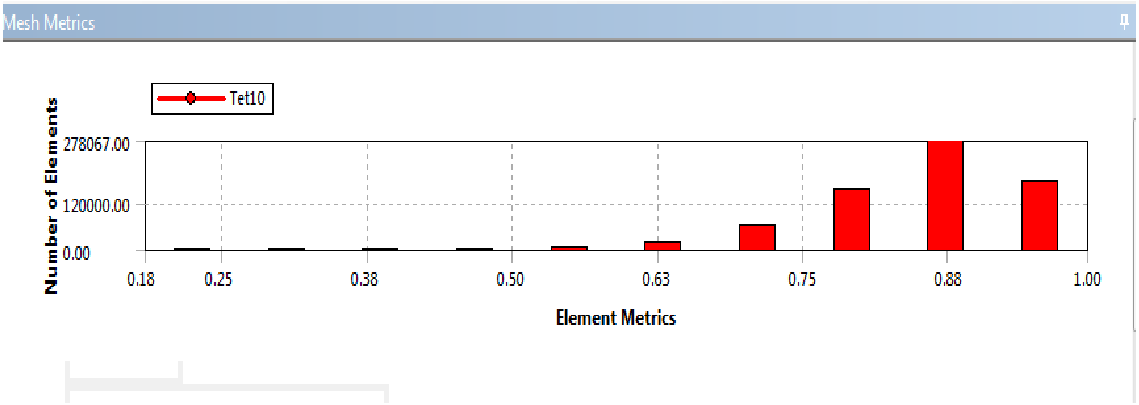

Figure 3. 4: Orthogonal quality mesh metrics for the thermal model

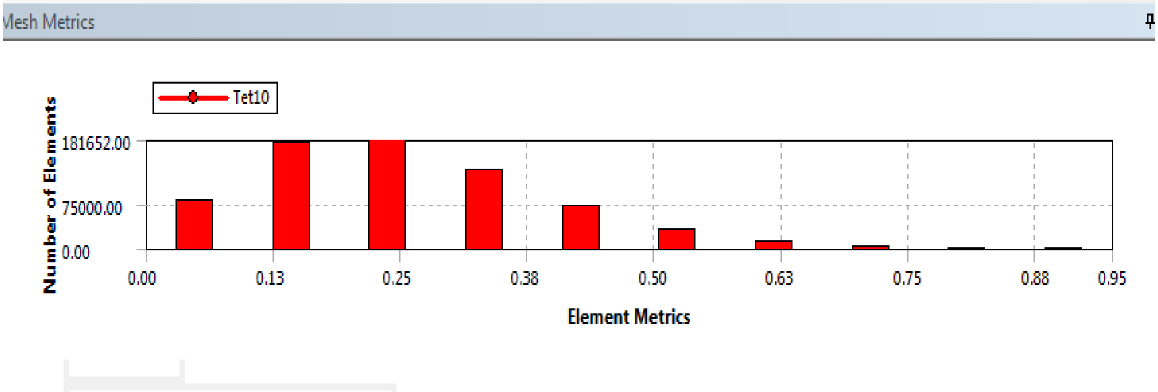

Figure 3. 5: Skewness mesh metrics for the thermal model

The meshed CT blade thermal model elements were then assigned material properties as captured in Table 3.1 and creep module was invoked at this stage as will be discussed in creep-fatigue analyses in section 3.2.3.

Table 3. 1: Physical Properties of Inconel 713LC (Nickel Institute, 2017)

Property	**Symbol**	**Range**
Density	ρ	7913 kg/m^3
Melting Point		1260 – 1280 ℃
Modulus of Elasticity	E	210 GPa
Factor of Safety	*FOS*	1.68
Poisson’s Ratio	μ	0.3
Specific Heat Capacity		435 J/kg℃
Thermal Conductivity	K	Room Temp: 11 W/m.K

3.2.1.2. Thermal settings

From the engine operating guidelines, the transient regime representing a phase of flight with the most aggressive stresses on the CT blades was adopted for both thermal and rotational speeds, where the inter turbine operating gas temperature was given as 850ºC (Red Sky Ventures, 2017). The boundary conditions which obtained from material properties drawn from Table 3.1 and running prior steady state heat transfer were used for transient loading without increasing the complexity of analyses for heat transfer on the CT blade.

Heat transfer by convection causes differential temperature distribution which results to induction of thermal stresses on the material as illustrated in Fig. 3.6. The convective heat transfer is given as 13000W/m^2.ºC for temperature ranges 815-950ºC (Nickel Institute, 2017).

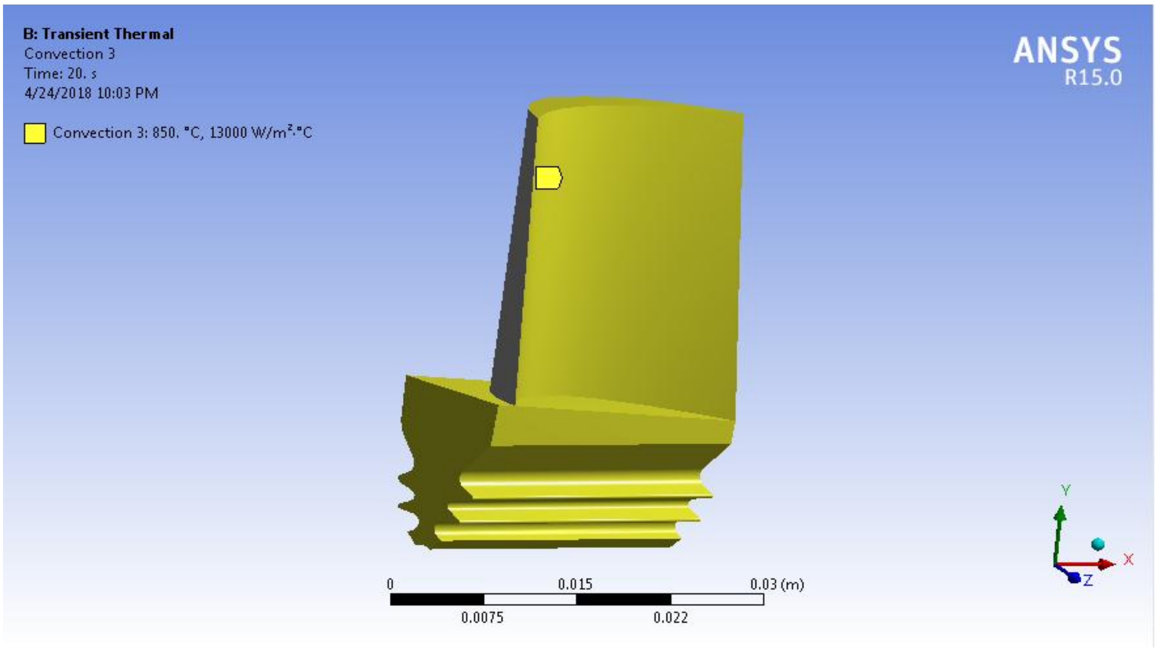

B: Transient Thermal
Convection 3
Time: 20. s
4/24/2018 10:03 PM

🟨 Convection 3: 850. °C, 13000 W/m²·°C

Figure 3. 6: Convection heat transfer

The creep-thermal model was then initialized in order to obtain temperature distribution on the surface of the CT blade. In this thermal problem radiation is considered to be negligible.

3.2.2. Rotational analyses

In the structural platform, rotational analyses were guided by the governing Eq. 3.3.

$$[M]\{\ddot{X}\} + [C]\{\dot{X}\} + [K]\{X\} = \{F\} \qquad 3.3$$

Where $[M], [C] \& [K]$ are mass, damping and stiffness matrices respectively, $\{\ddot{X}\}, \{\dot{X}\} \& \{X\}$ are acceleration, velocity and displacement vectors, while F is the force vector.

3.2.2.1. Rotational settings

The root of the CT blade was constrained in the axial direction with a fixed support to keep it in direction of rotation as depicted in Fig. 3.7.

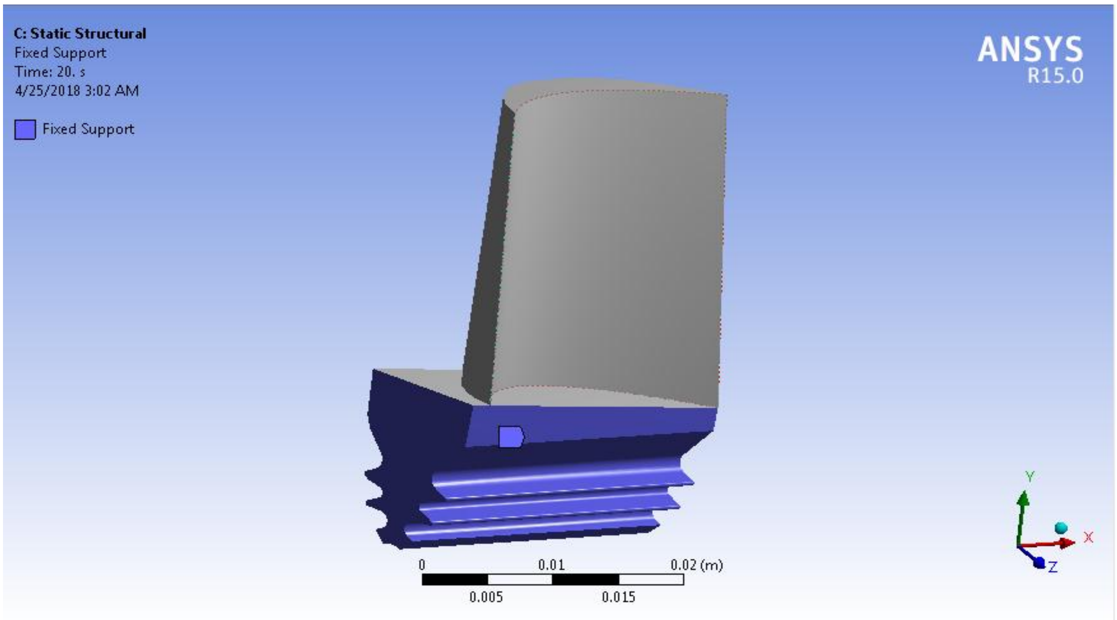

Figure 3. 7: Fixed support prior to application of rotational load

Rotational velocity of magnitude 1047.2 radians/second given for transient regime (Red Sky Ventures, 2017) was applied in the axial and acting parallel to the rotation of the shaft as indicated in Fig. 3.8. before damage initialization.

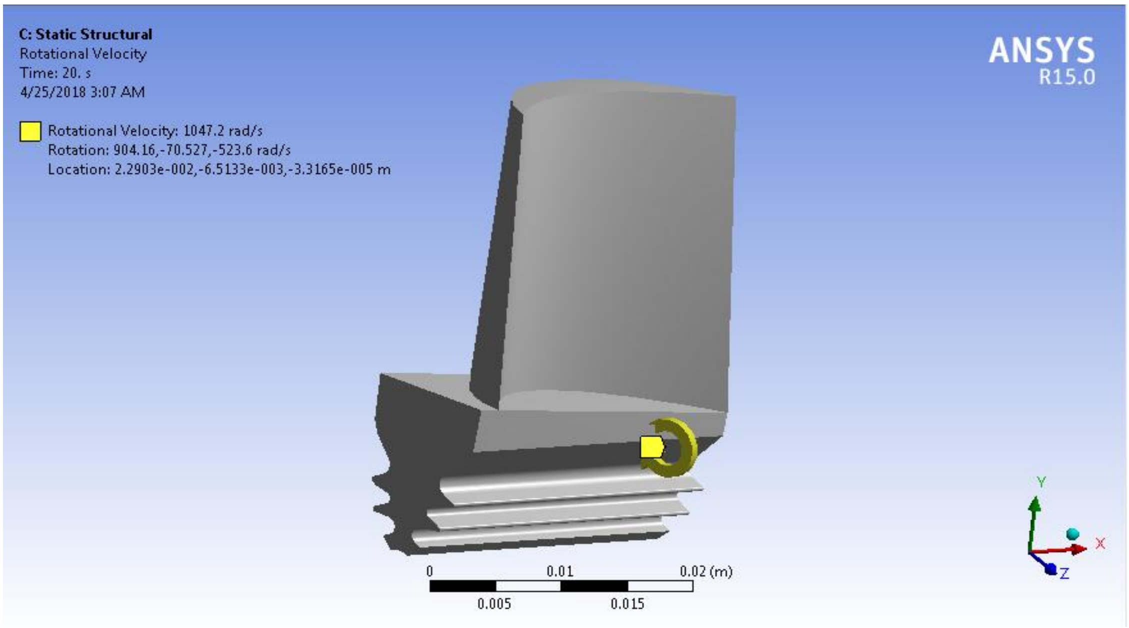

C: Static Structural
Rotational Velocity
Time: 20. s
4/25/2018 3:07 AM

🟨 Rotational Velocity: 1047.2 rad/s
Rotation: 904.16,-70.527,-523.6 rad/s
Location: 2.2903e-002,-6.5133e-003,-3.3165e-005 m

Figure 3. 8: Application of rotational velocity

The combined thermo-mechanical loading on the CT blade could then defined by Hooke’s law in the constitutive form stated in Eq. 3.4.

$$\left.\begin{aligned}\epsilon_{xx} &= {}^{1}\!/_{E}\,\left[\sigma_{xx} - \upsilon\left(\sigma_{yy} + \sigma_{zz}\right)\right] + \alpha\tau = {}^{1}\!/_{2G}\left(\sigma_{xx} - {}^{\nu}\!/_{1+\nu}\,\Theta\right) + \alpha\tau\\ \epsilon_{yy} &= {}^{1}\!/_{E}\,\left[\sigma_{yy} - \upsilon\left(\sigma_{xx} + \sigma_{zz}\right)\right] + \alpha\tau = {}^{1}\!/_{2G}\left(\sigma_{yy} - {}^{\nu}\!/_{1+\nu}\,\Theta\right) + \alpha\tau\\ \epsilon_{zz} &= {}^{1}\!/_{E}\,\left[\sigma_{zz} - \upsilon\left(\sigma_{xx} + \sigma_{yy}\right)\right] + \alpha\tau = {}^{1}\!/_{2G}\left(\sigma_{zz} - {}^{\nu}\!/_{1+\nu}\,\Theta\right) + \alpha\tau\\ &\epsilon_{xx} = {}^{\sigma_{xy}}\!/_{2G},\;\; \epsilon_{yz} = {}^{\sigma_{yy}}\!/_{2G},\;\; \epsilon_{zx} = {}^{\sigma_{zx}}\!/_{2G}\end{aligned}\right\} \qquad 3.4$$

Where τ is temperature of the CT blade in unstrained state, i.e. $\tau = T - T_o$, E is the Young’s Modulus, G is the Shear Modulus, ν is the Poisson’s ratio, constants of CT blade material while α is the coefficient of linear thermal expansion coefficient equivalent to 9.8 µstrain/^{o}C (Granta, 2018) and $\Theta = \sigma_{xx} + \sigma_{yy} + \sigma_{zz}$.

By applying the principle of variation to the governing equations of elastic continua and thermos-elastic constitutive equations, this thermo-elastic problem was solved in Eq. 3.5.

$$\begin{bmatrix} M & 0 \\ 0 & 0 \end{bmatrix}\begin{Bmatrix} \ddot{U} \\ \ddot{T} \end{Bmatrix} + \begin{bmatrix} C & 0 \\ C^{tu} & C^{t} \end{bmatrix}\begin{Bmatrix} \dot{U} \\ \dot{T} \end{Bmatrix} + \begin{bmatrix} K & K^{ut} \\ 0 & K^{t} \end{bmatrix}\begin{Bmatrix} U \\ T \end{Bmatrix} = \begin{Bmatrix} F \\ Q \end{Bmatrix} \qquad 3.5$$

Where M is element mass matrix, C is element structural damping matrix, K is element stiffness matrix, U is displacement vector, F is structural load vector, K^{t} is element diffusion conductivity matrix, Q is summation all heat vectors in Eq. 3.5, K^{ut} is element thermo-elastic damping matrix. Since the interactions between thermal and structural fields were now of low degree of nonlinearities, a more flexible and efficient solution for the analyses was required such that; $K^{ut} = C^{tu} = 0$ and $C = 0$. The general solution is therefore denoted in Eq. 3.6.

$$\begin{bmatrix} K_{11}(X_1, X_2) & 0 \\ 0 & K_{22}(X_1, X_2) \end{bmatrix} \begin{Bmatrix} X_1 \\ X_2 \end{Bmatrix} = \begin{Bmatrix} F_1(X_1, X_2) \\ F_2(X_1, X_2) \end{Bmatrix} \quad 3.6$$

Where the mean stress curves were then used for mapping mean stress effects, while multi-stress correction was accounted for by von mises and maximum principal stress contours after which, total deformation, equivalent stress and strain were computed.

3.2.3. Creep-fatigue analyses

Creep-fatigue analyses for damage and life were executed from thermo-mechanical solutions. Constant amplitudes stress and strain components were used to define the loads, representing a flight phase that follows a predetermined path. During the entire period of computation, the load and boundary conditions in creep analyses were the same as those in mechanical analyses and the conditions were held similar.

Creep deformation was modeled as creep strain rate which is a function of stress, strain, time, and temperature as specified in Eq. 3.7.

$$\dot{\varepsilon_{cr}} = f_1(\sigma) f_2(\epsilon) f_3(t) f_4(T) \quad 3.7$$

Computation of creep was governed by Norton’s power law expressed in Eq. 3.8 in its constitutive form.

$$\dot{\varepsilon_{cr}} = C_1 \sigma^{C_2} e^{-C_3/T} \quad 3.8$$

Where $\dot{\varepsilon_{cr}}$ is the creep strain rate, σ is the stress in (MPa), ϵ is creep strain, t is time in (hours), T is temperature in (°C), C_1, C_2, are C_3 material constants. Temperature dependency was defined using the Arrhenius law stipulated in Eq. 3.9 to avoid multiple creep constants which yield linear based interpolation rather than more accurate log-based solutions.

$$\dot{\varepsilon_{cr}} = e^{-Q/RT} \quad 3.9$$

Where Q is the activation energy, R is the universal gas constant and T is the absolute temperature.

Fatigue analyses were performed to characterize the ability of the CT blade to survive many cycles during its lifetime. The stress and strain components are governed by Neuber's Rule as presented in Eq. 3.10.

$$\varepsilon\sigma = K_t^2 eS \tag{3.10}$$

Where ε is the total strain, σ is the total stress, K_t is the elastic stress concentration factor for a mesh that is well refined, e is the nominal elastic strain and S is the nominal elastic stress. Since stress life was based on stress-cycle curves, computation of was done without distinguishing between initiation and propagation of damage.

Constant amplitude, fully reversed proportional loading was applied for fatigue analyses as only one set of FE stress results along with a loading ratio was required to calculate the alternating and mean values. Likewise, the principal stress axes did not change over time allowing a single set of FE results to identify critical fatigue locations and with only two loadings. No cycle counting or cumulative damage computation needed to be done and the Soderberg Theory depicted in Eq.3.11 accounted for the mean stress correction.

$$\frac{\sigma_A}{S_{EL}} + \frac{\sigma_M}{S_{YS}} = 1 \tag{3.11}$$

Where σ_A is the alternating stress, S_{EL} is the stress at elastic limit, σ_M is the mean stress and S_{YS} is the yield stress.

In a similar manner to stress, mean strain correction was accounted for by Morrow's method as presented in Eq. 3.12.

$$\frac{\Delta\varepsilon}{2} = \frac{\sigma'_f - \sigma_M}{E} + \left(2N_f\right)^b + \varepsilon'_f\left(2N_f\right)^c \tag{3.12}$$

Where $\frac{\Delta\varepsilon}{2}$ is the total strain amplitude, σ'_f is the fatigue strength coefficient, $\sigma_M$is the mean stress, E is the Young's modulus, N_f is the number of cycles to failure and $2N_f$ is the number of reverse cycles to failure.

Multiaxial stress correction was defined by von-mises stresses as they are considered as the largest indicator of absolute principal stresses. Fatigue modification was achieved by adjusting the value of infinite life, fatigue strength factor, load scale factor and interpolation curves (log-log, semi-log and linear curves). In so doing, accrued damage, blade life, safety factor and sensitivity factor were then computed. The modeling results yielded valuable information to analyses of creep-fatigue behavior in HP CT blades of short-haul aircraft fleet.

3.3 Results and discussions

The thermal results were depicted by temperature distribution on the surface of the CT blade. On the other hand, rotational analyses were evaluated by total deformation, equivalent (von-mises) stress and equivalent total strain, while creep-fatigue interactions were accounted for by; accrued damage, blade life, safety factor, equivalent alternating stress and sensitivity factor.

The lowest temperature on the CT blade surface was 826.7^{o}C at the root section, the suction side of the airfoil and tip of the CT blade. 829.76^{o}C was the highest recorded temperature at the leading edge of the tip and airfoil which gradually decreased to about 827.04^{o}C towards the trailing edge as conveyed in Fig. 3.9.

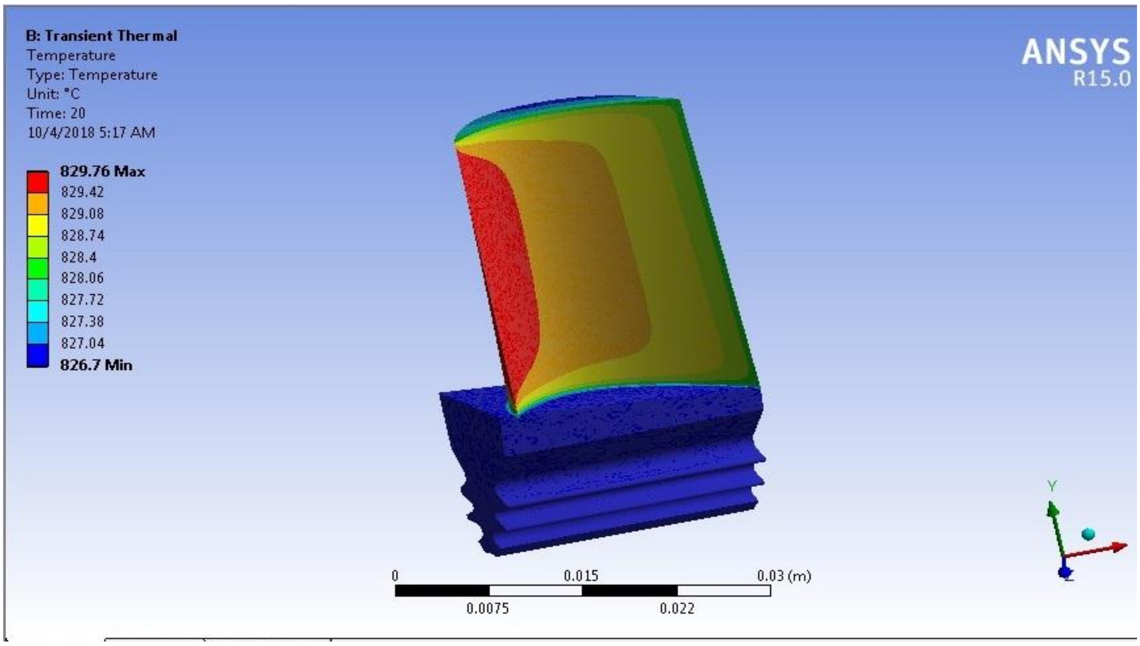

Figure 3. 9: Temperature distribution on the CT blade surface

The magnitude of maximum total deformation indicated was 5.3028 x 10^{-3} m at the tip of the leading edge as it appears in Fig. 3.10 and dropped to zero towards the root section.

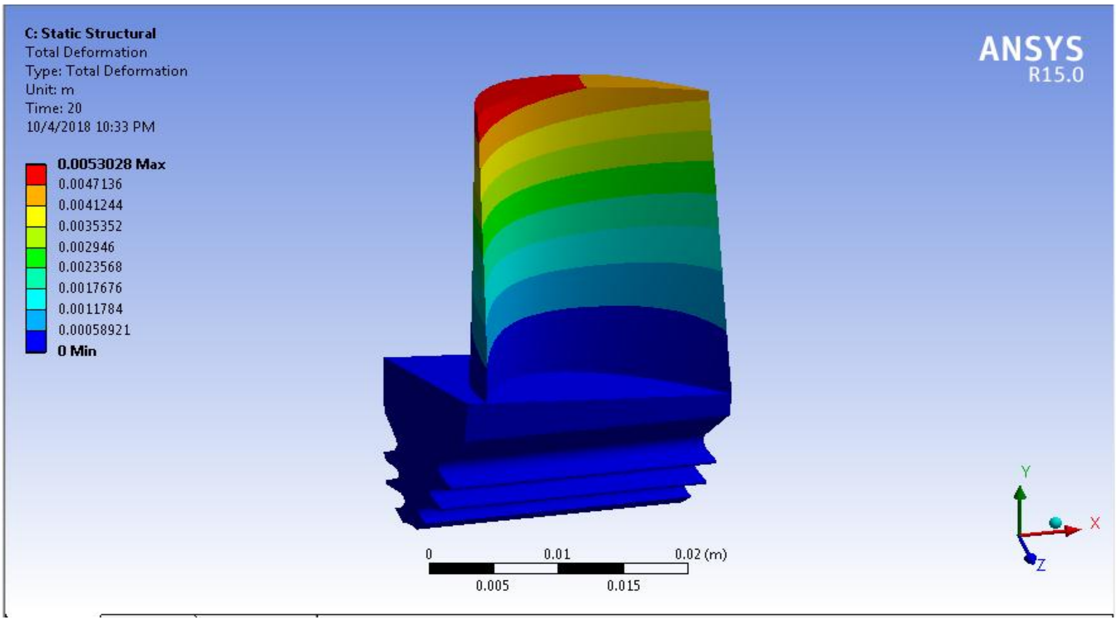

Figure 3. 10: Total deformation of the CT blade

The maximum equivalent (von-mises) stress of magnitude 9.3541 x 10^{7} Pa was noted at the leading-edge joint between the airfoil and the base as presented in Fig. 3.11. The entire root and the rest of the blade were relatively unaffected by these stresses.

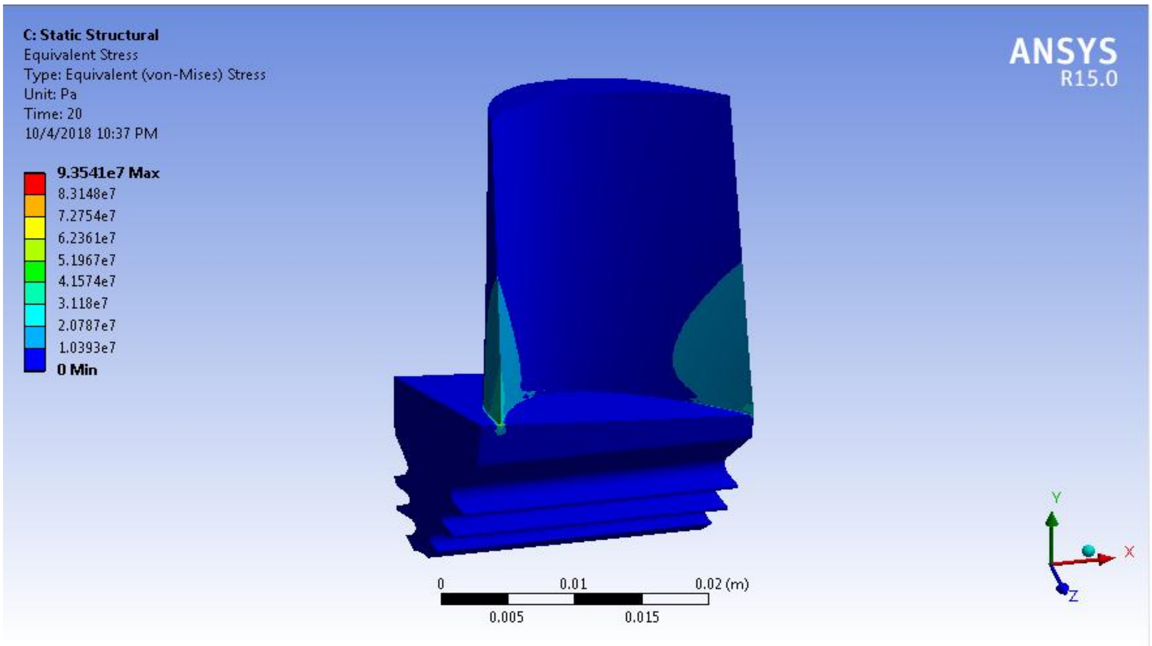

Figure 3. 11: Equivalent (von-mises) stress on CT blade

Equivalent elastic strain changed in similar fashion to match the von-misses stress with a maximum of 0.50453 m/m recorded at the leading-edge joint of the airfoil and the base denoted in Fig. 3.12.

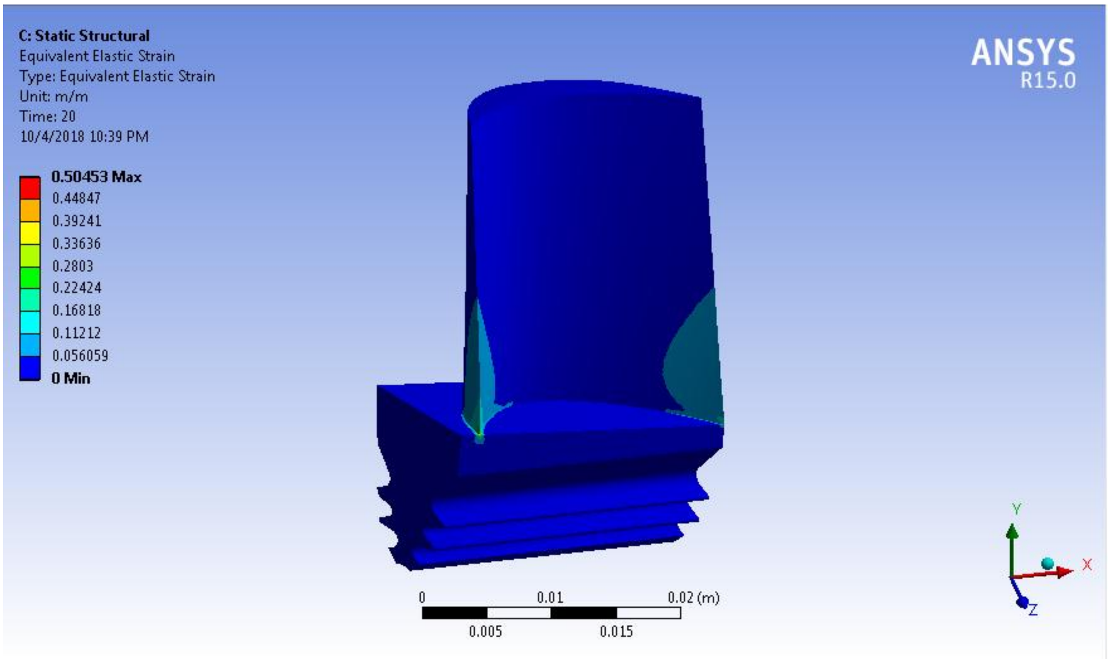
C: Static Structural
Equivalent Elastic Strain
Type: Equivalent Elastic Strain
Unit: m/m
Time: 20
10/4/2018 10:39 PM

Figure 3. 12: Equivalent elastic strain on the CT blade

Maximum damage of magnitude 1.5456 x 10^5 was observed at the leading-edge joint between the airfoil and the base as indicated in Fig. 3.13, with the rest of the blade unaffected.

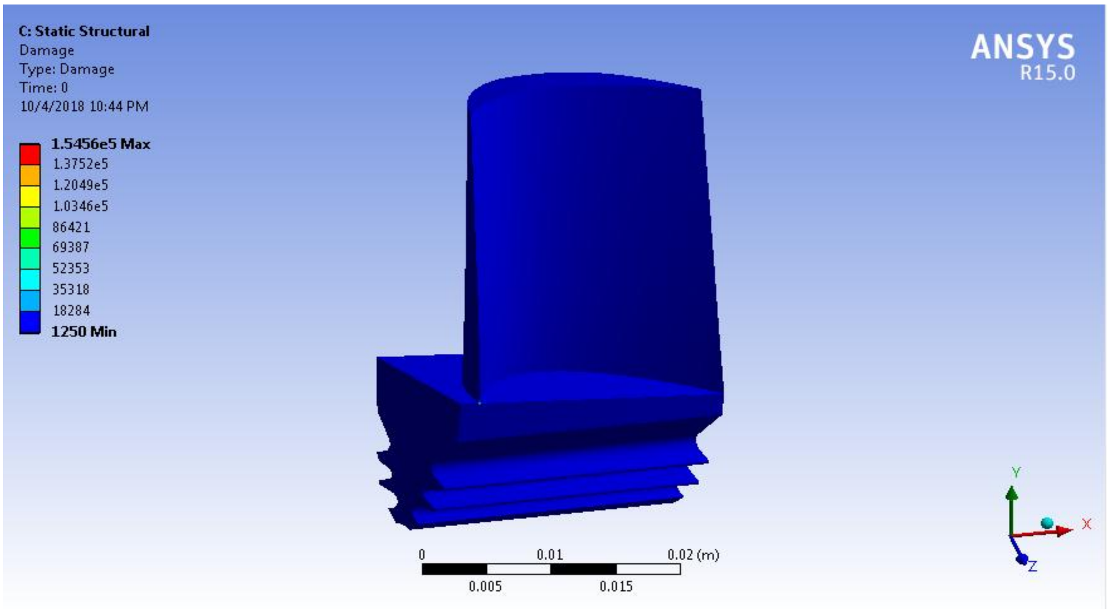
C: Static Structural
Damage
Type: Damage
Time: 0
10/4/2018 10:44 PM

Figure 3. 13: Accrued damage on the CT blade

Creep-fatigue life depicted in Fig. 3.14 indicated that the CT blade could have served for a minimum of 6470.1 creep-fatigue hours at most life threatened region; the leading-edge joint between the airfoil and the base, while the entire blade could serve much a longer period.

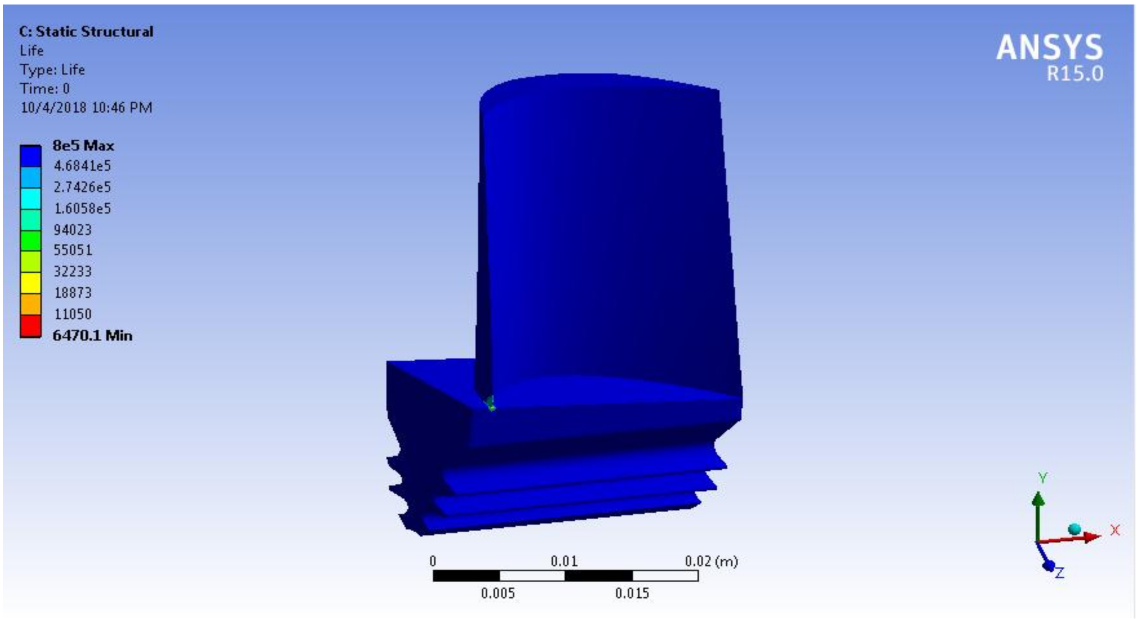

Figure 3. 14: CT blade life

The minimum load carrying capacity of the CT blade of magnitude 0.30717 was recorded at the leading-edge joint between the airfoil and the base as it appears in Fig. 3.15, which was closely followed by the airfoil and safer at then tip and root sections.

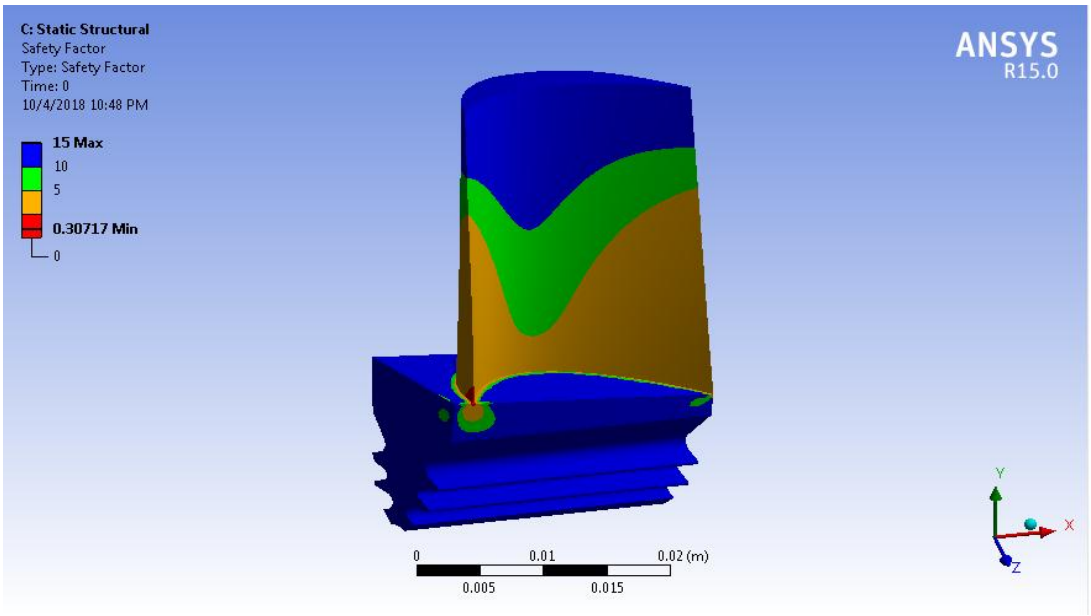

Figure 3. 15: Safety factor of the CT blade

A maximum equivalent alternating stress of magnitude 2.8062 x 10^8 Pa appearing in Fig. 3.16 was computed to establish creep-fatigue life, which verified that the weakest point of the blade was at the leading-edge joint between the airfoil and the base.

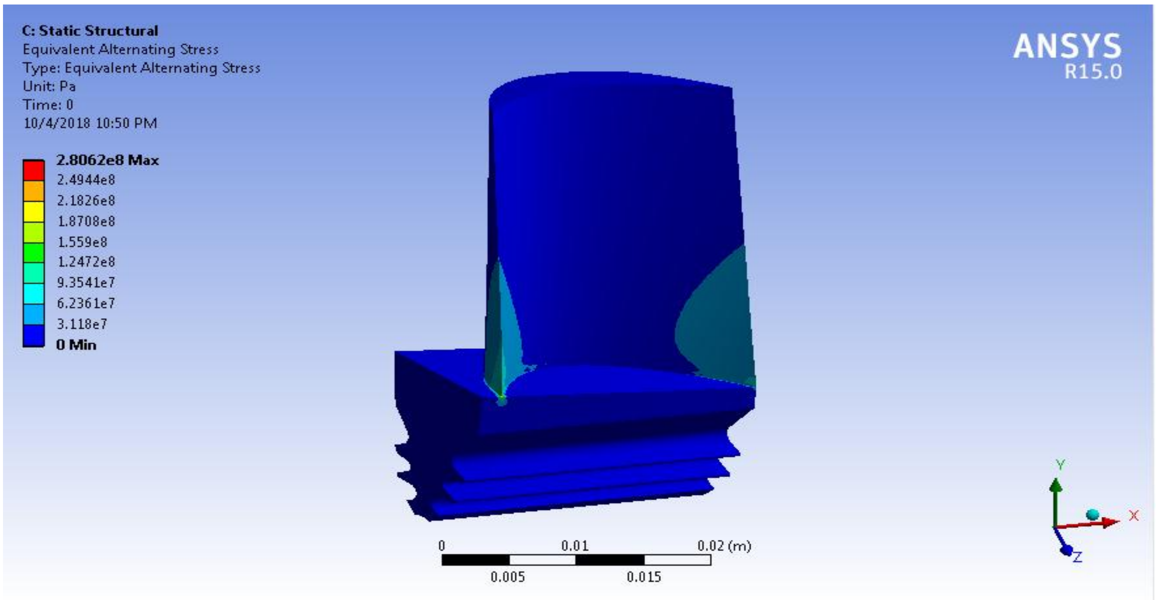

Figure 3. 16: Equivalent alternating stress on the CT blade

To sum it all up, the log-log creep-fatigue sensitivity curve in Fig. 3.17 presents the creep-fatigue life change with loading history in ranges of 50-150% at the critical locations of the CT blade. It is apparently evident then that when the loading is low, the life is longer and when the loading is high, CT blade life significantly dips in a corresponding manner.

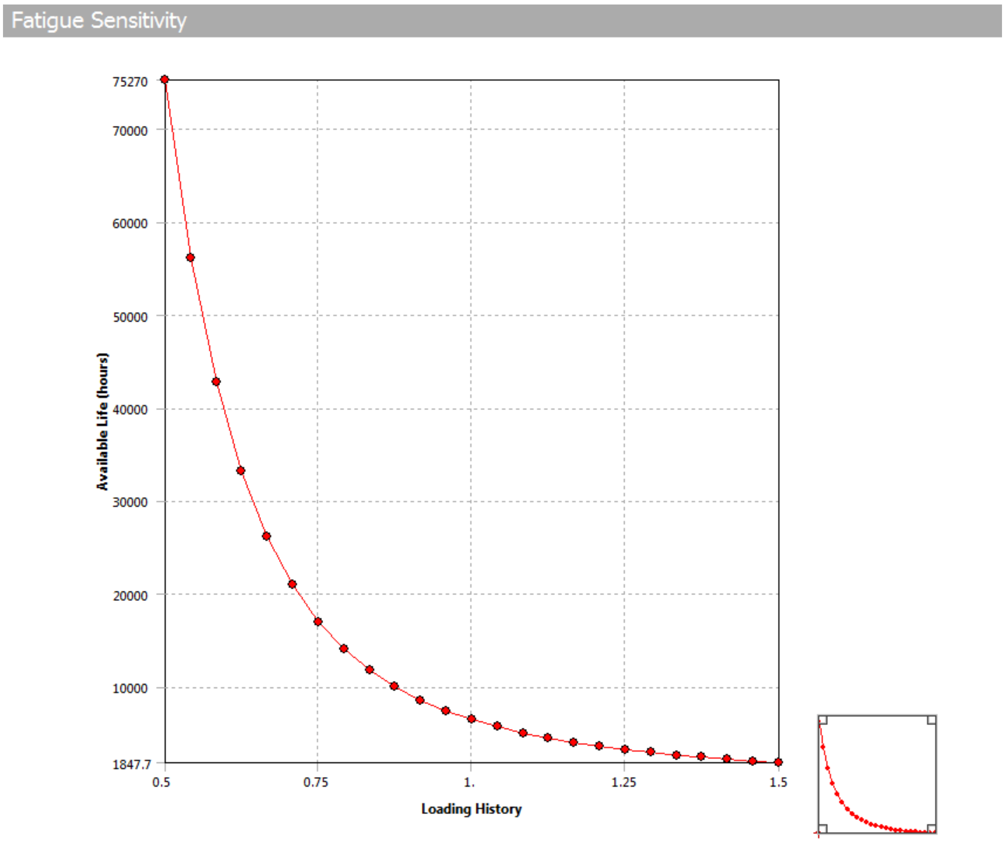

Figure 3. 17: Sensitivity factor

3.4 Closure

Chapter 3 devotes to sequential execution of thermo-mechanical FE stresses analyses. The results depicted that thermal stresses were concentrated on the leading edge than the trailing edge. The tips were seemingly too greatly affected as compared to the airfoil and the base. Stress and strain concentration were centered at the leading-edge joint between the airfoil and the base as a result of rotational speeds. The results further suggested that the CT blade could have served for another 1.44% of the actual life it was in service. The following chapter characterizes microstructural and metallurgical of the protective coating and the substrate material of the CT blade.

CHAPTER 4: MICROSTRUCTURAL AND METALLURGICAL CHARACTERIZATION OF THE PROTECTIVE COATING AND SUBSTRATE MATERIAL

4.1. Preamble

This chapter characterizes the degradation on the diffusion aluminide protective coating and the substrate material of the CT blades. The transverse and longitudinal sections of CT blade samples were treated to detailed XRF, XRD, EDS-SEM examinations. These investigations enabled identify the morphology, attacks, present, lost and intruder elements and their roles in premature failure of the protective coating and substrate material of the CT blades.

4.2. CT blade specimens

Polycrystalline Inconel 713LC Ni-base HP, PT6A-114A engine CT blades used in this research appearing in Fig. 4.1 were collected from Vector Aerospace Kenya Limited after premature retire from service at 6378 creep-fatigue hours against a preset 10000 creep-fatigue hours.

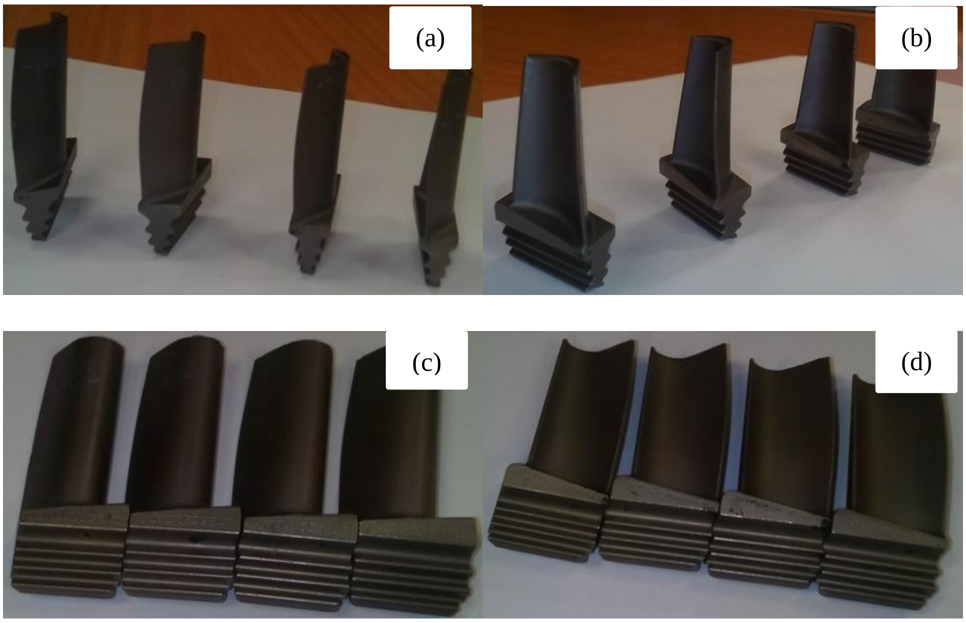

Figure 4. 1: (a) and (b) The suction and pressure sides of front view respectively (c) and (d) The suction and pressure sides of rear view respectively

4.3 Experimental procedures and equipment

4.3.1. XRF analyses

XRF analyses were conducted to confirm the existence of various elements that constitute the bulk of the protective coating and the substrate material of the CT blades. The method is both qualitative and quantitative. In the qualitative aspect; fluorescent spectra are identified by accurately singling out peak tops which are converted to energy indicators from set standard reference elements and known energy calibration pattern, the $K\propto$. With the aid of the spectrum analysis software, identification of unknown elements from X-ray energy level data bases is then executed. This analyses follow least square fitting technique as expressed in Eq. 4.1 (Hardwicke et al., 2013; Juliš et al., 2010; Lee, 2006)

$$E(ekV)=A+BX \qquad 4.1$$

Where A=0.01000; B=0.00216(ekV/levels); X=number of levels.

The quantitative analysis converts net peak intensities into percentage concentration by subtracting the backgrounds using mathematical algorithms. This involves theoretical calculation of elemental constitution using key parameters of the X-ray intensity associated with instrument characteristics; the photoelectric absorption coefficient, mass absorption and fluorescence yield rate. Then, against known reference standards, the parameters are adjusted to reflect the spectra (Hardwicke et al., 2013; Juliš et al., 2010; Lee, 2006).

The S8 Tiger Bruker AXS, XRF machine shown in Fig. 4.2 was used for data acquisition in compliance to ASTM E2465-13. The samples were cleaned and placed in 25mm plastic cup sample holder and covered with Prolene seal at standard temperature and pressure (STP). Measurements were effected using the quant-express method. Since the system had been calibrated and passed the STG2 standard test, full analysis at He25mm calibration, QE-Check-He25mm was applied for sample scan with the best detection analysis being realized at He34mm. Bruker AXS GmbH software Spectra Plus, Version 3.0.2.19 © 2012, was utilized for qualitative and quantitative analyses of peak identification, element detection and normalization. This analytical technique relies on elemental composition ratios to indicate the bulk material.

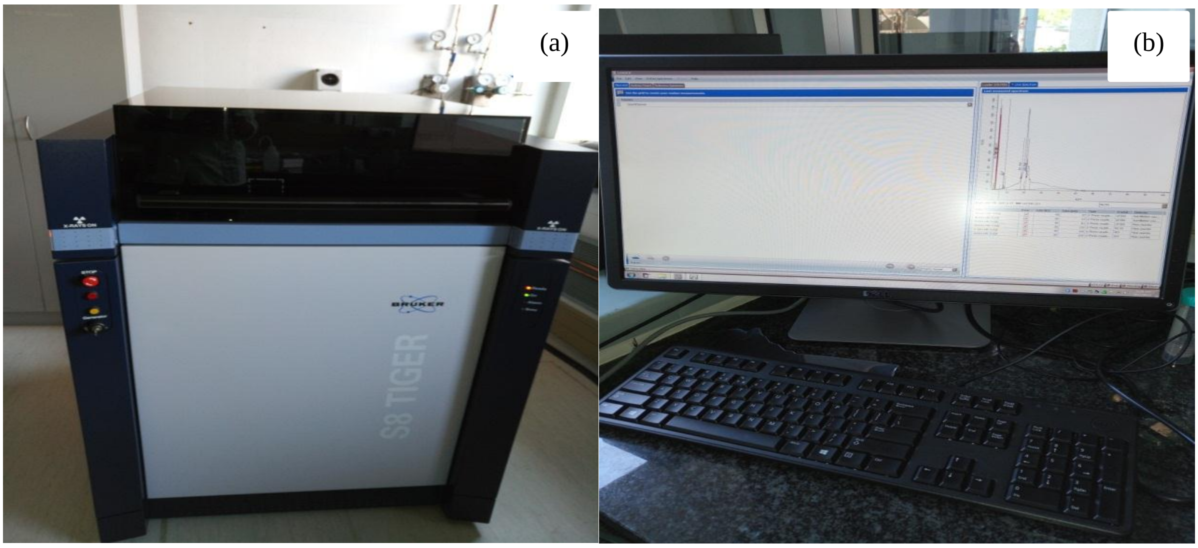

Figure 4. 2: (a) Bruker AXS, S8 Tiger XRF machine (b) Display of sample data

4.3.2. XRD analyses

An XRD machine illuminates a beam of X-rays on a single crystal which generates spots whose positions are determined by the size and shape of the unit cell and symmetry. The arrangement of atoms within a crystal are used to define the intensity of the diffracted spots and the positions of atoms in the unit cell. Similar to the XRF, both qualitative and quantitative data are acquired.

In qualitative analyses, the peak positions in a powder pattern representing a phase is determined by the size, shape, and symmetry of the unit cell while the peak intensities are determined by the arrangement of atoms within the cell. In case a phase mixture occurs, diffraction patterns overlap making it possible to identify the components of a mixture. Using search and matching methods from powder diffraction file (PDF) and contemporary algorithms, compound giving rise to the specific pattern are singled out. Quantitative analyses measure and makes summation of peak intensities arising from every variation of concentration in phase mixtures.

The Empyrean XRD machine, PANalytical, Expert Pro, appearing in Fig. 4.3 was used for data acquisition. The samples were cleaned, placed on a zero-background holder and pressed to make a 5mm radius circle at STP in conformity to ASTM E1834-11. Scan Axis Gonio settings were applied prior to spinning with KαCu radiation from start position 33.64 [°2θ] to end position 93.08 [°2θ] with a Step Size of 0.02 [°2θ] and Step Time of 1.00 [s]. X'Pert High Score Plus, V4.5 software was then used for analyses.

Figure 4. 3: (a) PANalytical Expert Pro XRD machine (b) Display of sample data

4.3.3. Energy Dispersive Spectroscopy-Scanning Electron Microscopy analyses

4.3.3.1. The non-sectioned specimens

The non-sectioned samples of the CT blades majorly represented the diffusion aluminide protective coating. The samples were cleaned ultrasonically with ethanol, dried and subjected to SEM for surface and sub-surface damage identification and quantification at the tips, airfoils and bases. The micrographs then subjected for analyses using an EDS enabled SEM, ZEISS; Gemini 500 illustrated in Fig. 4.4 in line with ASTM E1508.

Figure 4. 4: ZEISS Gemini 500, EDS enabled SEM

4.3.3.2 The sectioned specimens

The sectioned specimens of the CT blades represented both the diffusion aluminide protective coating as well as the substrate material. The samples for both transverse and longitudinal sections were cleaned and marked as presented in Fig. 4.5 (a) and (b) respectively (Qu et al., 2013; Sexton et al., 2002).

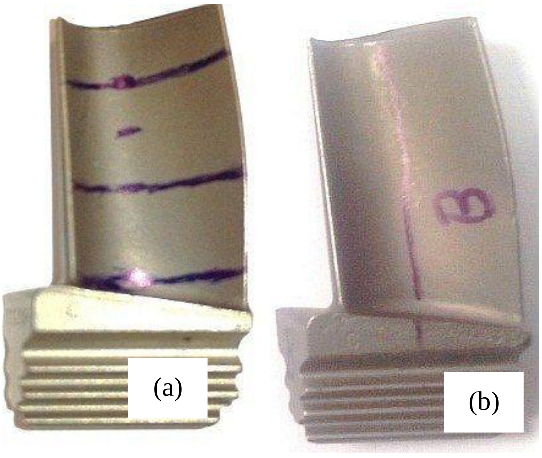

Figure 4. 5: Marked samples for sectioning (a) Transverse (b) Longitudinal

The sectioned samples of the CT blades were treated to a number of procedures in conformity to ASTM E3-11, which entailed; sectioning, mounting, grinding, polishing and carbon coating. The transverse sections were carried out at intervals of

$33.3\%, 66.7\%\ and\ 83.3\%$ from the root of the CT blades whose heights are $36mm$ to give a fair representation of the base, airfoil and tip sections. The longitudinal section on the other hand was through the mid-span of the CT blade. A Dace Technologies, Picco 155P precision cutter, in Fig. 4.6 was utilized.

Figure 4. 6: Dace Technologies, Picco 155P, precision cutter

Mounting was carried out in hot grey acrylic thermoplastic resin to preserve the edges and make recording of specimen details possible with the aid of Struers Cito Press 30, mounting machine in Fig. 4.7.

Figure 4. 7: Struers Cito Press 30, hot compression mounting machine

Automatic simultaneous grinder and polisher, Struers Tegramin 30, in Fig. 4.8 was used to yield superior flatness, preserve the edges and clearly reveal the microstructure in Table 4.1 was adopted.

Figure 4. 8: Struers Tegramin 30, automatic grinder and polisher

Table 4. 1: Grinding and polishing procedures (Struers, 2017)

Procedure	**Time (Seconds)**	**Force (Newtons)**	**Surface**
Step 1	180	40	MD Piano 500
Step 2	330	20	MD Piano 1200
Step 3	180	40	MD Largo $9_{\mu m}$ suspension
Step 4	180	30	MD Dac $3_{\mu m}$ (polishing)
Step 5	600	Gravity	Colloidal Silica on Vibratory Polisher GIGA-1200

Finally, Quorum Technologies, Q300T ES carbon-coater, in Fig. 4.9 was used to enhance signal and improve surface resolution of the sections at microscopic level prior to exposure to the EDS enabled SEM for micrography and element mapping. Literature suggests that carbon coating is sufficient for Ni-base alloys, while cost is significantly cut in comparison to gold coating.

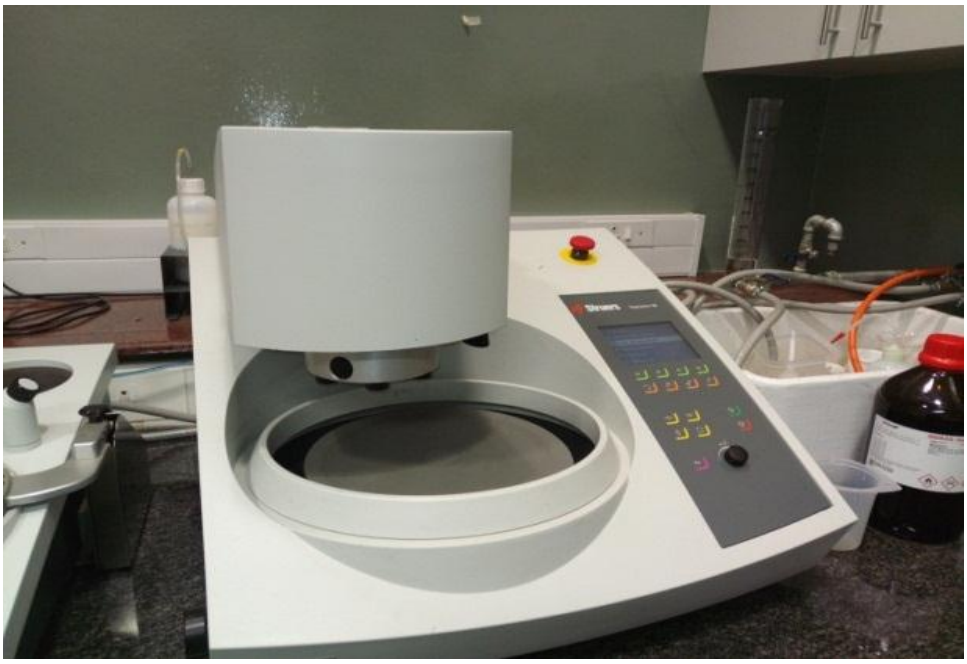

Figure 4. 9: Quorum Technologies, Q300T ES carbon-coater

Figs. 4.10 and 4.11 illustrate the final prepared samples of the transverse sections at the tip, airfoil and base as well as the longitudinal section of the CT blades respectively ready for micrography.

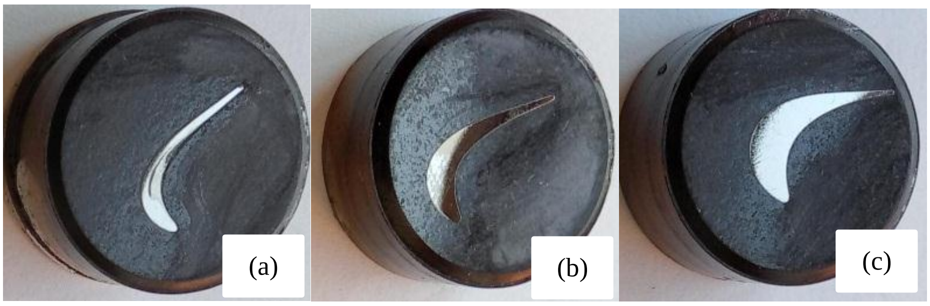

Figure 4. 10: Transverse sections (a) Tip (b) Airfoil (c) Base

Figure 4. 11: Longitudinal section

4.4. Results and discussions of the non-sectioned protective coating

4.4.1. XRF analyses

The XRF captured the bulk constituent elements of both the protective coating and the substrate material of the CT blades and were compared against the manufacturer's original specifications in Table 4.2.

Table 4. 2: % comparison between original composition of Inconel 713LC and XRF

	Ni	**Al**	**Co**	**Si**	**Cr**	**Ti**	**Mo**	**Fe**	**C**	**B**	**P**	**S**	**Nb**	**Zr**
Original	74	6.1	-	-	12.5	0.8	4.2	-	0.05	0.012	0.006	0.004	2.1	0.1
XRF	49.93	23.3	9.73	6.15	4.91	2.59	2.26	0.37	-	-	-	-	-	-

In conformity with the original material's composition, the bulk base elements; Ni, Al, Cr, Ti and Mo were present. A number of trace constituent elements such as Zr, Nb, C and B were however undetected, possibly from decomposition or active replacement by more reactive elements. Intruder elements such as Co, Fe and Si similarly found their way into the spectrum, possibly from fuel constituents or flight environment. The dynamics of decrease and increase of the constituent elements could have been as a result of position of the scanned surface in respect to heat exposure along the profile of the CT blades and the activity level of $NiAl$ inward or outward diffusion of during service.

4.4.2. XRD analyses

Three compounds formed the bulk of the peaks in XRD analyses as summarized in Table 4.3. A compound of Aluminium, Chromium and Nickel, who's reference code is 98-011-0813, with a chemical formula of $Al_{0.67}Cr_{0.67}Ni_{0.67}$ was predominant at peaks 1, 4, 7, 8, 9 and 10. Molybdenum, Vanadium and Silicon compound, with a reference code of 98-007-6378 and a chemical formula of $Mo_3Si_2V_3$ matched peaks 3, 5, and 9. Lastly, Titanium and Aluminium compound, with a reference code of 98-018-9695 and chemical formula of Al_1Ti_3 matched peaks 2 and 6. These results confirmed coexistence of active inward Al diffusion and outward Ni diffusion as well as presence of the alloy modifying elements Cr, Mo, V and Ti. Active inward diffusion of Al relative to Ni outward resulted to formation of more brittle carbides at the tips and the airfoils compared to the bases leading to microcrack formation which coalesced into cracks and eventually disintegration of the protective coating.

Since the $Al_{0.67}Cr_{0.67}Ni_{0.67}$ compound was dominant and thermodynamically stable, the resultant oxide, $Al(Cr)_2O_3$ is of excellent protective properties. This played a role in oxidation and corrosion resistance at the bases. The carbides of Mo and V are an excellent strength enhancer for Inconel 713LC, nonetheless, less of their pronouncement may have been a key contributor to strength loss in the protective coating. The least and smallest peaks represented by Ti and Al compounds indicate depletion of the most needed anti-oxidation agent most required at the tips to counter micro-cracking, disintegration and spalling. Fig. 4.12 illustrates the spectrum on which the ten peaks and their relative positions were identified.

Table 4. 3: XRD identified peaks, their positions and respective counts

Peak Number	**1**	**2**	**3**	**4**	**5**	**6**	**7**	**8**	**9**	**10**
Position [°2θ]	30.86	39.41	41.84	44.45	45.99	48.80	55.31	64.74	73.40	82.02
Height (Counts)	213.2	219.0	1705.7	24025.0	2883.7	665.6	1108.9	404.0	243.4	6021.8

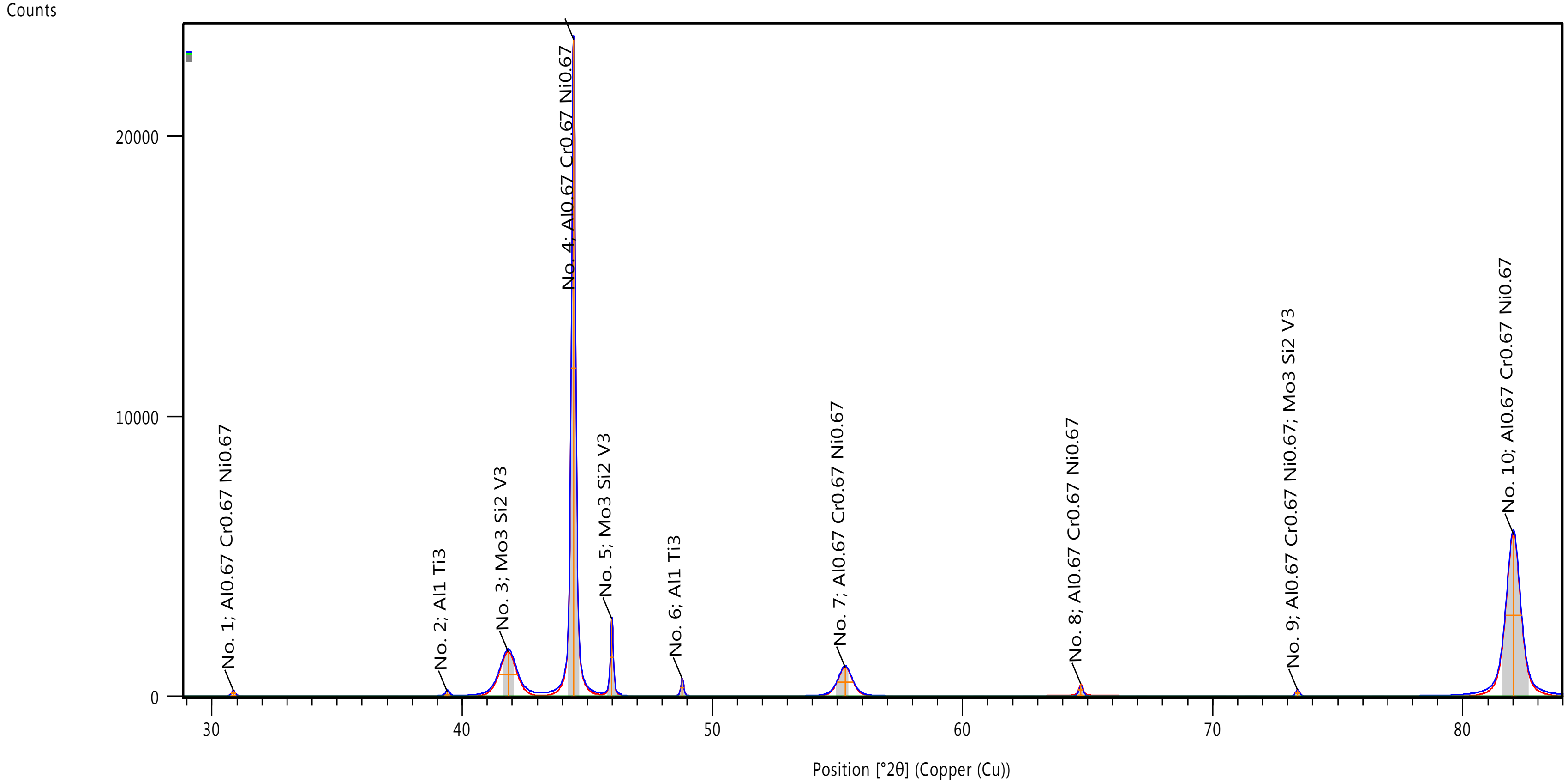

Figure 4. 12: XRD spectrum of non-sectioned diffusive aluminide protective coating

4.4.3. Energy Dispersive Spectroscopy-Scanning Electron Microscopy analyses

4.4.3.1. The Tip

The non-sectioned tips had severely disintegrated protective coating as illustrated in Fig. 4.13 with hot corrosion attack as revealed in Fig. 4.14.

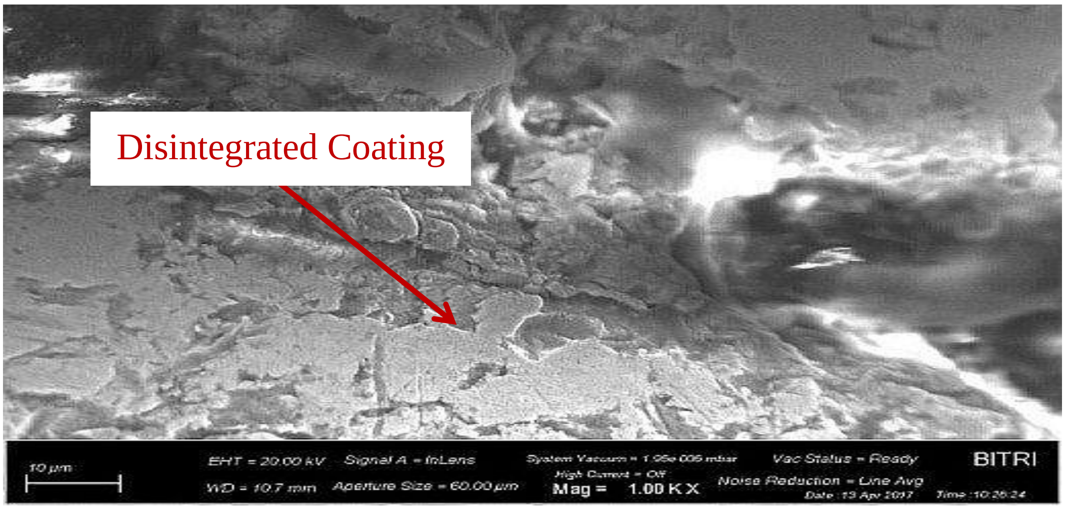

Figure 4. 13: Non-sectioned tip

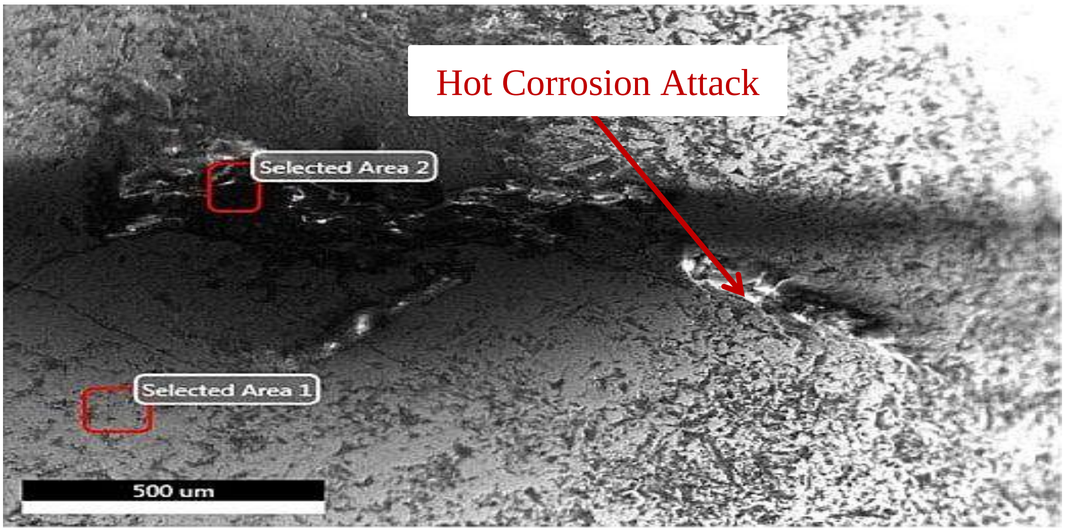

Figure 4. 14: EDS micrograph of the leading edge at the tip

The EDS Spectrum of the leading edge at the tip in Fig. 4.15 indicated that selected area 1; the hot corroded patch had reduced carbides of Mo and Co with increase in Ti and Cr. There was also a rise in oxides of Al, with minute occurrences of Na, Mg, Si, Ca, V, and Fe oxides, which possibly had been introduced from fuel or the flight environment. Similarly, in this region both active inward diffusion of Al and outward diffusion of Ni was prevalent.

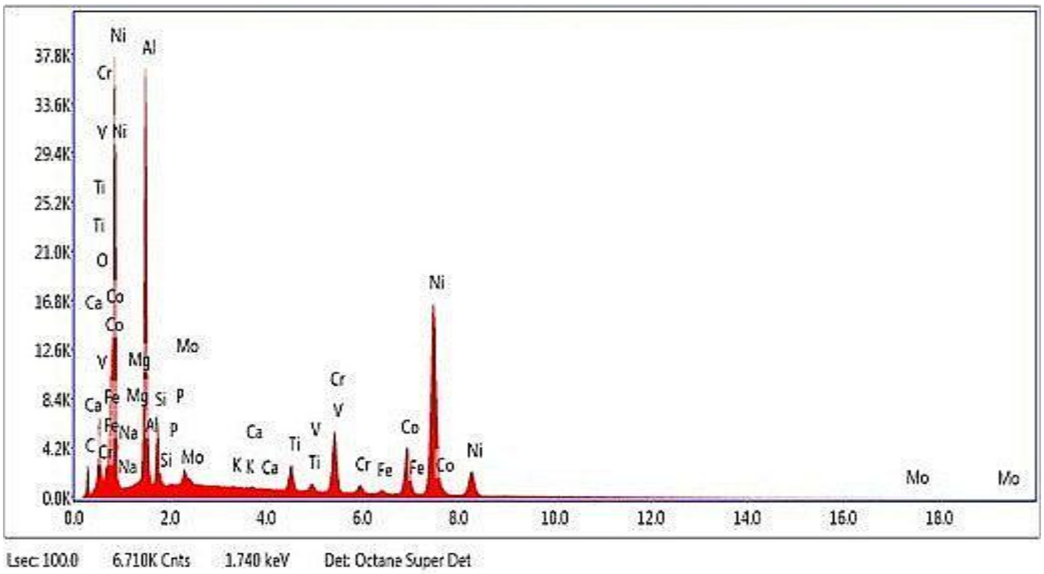

Figure 4. 15: EDS spectrum of selected area 1

At selected area 2 adjacent to hot corroded patch as conveyed in Fig. 4.16, there was a remarkable reduction in carbides of Mo, Co, Ti and Cr. Oxides of Na, K, Ca had in turn significantly escalated, while those of Mg, Si, V had dwindled. Chloriding effect had developed probably from fuel constituents or flight environment too. This region nonetheless had no active inward of Al nor outward diffusion of Ni.

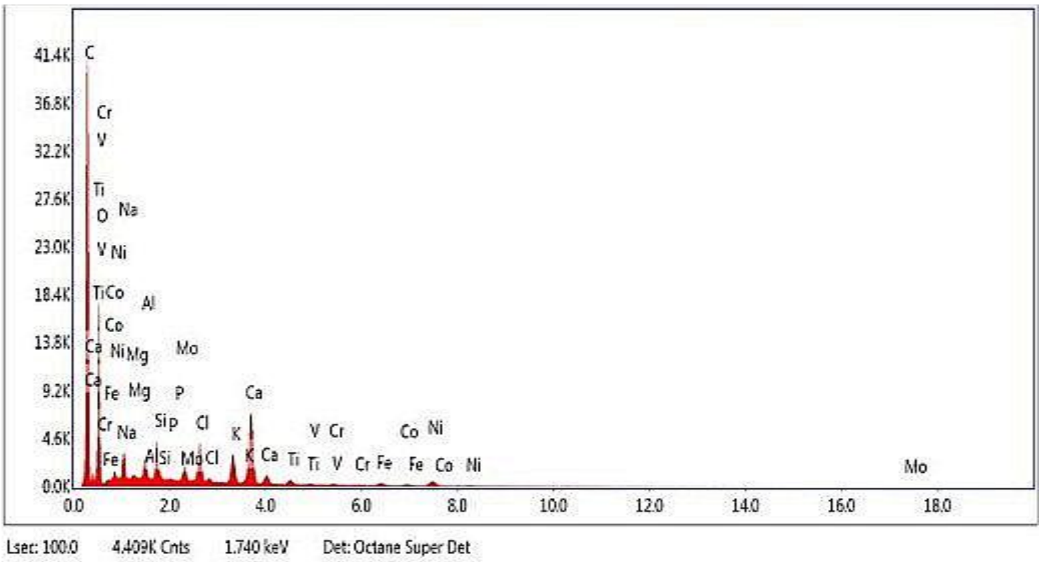

Figure 4. 16: EDS spectrum of selected area 2

The EDS elemental compositions of the tip for selected areas 1 and 2 are as tabulated in Table 4.4 as were conveyed in Figs. 4.15 and 4.16.

Table 4. 4: Elemental composition of the tip for selected areas 1-2

Element	**CK**	**OK**	**NaK**	**MgK**	**AlK**	**SiK**	**MoL**	**ClK**
% Weight Selected Area 1	10.2	5.5	1.0	0.5	19.7	3.0	1.2	-
% Weight Selected Area 2	54.4	31.4	2.0	0.2	0.7	1.1	0.8	1.5
Element	**KK**	**CaK**	**TiK**	**VK**	**CrK**	**FeK**	**CoK**	**NiK**
% Weight Selected Area 1	0.0	0.1	1.8	0.4	5.8	0.4	8.3	41.8
% Weight Selected Area 2	1.4	4.5	0.3	0.4	0.1	0.4	0.2	1.0

The non-sectioned tip also had a pit hole as it appears in Fig. 4.17. The area adjacent to the hole in Fig. 4.18 denoted abundance of Al and Ca oxides. Trace oxides of Na, Mg, Si, V, Fe and Cu were noted. Oxides of P, S, together with Cl were distinctively missing. In this region both active inward diffusion of Al and outward diffusion of Ni were evident.

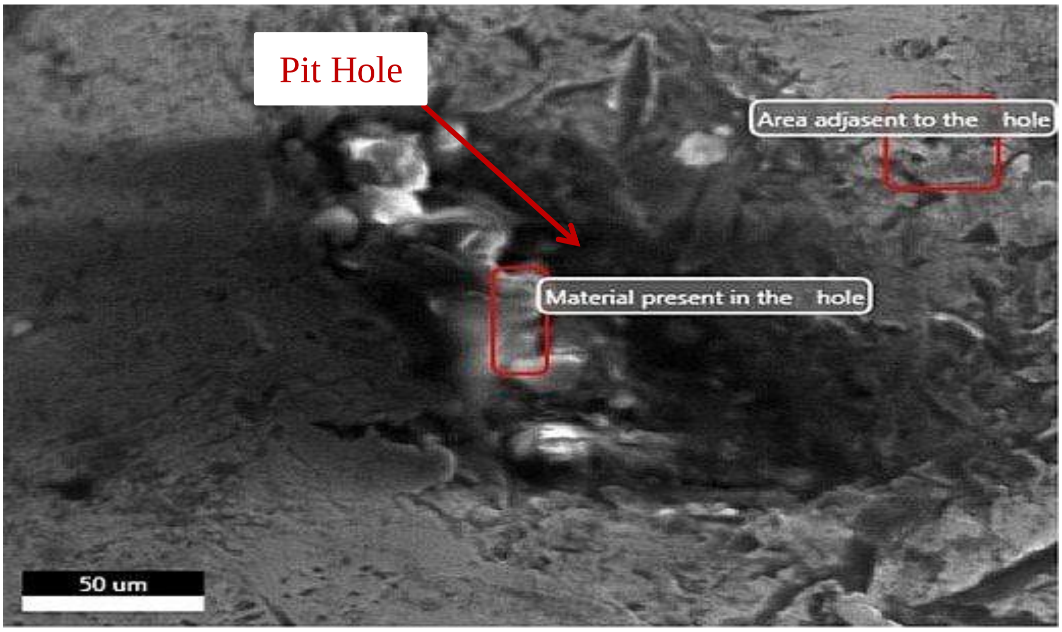

Figure 4. 17: Pit hole on non-sectioned tip

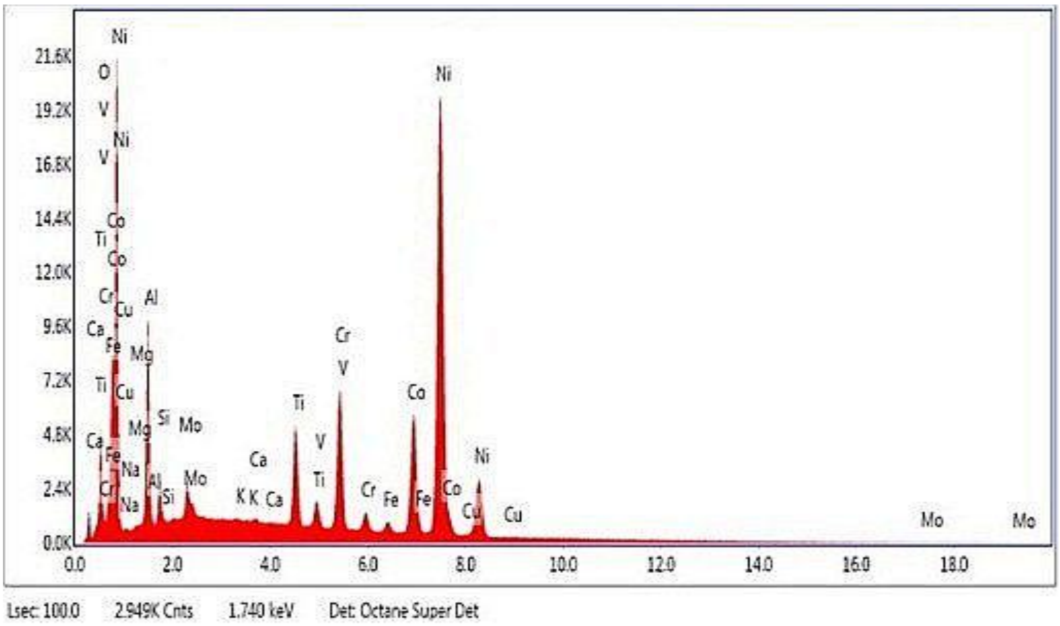

Figure 4. 18: EDS spectrum of the material adjacent to the hole

The material present in the hole in Fig. 4.19 exhibited active oxide deposition of Na, Mg, Si, P, S, Ca alongside chloriding effect. However, passive inward diffusion of Al as well as outward diffusion of Ni was noted.

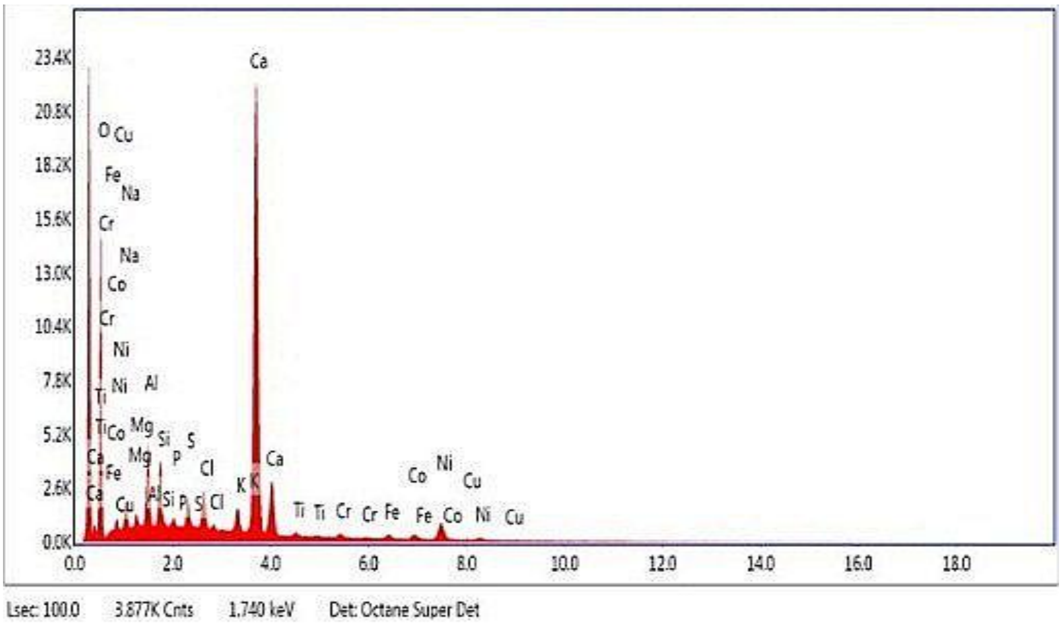

Figure 4. 19: EDS spectrum of the material in the hole

Table 4.5 reports the EDS elemental composition of the material adjacent to and in the hole respectively in Figs. 4.18 and 4.19.

Table 4. 5: Elemental composition of the material adjacent to and in the hole

Element	**OK**	**NaK**	**MgK**	**AlK**	**SiK**	**MoL**	**PK**	**SK**	**ClK**
% Weight (Adjacent)	4.3	0.9	0.2	7.2	1.2	1.8	-	-	-
% Weight (In the hole)	48.9	3.3	0.8	3.3	2.3	-	0.3	1.0	1.6
Element	**KK**	**CaK**	**TiK**	**VK**	**CrK**	**FeK**	**CoK**	**NiK**	**CuK**
% Weight (Adjacent)	0.1	0.1	4.0	0.8	7.8	0.8	13.0	57.6	0.3
% Weight (In the hole)	1.1	30.6	0.3	-	0.5	0.7	0.9	4.1	0.1

4.4.3.2. The Airfoil

The non-sectioned airfoil had evidences of pore as captured in Fig. 4.20. Microcracks had developed and coalesced into cracks as depicted in Fig. 4.21. Selected areas 1 and 2 which were used for EDS analyses as presented in Fig. 4.22.

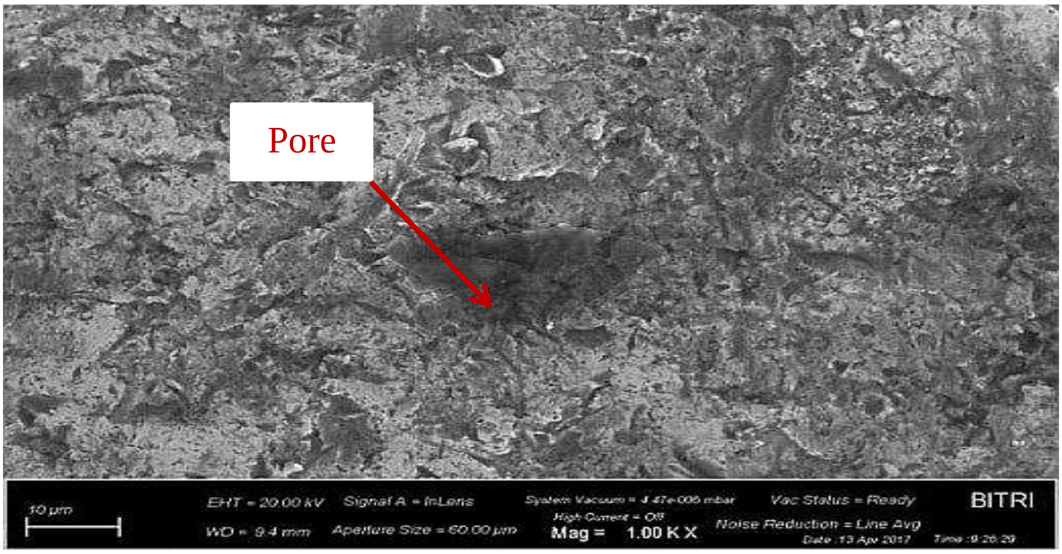

Figure 4. 20: Non-sectioned airfoil (Image 1)

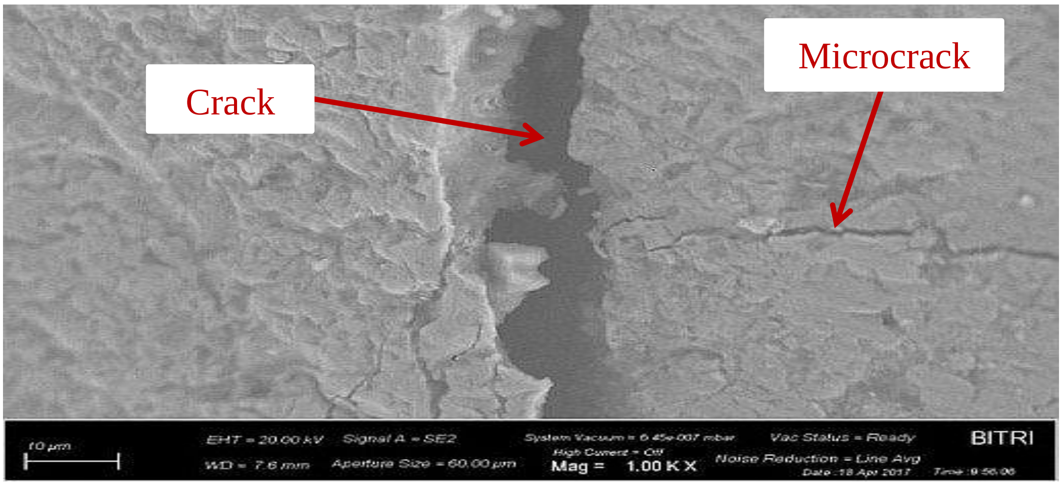

Figure 4. 21: Non-sectioned airfoil (Image 2)

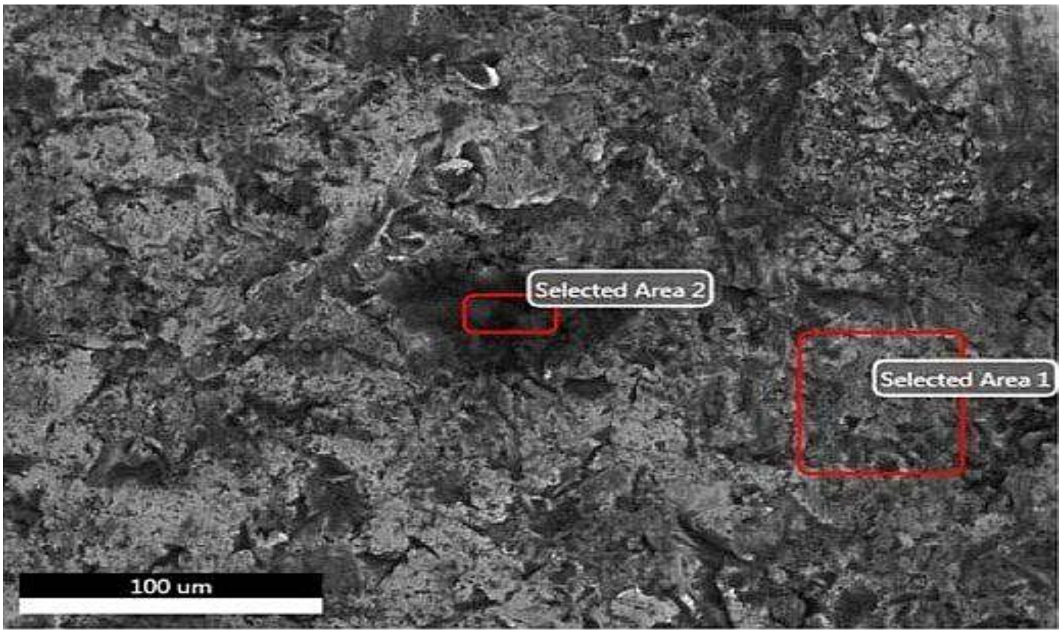

Figure 4. 22: EDS micrograph of the airfoil at selected areas 1 and 2

In Fig. 4.23, the EDS spectrum of selected area 1 indicated formation of Mo, Ti, Cr and Co carbides alongside Al oxide in abundance. Trace oxides of Na, Mg, Si, P, K, Ca, and Fe were also identified and suspected to be from fuels during combustion or flight environment. Very active outward Ni diffusion was evident.

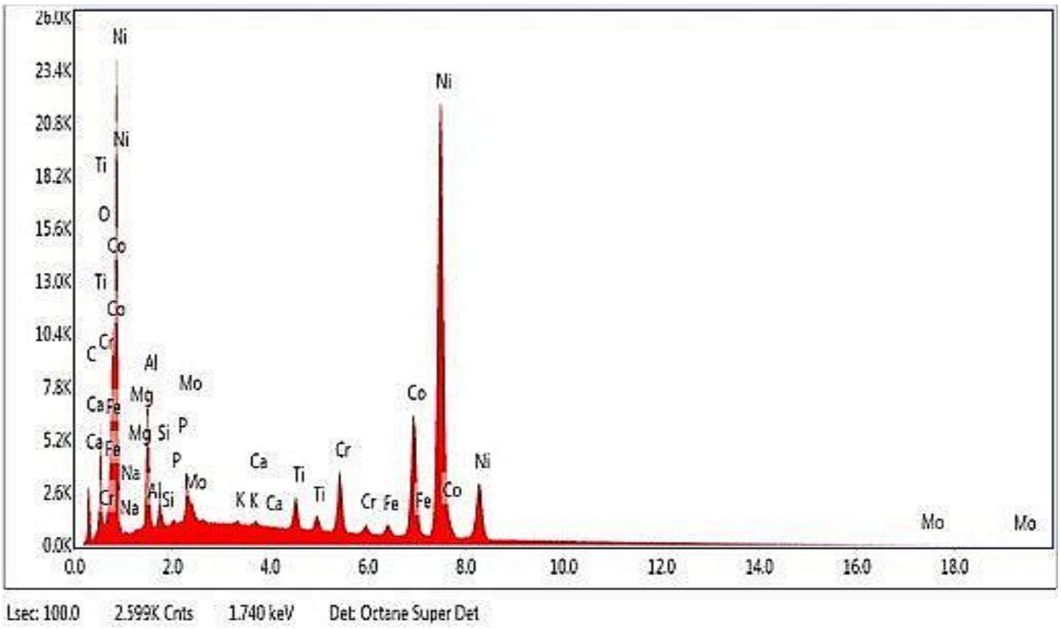

Figure 4. 23: EDS spectrum of selected area 1 in the pore

Selected area 2, appearing in Fig. 4.24 revealed reduced carbides of Mo and Co with, significant increase in those of Ti and Cr in relation to selected area 1 which was adjacent to the pore. An increase in oxides of Na, Mg, Si, P, K, Ca, and Fe in addition to chloriding was evident. A significant reduction in outward diffusion of Ni was noted than inward diffusion of Al, making the protective coating brittle and susceptible to cracking and disintegration thereof.

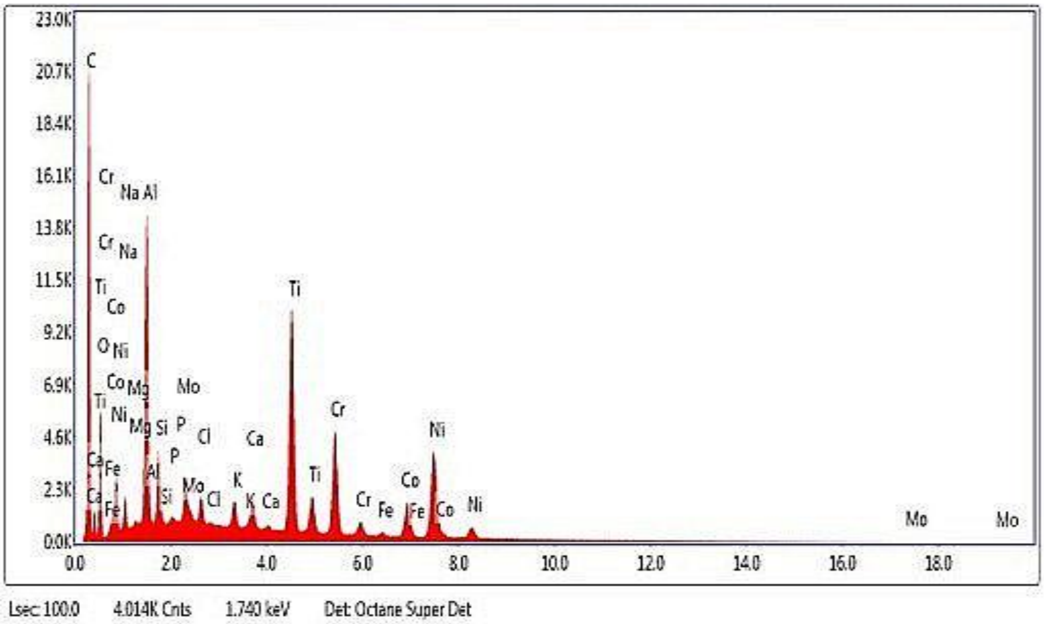

Figure 4. 24: EDS spectrum of selected area 2; adjacent to the pore

Table 4.6 reports of the elemental composition of the airfoil at selected areas 1 and 2 in Figs. 4.23 and 4.24.

Table 4. 6: Elemental composition of the airfoil at selected areas 1-2

Element	**CK**	**OK**	**NaK**	**MgK**	**AlK**	**SiK**	**PK**	**MoL**
% Weight Selected Area 1	9.7	4.9	1.0	0.3	5.0	0.9	0.1	2.1
% Weight Selected Area 2	45.9	11.8	1.5	0.1	5.9	1.2	0.1	1.6
Element	**ClK**	**KK**	**CaK**	**TiK**	**CrK**	**FeK**	**CoK**	**NiK**
% Weight Selected Area 1	-	0.2	0.2	1.3	3.2	0.6	12.9	57.4
% Weight Selected Area 2	0.6	0.7	1.0	9.1	6.1	0.2	3.6	10.5

4.4.3.3. The Base

The EDS analyses of the non-sectioned base in Fig. 4.25 indicated high deposits of Al oxides alongside traces oxides of Na, Si, K, Ca, Ti, V, Cu and Fe which possibly had been introduced from fuel or flight environment. Presence of Fe led to formation of Ni-FCC dendrites known to actively replace Mo and Cr. However, rich content of Mo, Ti, Cr, Co were great inhibitors of corrosion and oxidation. Active outward diffusion of Ni was rampant relative to inward diffusion of Al. As a result, the bases had good ductility of the protective coating at elevated temperature, making them less likely to cracking and disintegrating.

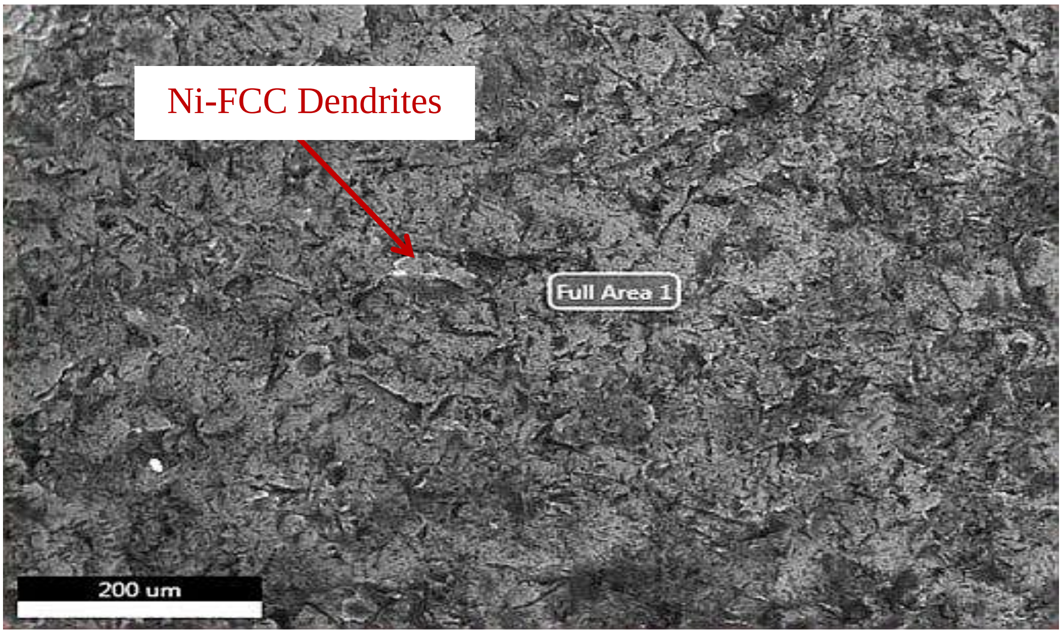

Figure 4. 25: EDS micrograph of the non-sectioned base

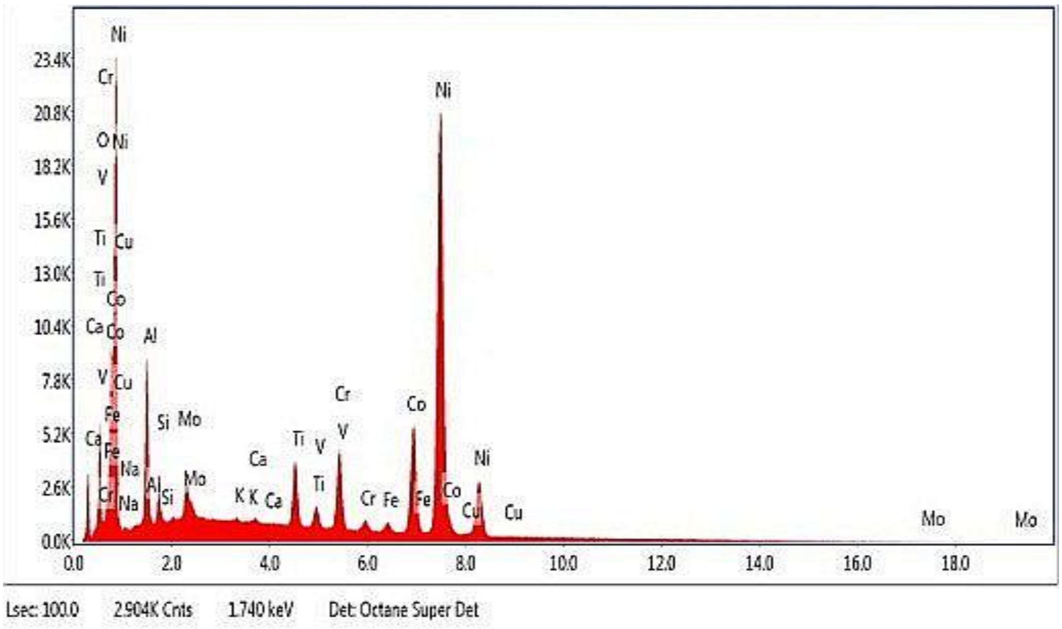

Figure 4. 26: EDS spectrum of non-sectioned base

Table 4.7 presents the elemental composition of the non-sectioned base in Fig. 4.26.

Table 4. 7: Elemental composition of the non-sectioned base

Element	**OK**	**NaK**	**AlK**	**SiK**	**MoL**	**KK**	**CaK**
% Weight	4.8	1.0	6.6	1.3	2.4	0.1	0.2
Element	**TiK**	**VK**	**CrK**	**FeK**	**CoK**	**NiK**	**CuK**
% Weight	3.0	0.8	4.8	0.8	12.6	61.4	0.4

4.5. Results and discussions of sectioned protective coating

4.5.1. The Tip

The tip section had noticeable multiple micro-cracks, some of which were already leading into the substrate material as it appears in Figs. 4.27.

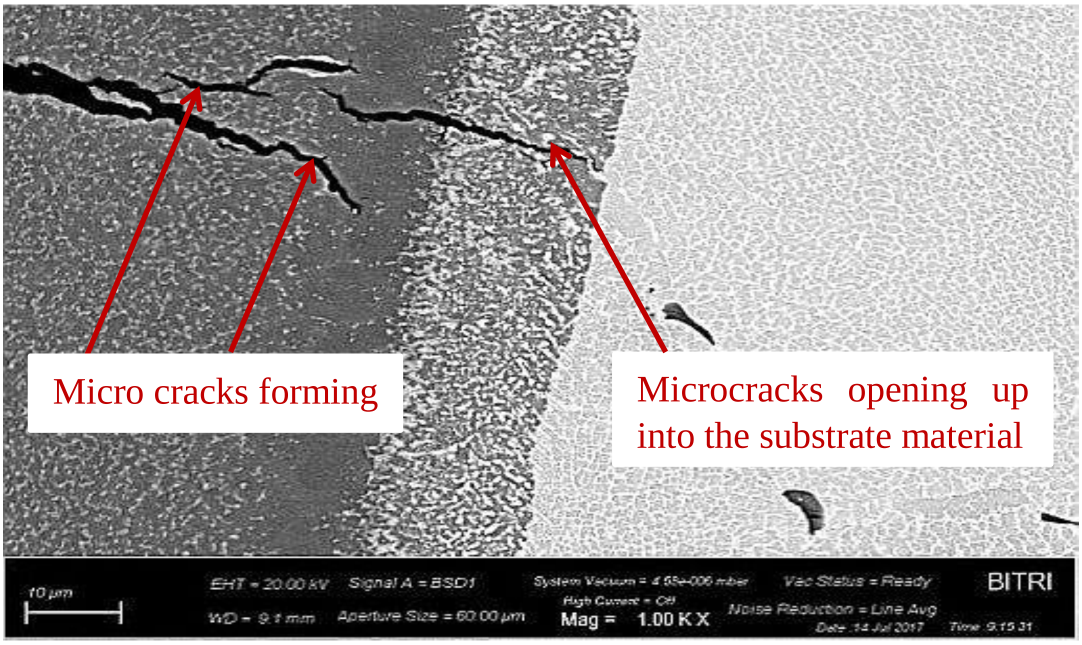

Figure 4. 27: Sectioned tip

Selected areas 1, 2, and 3 in the protective coating and illustrated in Fig. 4.28 and representing, outer, middle and inner protective coating layers were used for EDS analyses.

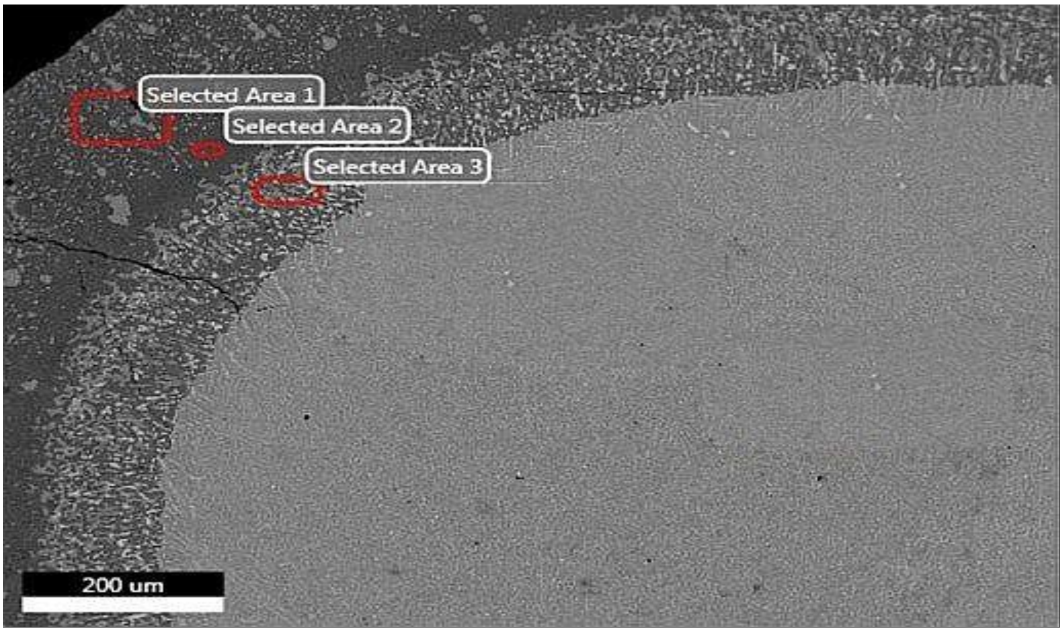

Figure 4. 28: EDS micrograph of sectioned tip

In reference to EDS spectra of the outer and middle layers of the protective coating in Figs. 4.29 and 4.30, no carbides nor oxides of any element were evident. Nonetheless, rich content of Al and Ni, an indication of active inward and outward diffusion for the two elements. There was also very rich presence of Si, Mo, Ti, Cr, and Co.

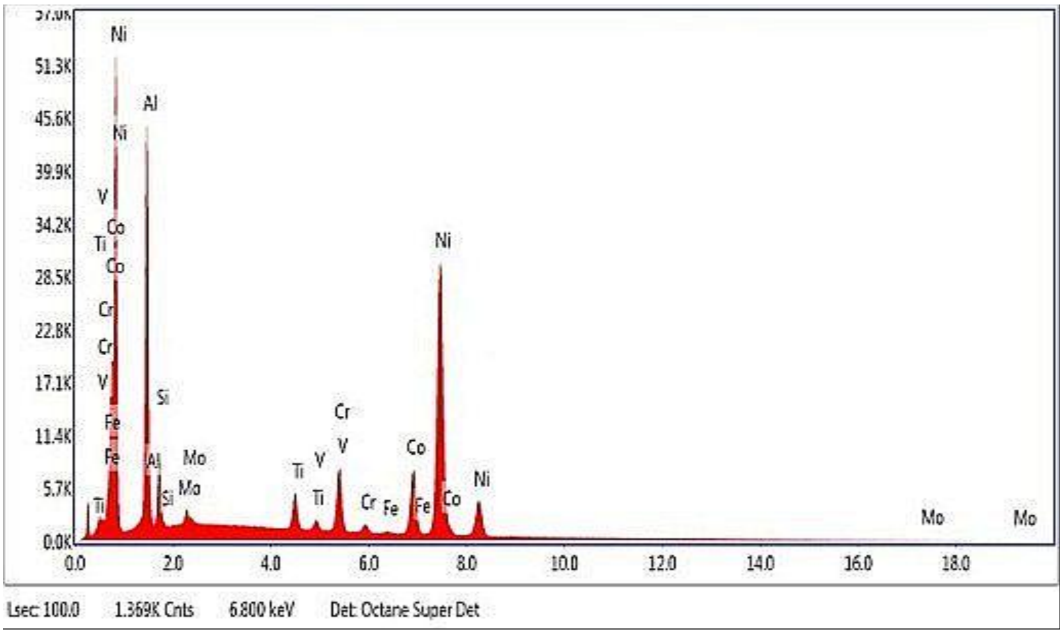

Figure 4. 29: EDS spectrum of selected area 1; the outer layer

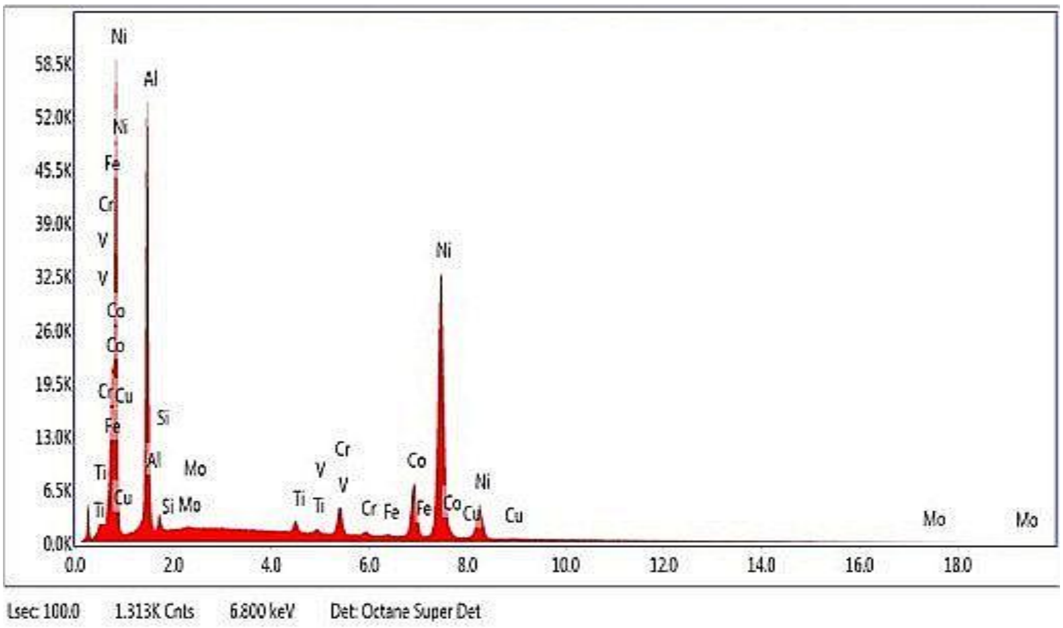

Figure 4. 30: EDS spectrum of selected area 2; the middle layer

The inner layer in Fig 4.31 was richer in Al and Ni but, indicated lesser of Si, Mo, Ti, V, Cr, Co, with introduction of Cu traces. The diffusion zone exhibited a decline in Al and Ni compared to the inner layer, an indication of lesser diffusion activity for both these elements in this zone. However, there was a rise in contents of Si, Mo, Ti, V, Cr and Co.

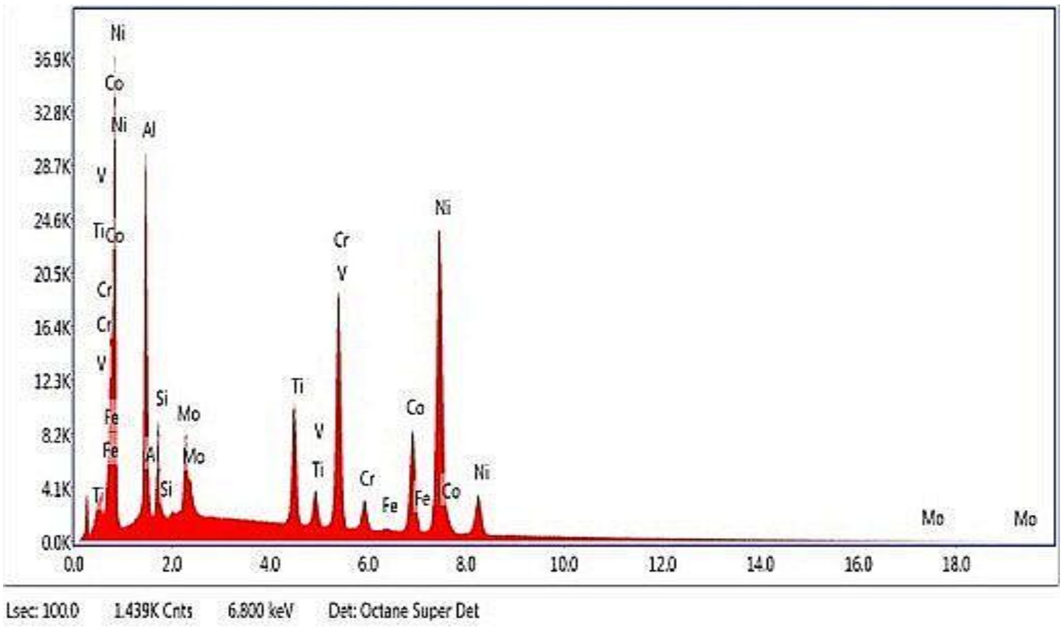

Figure 4. 31: EDS spectrum of selected area 3; the inner layer

Table 4.8 reports the EDS elemental composition of the sectioned tip on the outer, middle and inner layers of the protective coating in Figs 4.29 - 4.31.

Table 4. 8: Elemental composition of the tip at selected areas 1-3 in the coating

Element	**AlK**	**SiK**	**MoL**	**TiK**	**VK**	**CrK**	**FeK**	**CoK**	**NiK**	**CuK**
% Weight Selected Area1	20.9	3.8	1.5	2.8	0.6	5.8	0.3	10.7	56.3	-
% Weight Selected Area2	25.8	1.0	0.1	1.0	0.3	2.7	0.2	10.0	61.5	0.3
% Weight Selected Area3	13.1	3.3	5.4	6.3	1.4	16.1	0.3	12.3	44.3	-

4.5.2. The Airfoil

The sectioned airfoil revealed interdendritic white Mo rich MC carbides and gray Cr rich $M_{23}C_6$ primary blocky carbides as illustrated in Fig. 4.32.

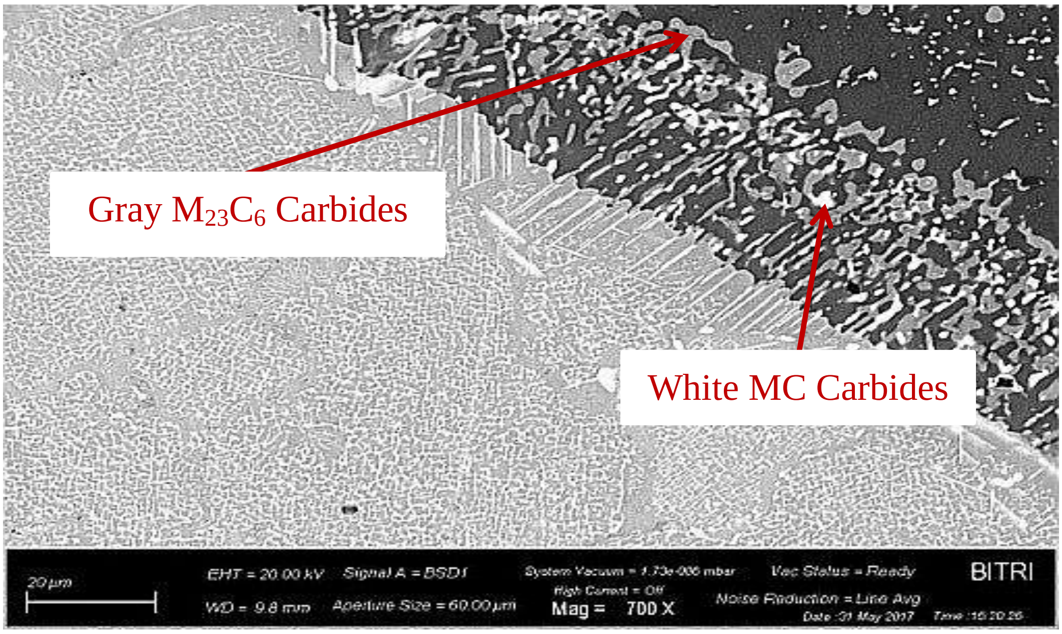

Figure 4. 32: Sectioned airfoil

The EDS cross section selected areas 1, 2 and 3 in the same diffusion zone represented by Figs. 4.33, 4.34, 4.35 and 4.36 indicated rich presence of Al, Si, Ti, V and Ni, all of which were in averagely the same range. In this region both outward Ni diffusion and inward Al diffusion was very active.

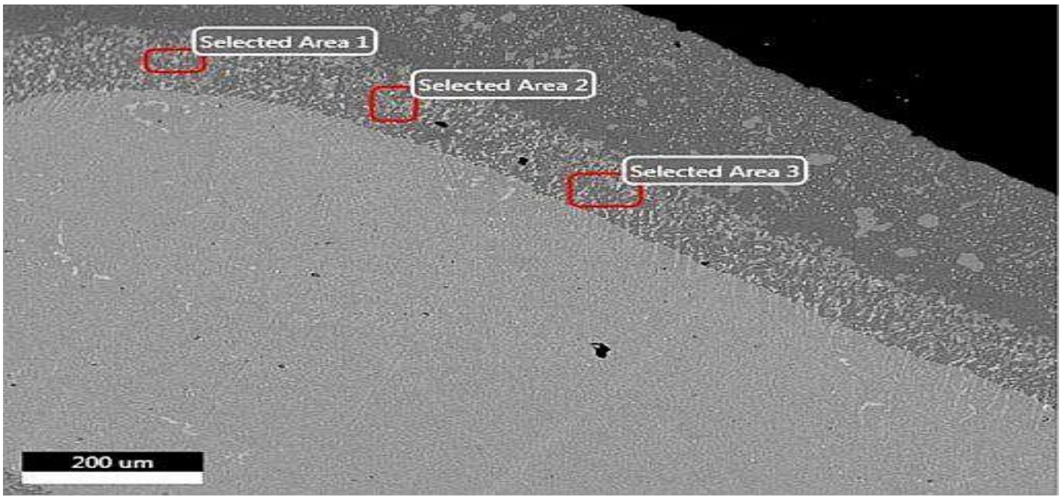

Figure 4. 33: EDS micrograph of sectioned airfoil

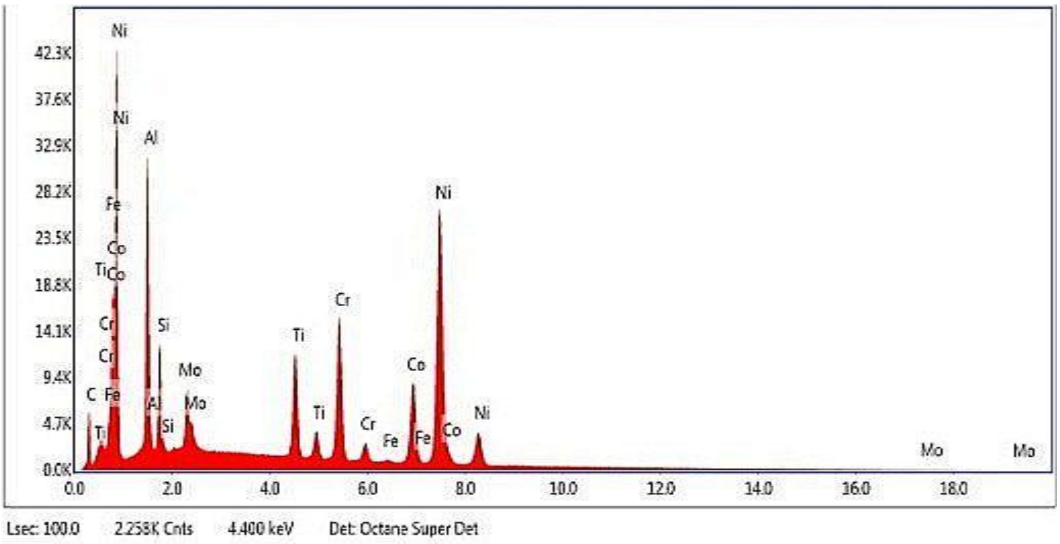

Figure 4. 34: EDS spectrum of selected area 1

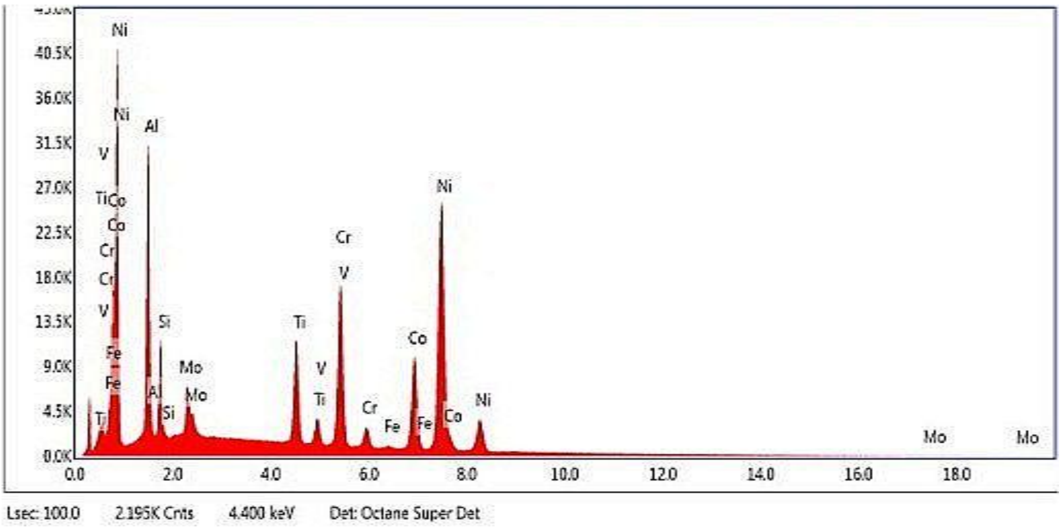

Figure 4. 35: EDS spectrum of selected area 2

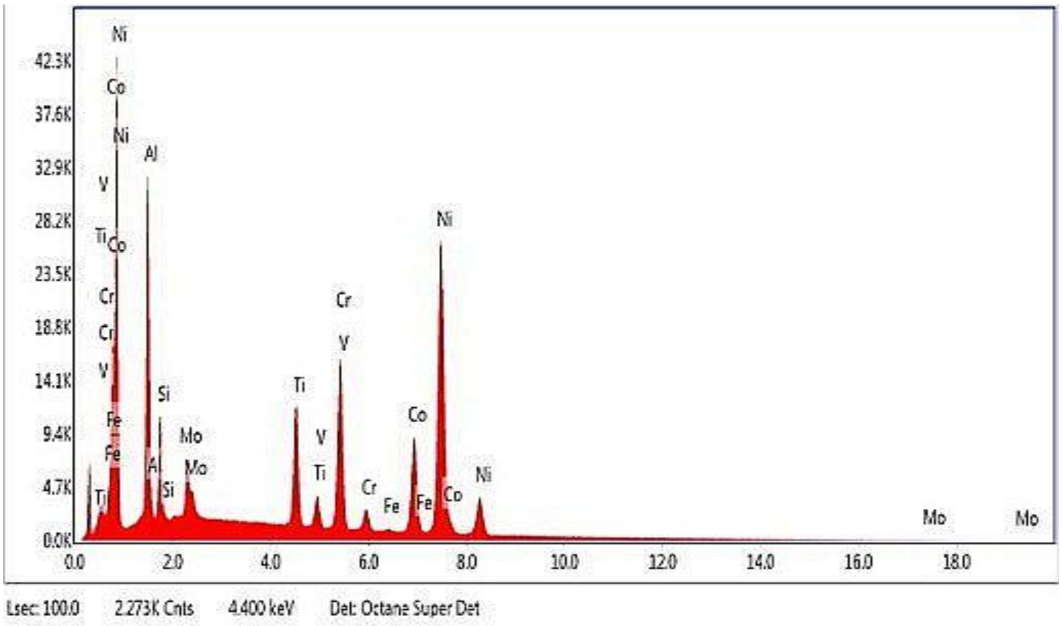

Figure 4. 36: EDS spectrum of selected area 3

Table 4.9 summarizes the EDS elemental composition of the airfoil at selected areas 1-3 in the diffusion zone in Figs. 4.34 – 4.36.

Table 4. 9: Elemental composition of the airfoil at selected areas 1-3; the diffusion zone

Element	**CK**	**AlK**	**SiK**	**MoL**	**TiK**	**VK**	**CrK**	**FeK**	**CoK**	**NiK**
% Weight Selected Area 1	13.1	10.8	3.8	4.3	5.9	0.8	10.5	0.1	10.5	41.1
% Weight Selected Area 2	12.8	13.0	4.1	4.3	6.7	0.9	13.2	0.1	13.4	44.4
% Weight Selected Area 3	12.6	13.1	3.9	4.5	6.9	1.1	12.3	0.3	12.3	45.6

The EDS spectra of the outer layer of the sectioned airfoil at selected areas 1, 2 and 3, illustrated in Figs. 4.37, 4.38, 4.39 and 4.40 revealed an increase in Al and Ni, an indication of active inward and outward diffusions of the two elements respectively compared to the tip. As a result, the airfoil was lesser attacked compared to the tip and more compared to the base. High content of Si, Mo, Ti, Cr, Co were similarly evident.

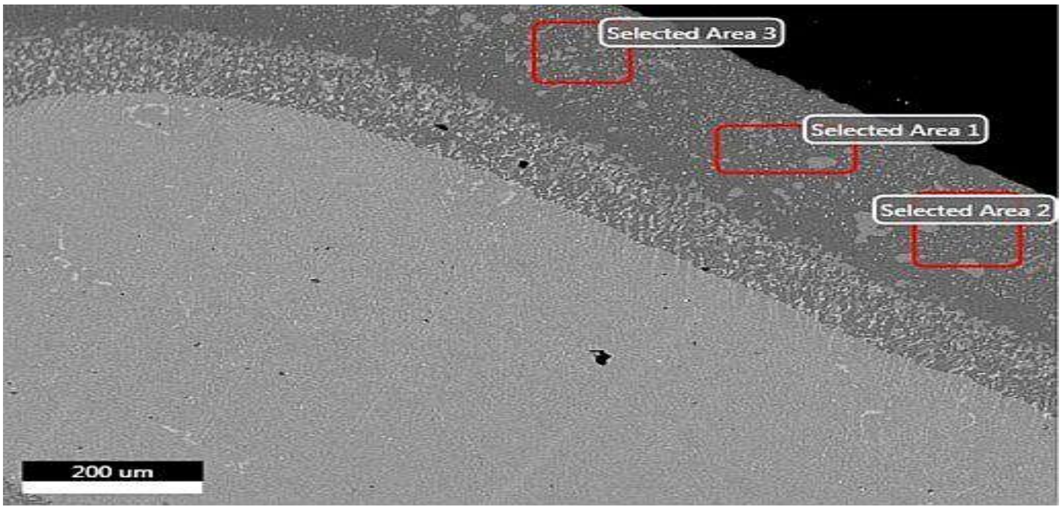

Figure 4. 37: Outer layer of the airfoil coating

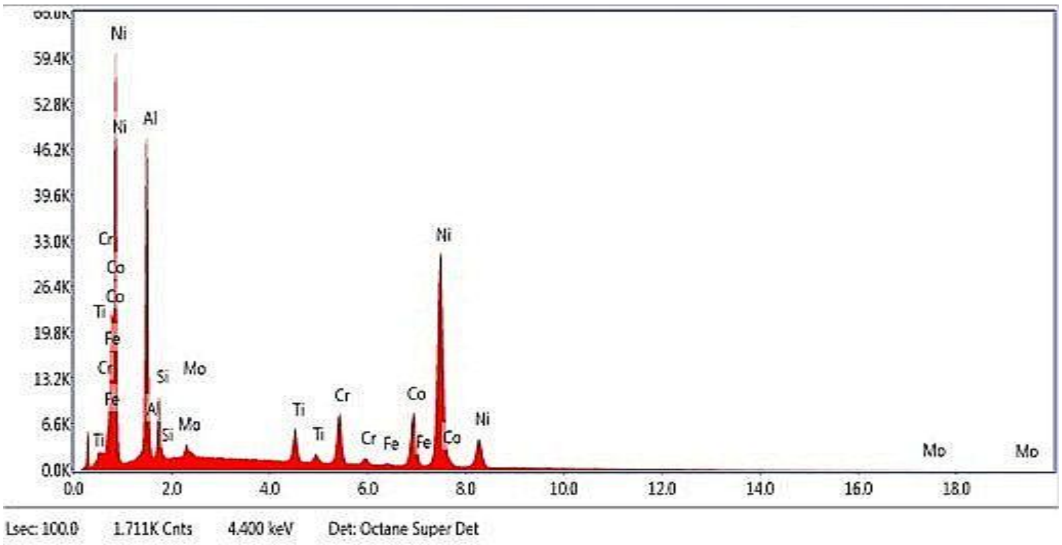

Figure 4. 38: EDS spectrum of selected area 1

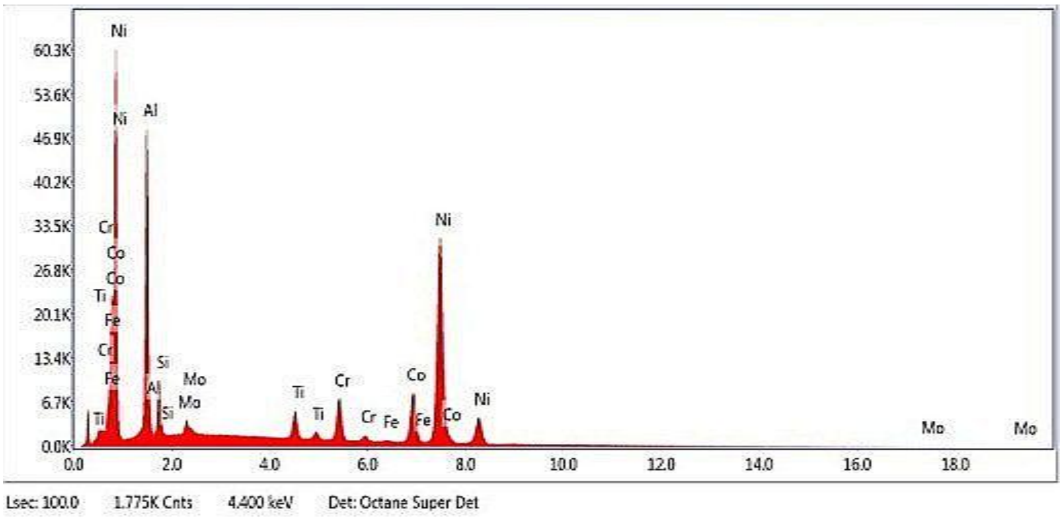

Figure 4. 39: EDS spectrum of selected area 2

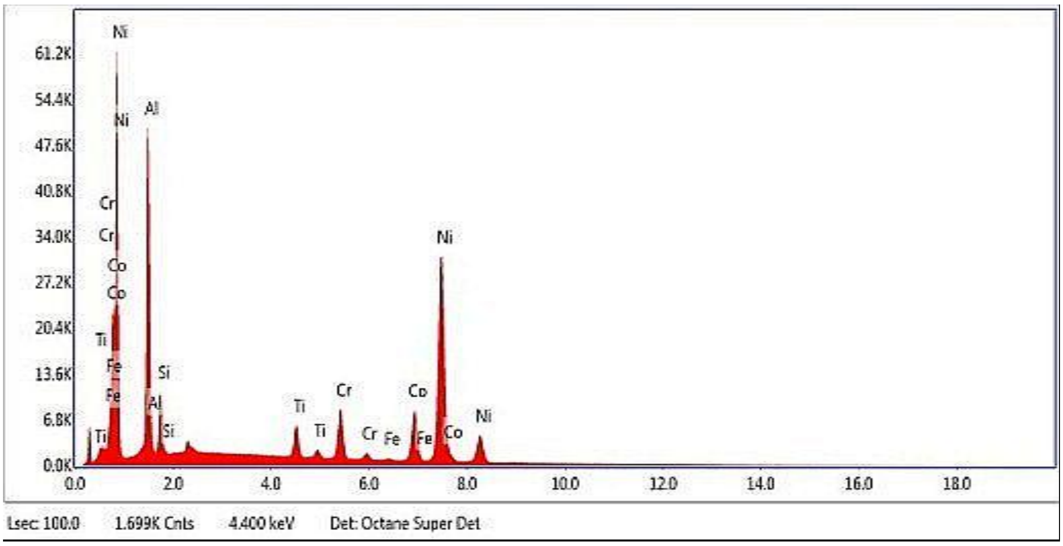

Figure 4. 40: EDS spectrum of selected area 3

Table 4.10 depicts the EDS elemental composition of the airfoil at selected areas 1-3; the outer layer in Figs. 4.38 – 4.40.

Table 4. 10: Elemental composition of the airfoil at selected areas 1-3; the outer layer

Element	**AlK**	**SiK**	**MoL**	**TiK**	**CrK**	**FeK**	**CoK**	**NiK**
% Weight Selected Area 1	20.2	4.3	1.8	3.1	5.7	0.4	10.7	53.9
% Weight Selected Area 2	20.9	3.9	1.9	2.6	4.8	0.1	10.5	55.3
% Weight Selected Area 3	21.3	4.5	2.0	3.1	5.9	0.3	10.5	54.4

4.5.3. The Base

The sectioned base had needles forming at the diffusion zones as expressed in Fig. 4.41, with formation of M_6C eutectic carbides from solubility of Mo at low temperatures.

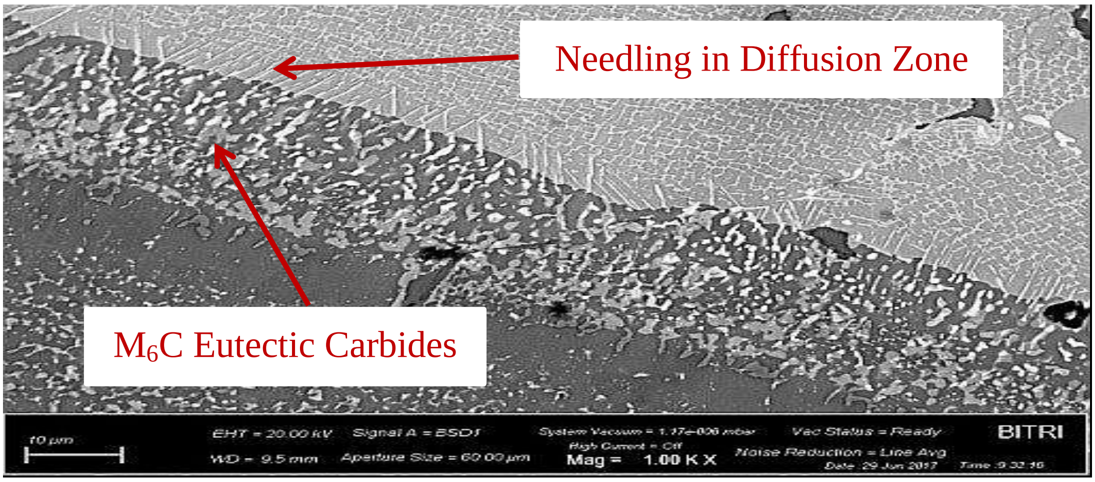

Figure 4. 41: Sectioned base

Selected EDS spots 1, 2 and 3 in Fig 4.42 were used for analyses. EDS spot 1 in Fig. 4.43, indicated pronounced presence of Mo, Ti, V and Co. Little outward diffusion of Ni was noted with no inward diffusion of Al. Traces of oxides of Si were also present.

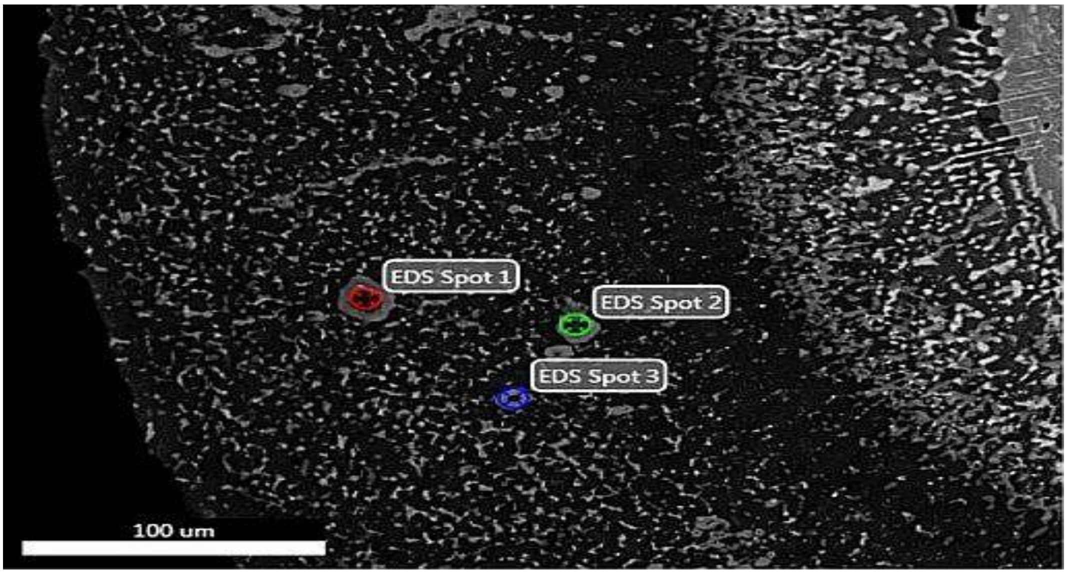

Figure 4. 42: EDS micrograph of the sectioned base

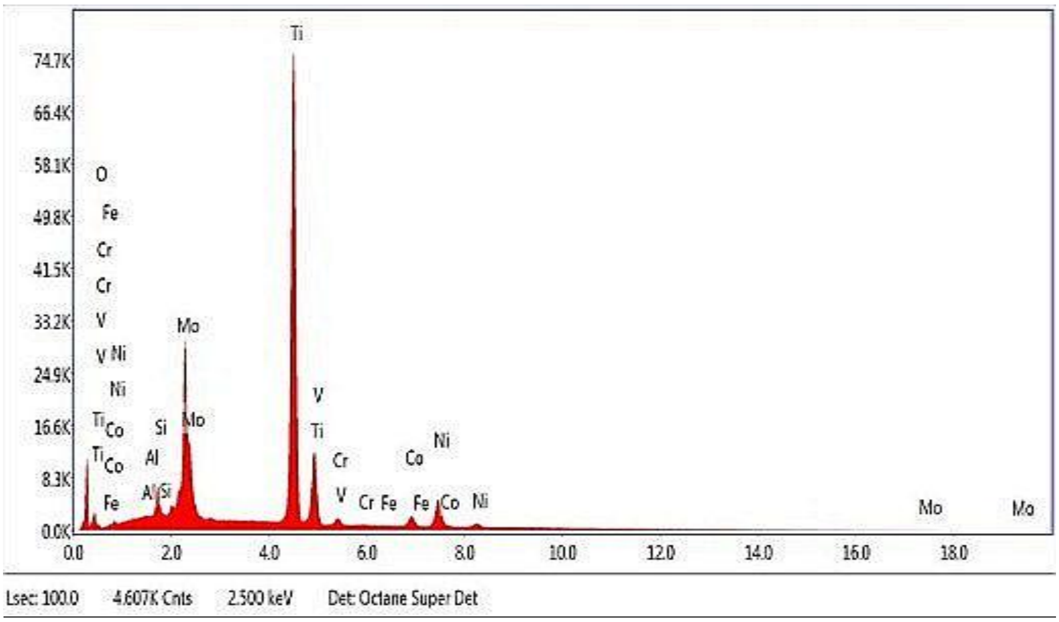

Figure 4. 43: EDS spectrum of spot 1

EDS spot 2, in Fig. 4.44 recorded much higher levels of Mo, Ti. V, Cr and Co however dwindled. Escalating levels of Si was evident. Outward Ni diffusion fell by approximately 50% relative to EDS spot 1.

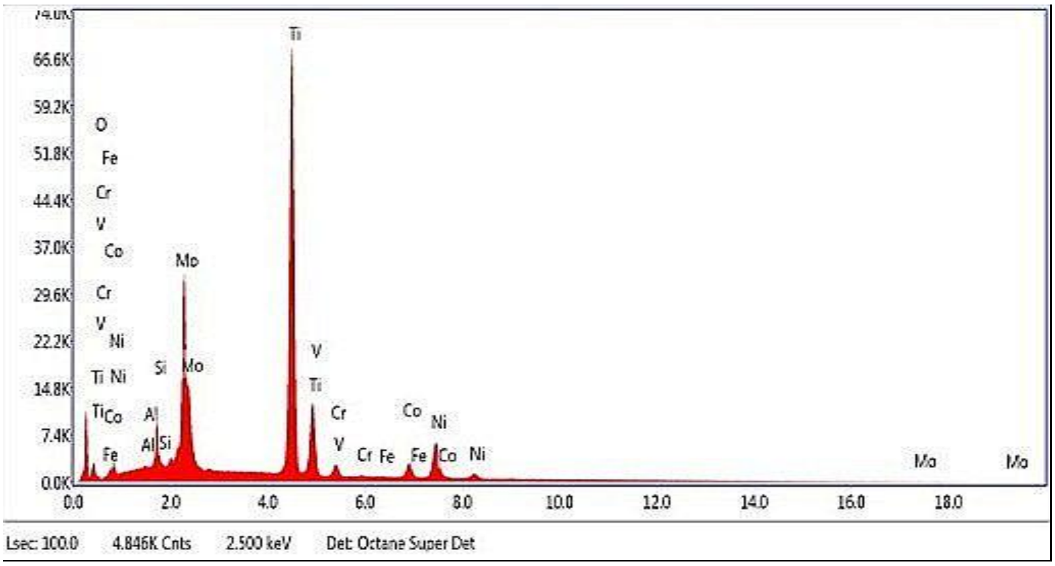

Figure 4. 44: EDS spectrum of spot 2

For EDS spot 3 denoted in Fig. 4.45, high contents of oxides of Si, Mo, Ti, maintained as well as much active outward diffusion of Ni in comparison to EDS spot 2.

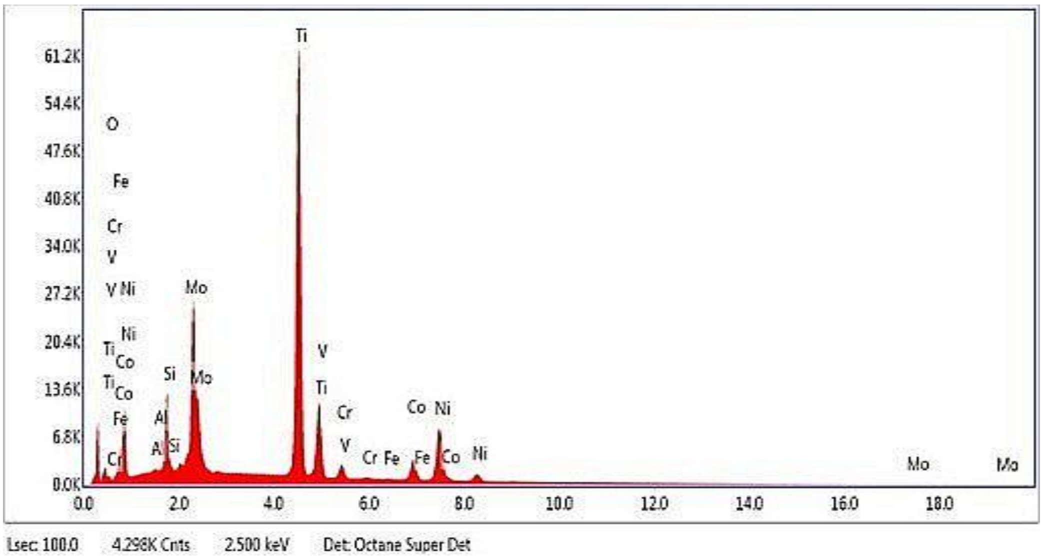

Figure 4. 45: EDS spectrum of spot 3

Table 4.11 summarizes the EDS elemental composition of the base at selected spots 1–3, in Figs 4.43 – 4.45.

Table 4. 11: Elemental composition of the base at EDS spots 1-3

Element	**OK**	**AlK**	**SiK**	**MoL**	**TiK**	**VK**	**CrK**	**FeK**	**CoK**	**NiK**
% Weight EDS Spot 1	0.9	0.0	1.7	23.3	59.5	2.2	1.0	0.1	2.8	8.7
% Weight EDS Spot 2	0.1	0.0	2.5	27.7	61.5	2.0	0.7	0.0	0.6	3.9
% Weight EDS Spot 3	2.0	0.0	4.2	24.1	60.5	2.0	0.8	0.0	0.8	5.6

4.6. Results and discussions of substrate material

4.6.1. X-Ray Flouresent analyses

The XRF results captured the bulk constituent elements for both the protective coating as well as the substrate material of the CT blades and are similar to those reported earlier in section 4.4.1.

4.6.2. X-Ray Diffraction analyses

Fig. 4.46 reports on the XRD spectrum on which seven peaks and their relative positions were identified and recorded in Table 4.12.

Table 4. 12: XRD identified peaks, their positions and respective counts

Peak Number	**1**	**2**	**3**	**4**	**5**	**6**	**7**
Position [°2θ]	35.64	36.29	43.94	50.75	63.32	74.98	91.08
Height (Counts)	392.04	392.04	15725.16	2693.61	129.96	2981.16	2043.04

Two compounds predominantly formed the bulk of the peaks; a Chromium Nickel, bearing a reference code of 98-018-8248, with a chemical formula of Cr_3Ni_1. Peaks 1, 3, 4 and 6 matched it. The second is Molybdenum Carbide compound with a reference code 98-061-8301, and a chemical formula of C_1Mo_1, with peaks 2 and 6 positively identifying with it. The constituent elements of these compounds form the bulk of the base and alloying materials in Inconel 713LC.

One other peak number 7 in the XRD pattern could not match any PAN ICSD Database FIZ Karlsruhe 2016-1 for High Score (Plus) V3. X. In this case it was omitted in the analyses. This could have been occasioned by the scanned surfaces of the samples being smaller than 5mm holder space, resulting in low intensity peaks which were also very close to the background noise making it difficult to be tapped despite scanning having lasted for over one hour of scan time per sample.

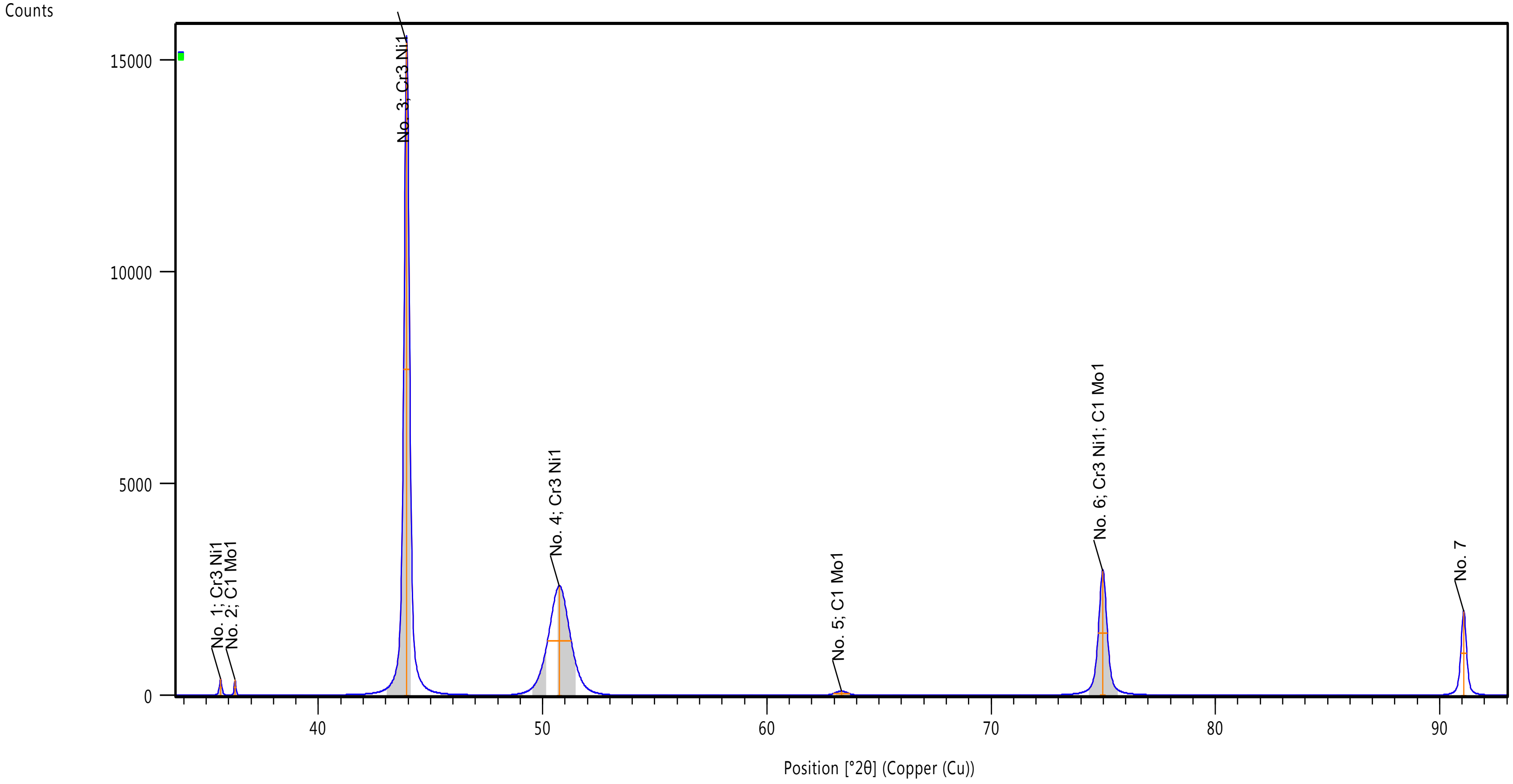

Figure 4. 46: XRD Analysis

4.6.3. Energy Dispersive Spectroscopy-Scanning Electron Microscopy analyses

4.6.3.1. The Tip

The tip section had cracks originating from the protective coating and finding their way to the substrate material. Pores were evident and needles had developed as they appear in Fig. 4.47.

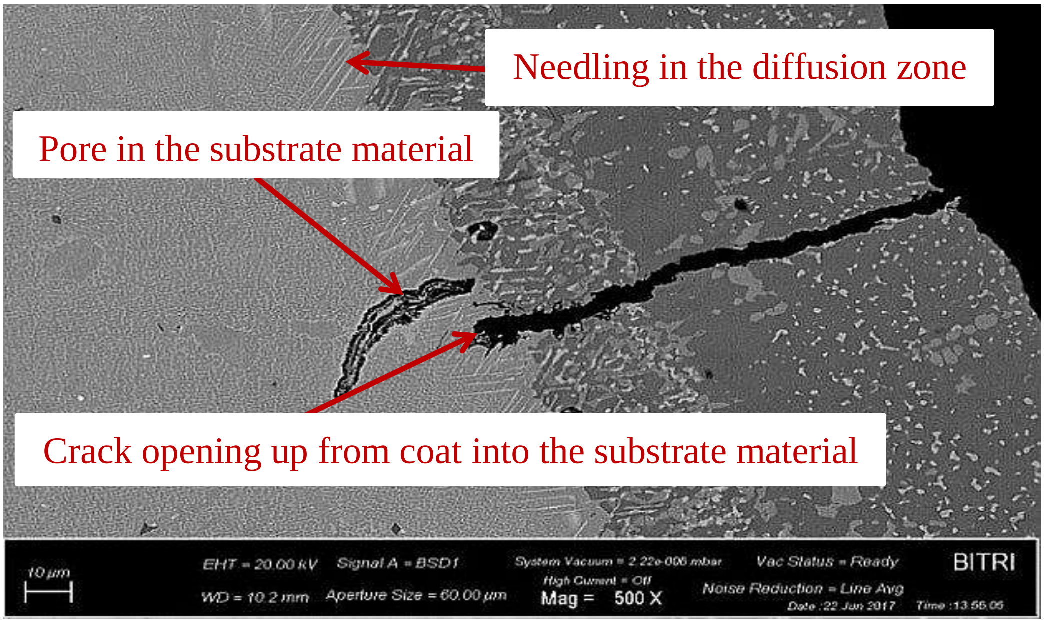

Figure 4. 47: Sectioned tip

Selected areas 4, 5 and 6 as shown in Fig. 4.48 were chosen for EDS analyses.

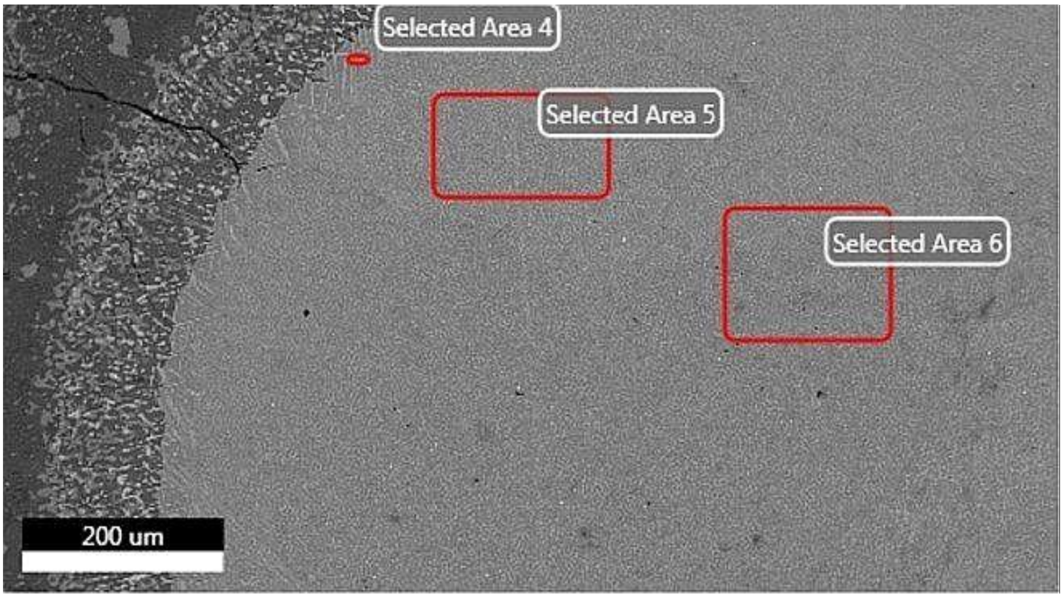

Figure 4. 48: EDS micrograph of sectioned tip

The EDS spectra of selected areas 4, in Fig. 4.49 had a great inward diffusion of Al than outward diffusion of Ni. It also equally had trace oxides of Si, Fe, and Cu, possibly from the fuel constituents and flight environment. Carbides of Mo, Ti, V, Cr and Co were present.

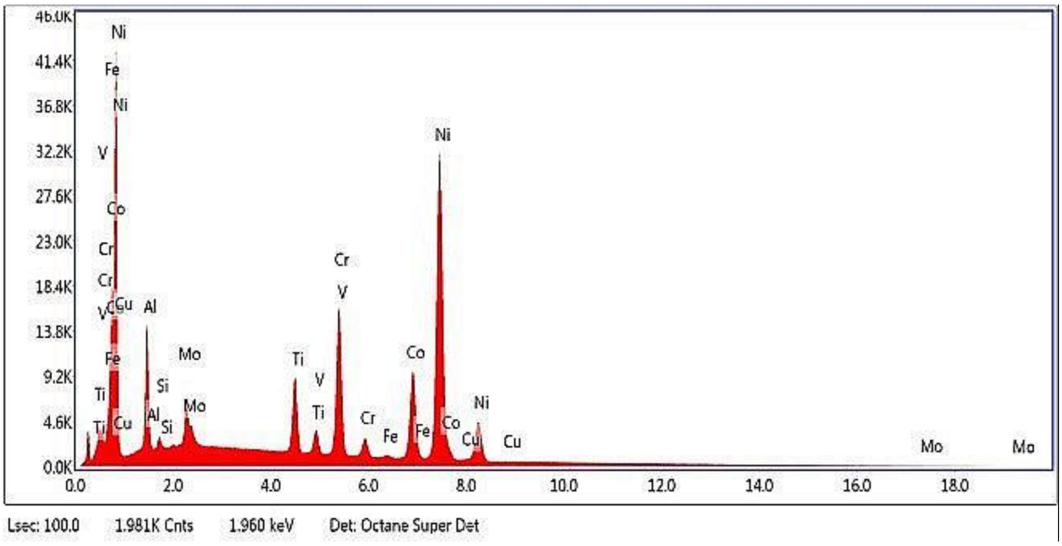

Figure 4. 49: EDS spectrum of selected area 4

Spectra for selected areas 5 and 6 in Figs. 4.50 and 4.51 had more or less similar characteristics; decreased Al inward diffusion and increased outward Ni diffusion. No traces of oxides from Si, Fe and Cu were found. The two areas equally exhibited a drop-in carbide of Mo and Cr, relative to selected area 4, but an increase in carbides of Co. V decreased in selected area 5 compared to 4 and was absolutely nonexistent in selected area 6.

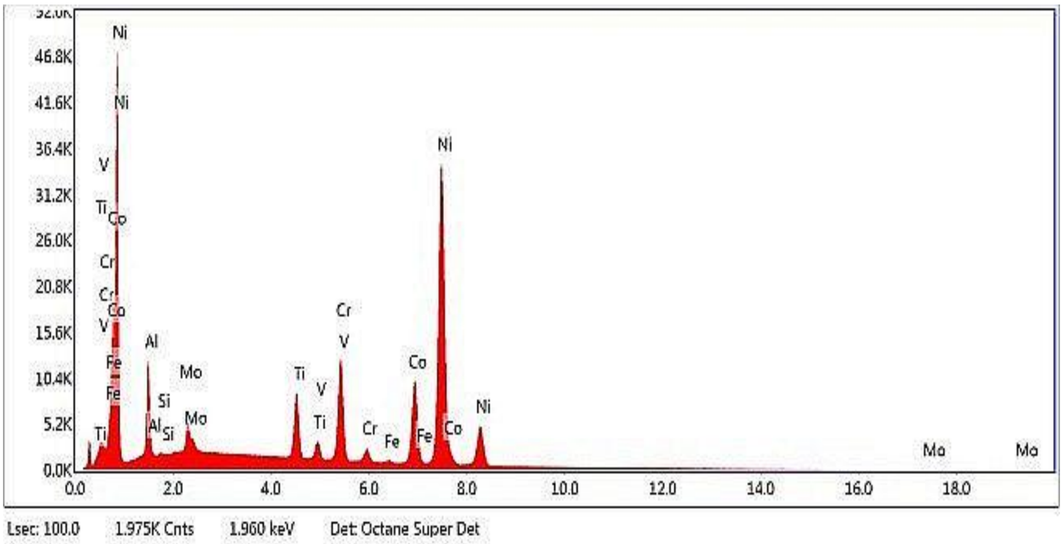

Figure 4. 50: EDS spectrum of selected area 5

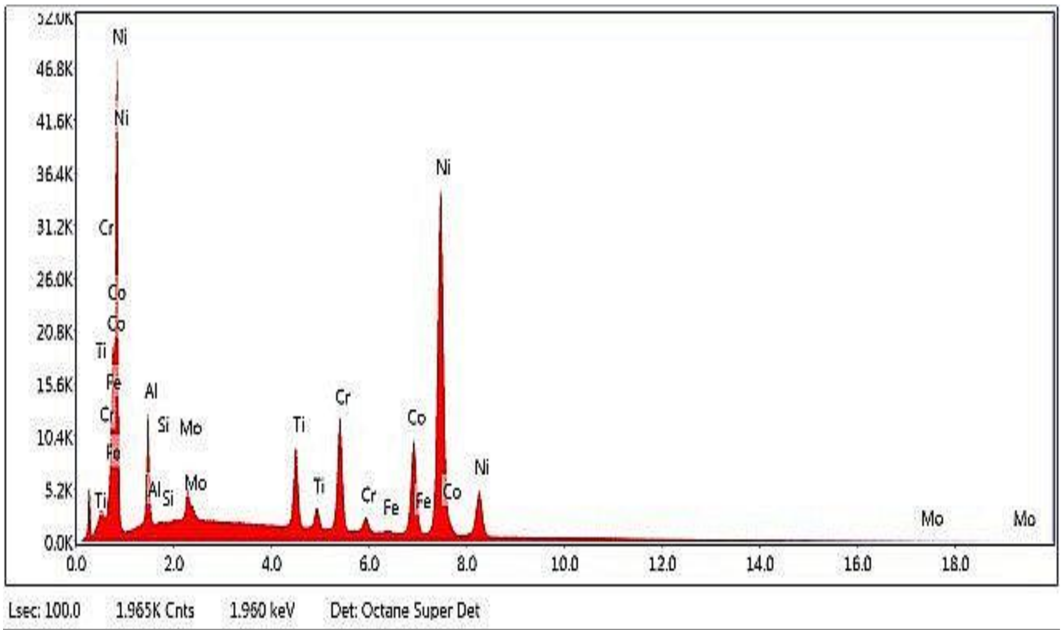

Figure 4. 51: EDS spectrum of selected area 6

Table 4.13 records the EDS elemental composition of the tip at selected areas 4 – 6 in Figs. 4.49 – 4.51.

Table 4. 13: Elemental composition of the tip at selected areas 4-6

Element	**AlK**	**SiK**	**MoL**	**TiK**	**VK**	**CrK**	**FeK**	**CoK**	**NiK**	**CuK**
% Weight Selected Area 4	6.4	0.4	3.0	4.6	1.2	12.3	0.4	13.8	57.8	0.3
% Weight Selected Area 5	5.4	0.0	2.2	4.4	0.9	9.3	0.3	14.5	62.9	-
% Weight Selected Area 6	5.6	0.0	2.2	4.7	-	9.1	0.3	14.2	63.8	-

For the tips which are the hottest regions of the CT blade indicated considerable magnitude of deterioration of microstructure. Primary original metal carbides near evenly perfect cuboidal phase of MC had degenerated and transformed into $M_{23}C_6$, M_6C and M_7C_3. As a result, rafting and elongation of the later carbides led weakening the material structure and upon cooling, cracking was ultimately inevitable. Such attacks were prominent at the leading edges of the blades than the trailing edges, airfoils, and base regions as confirmed by the temperature modeling results.

4.6.3.2. The Airfoil

The micrograph in Fig. 4.52 presents evidence of pores with dispersions of white Ti MC carbides.

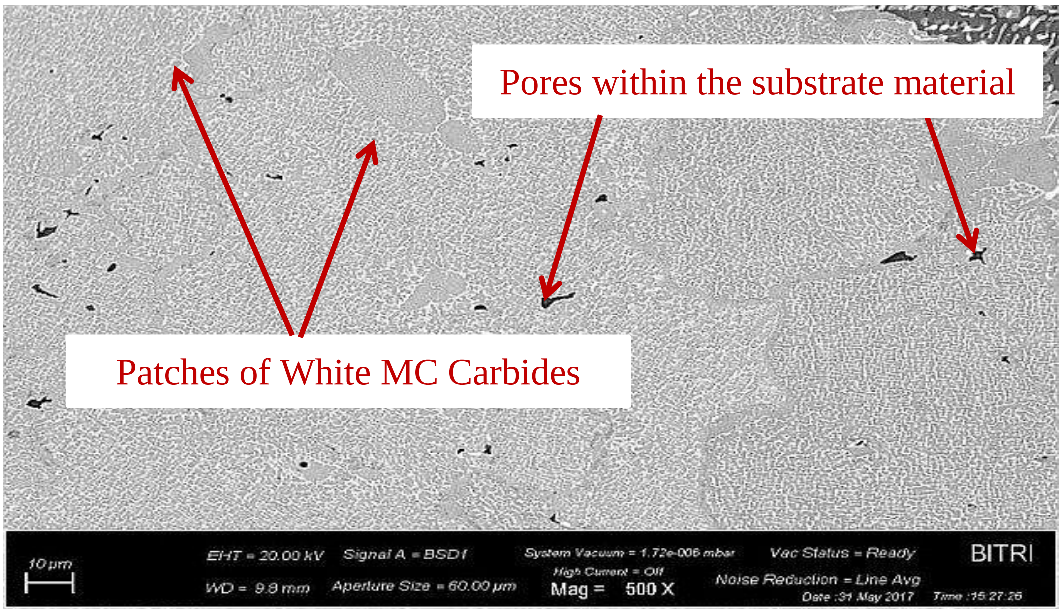

Figure 4. 52: Sectioned airfoil (Image 1)

Grains had also developed gray $M_{23}C_6$ carbides, as depicted in Fig. 4.53 arising from decomposing of MC carbides after repetitive exposure to elevated temperatures. As a result, rafting was evident but, at a much lower level compared to the tip.

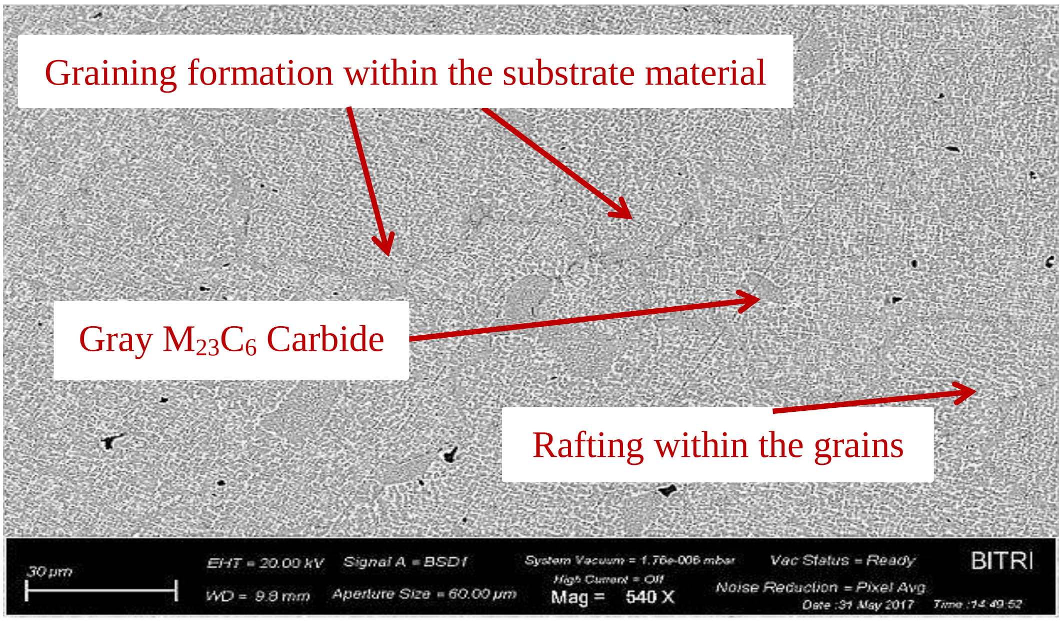

Figure 4. 53: Sectioned airfoil (Image 2)

The EDS spectra of the airfoil in Figs. 4.54, 4.55, 4.56 and 4.57 indicated a more uniform degradation of the material compared to the tip. For the same selected areas, carbides of Mo, Ti, Cr and Co were averagely similar too, with traces of Fe also detected in relatively equal measures. Inward Al diffusion besides outward Ni diffusion concurrently occurred.

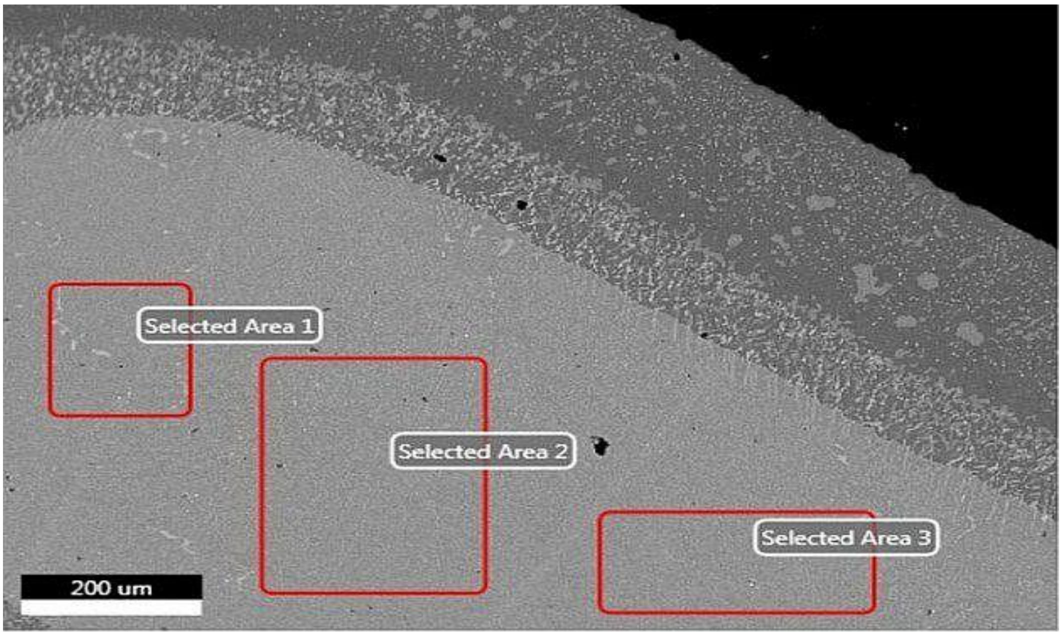

Figure 4. 54: EDS micrograph of sectioned airfoil

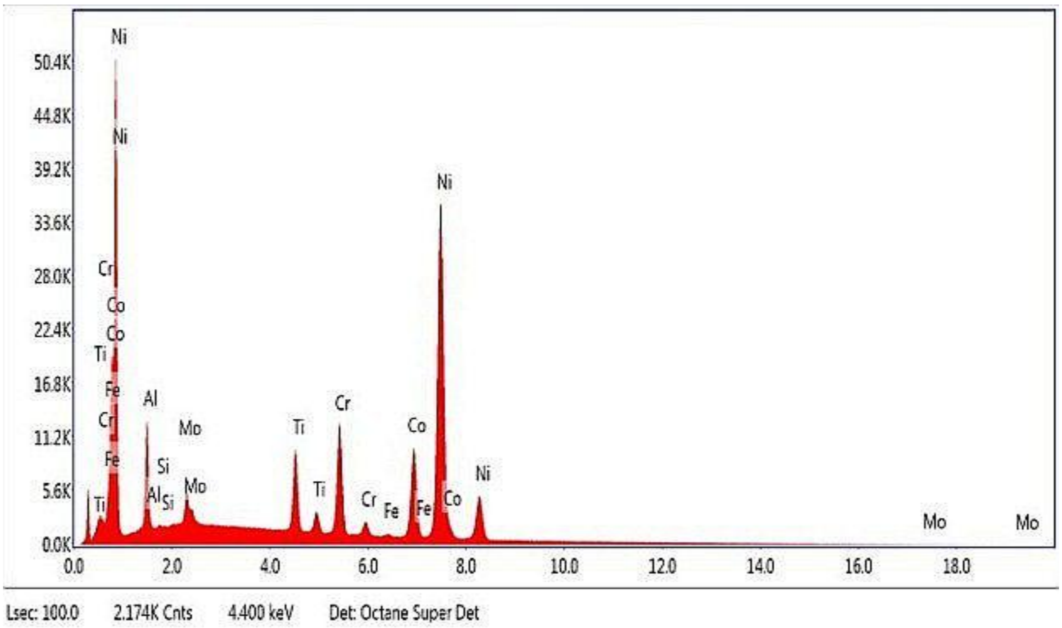

Figure 4. 55: EDS spectrum of selected area 1

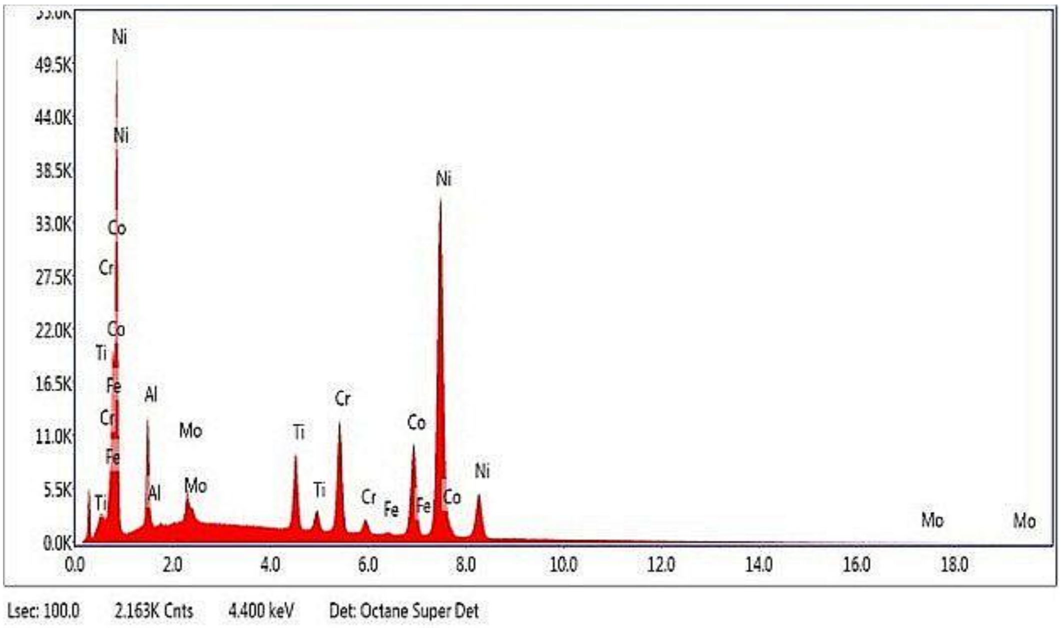

Figure 4. 56: EDS spectrum of selected area 2

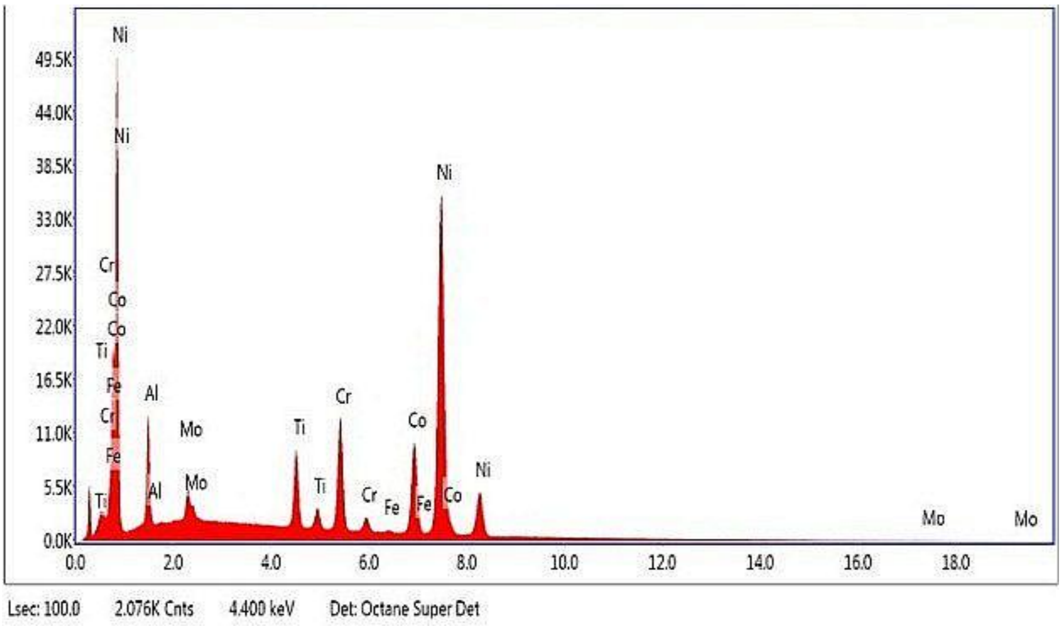

Figure 4. 57: EDS spectrum of selected area 3

Table 4.14 indicates the elemental composition of the airfoil at selected areas 1-3 in Figs. 4.55 – 4.57.

Table 4. 14: Elemental composition of airfoil at selected areas 1-3

Element	AlK	MoL	TiK	CrK	FeK	CoK	NiK
% Weight Selected Area 1	5.6	2.9	5.4	9.1	0.2	13.5	63.2
% Weight Selected Area 2	5.7	2.8	5.0	9.1	0.1	13.7	63.6
% Weight Selected Area 3	5.6	2.8	5.1	9.3	0.3	13.7	63.1

The inner material within the depletion zone of the airfoil in Fig. 4.58 experienced pronounced rafting.

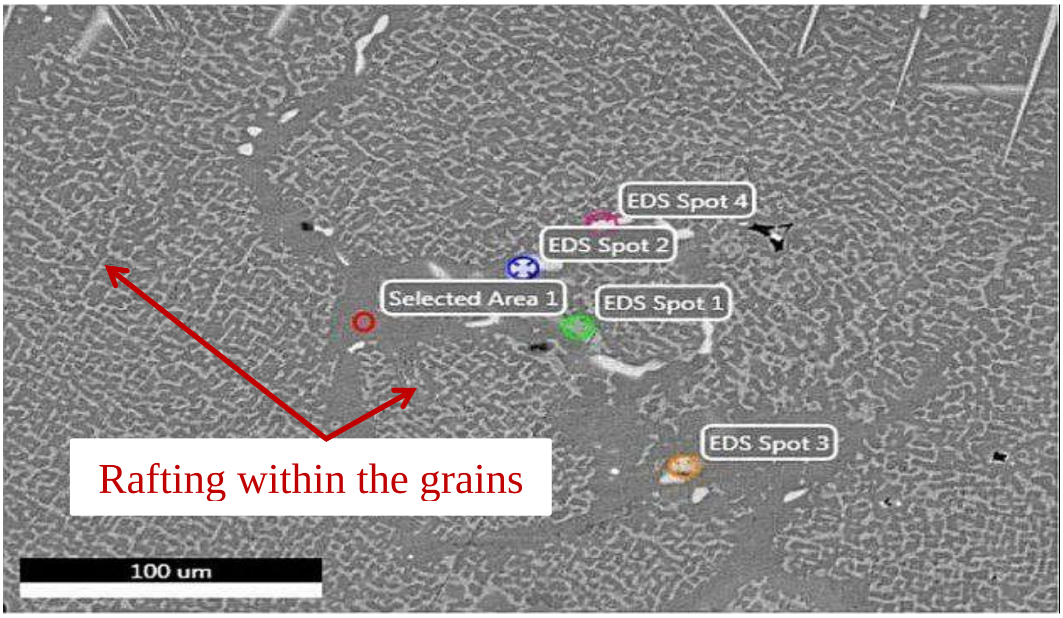

Figure 4. 58: Sectioned airfoil inner material within the depletion zone

Selected area 1, in Fig. 4.59 confirmed both active Al inward and outward Ni diffusions. Carbides of Mo, Cr, Co dropped, while Ti carbides significantly increased. Occurrence of V was also occasioned.

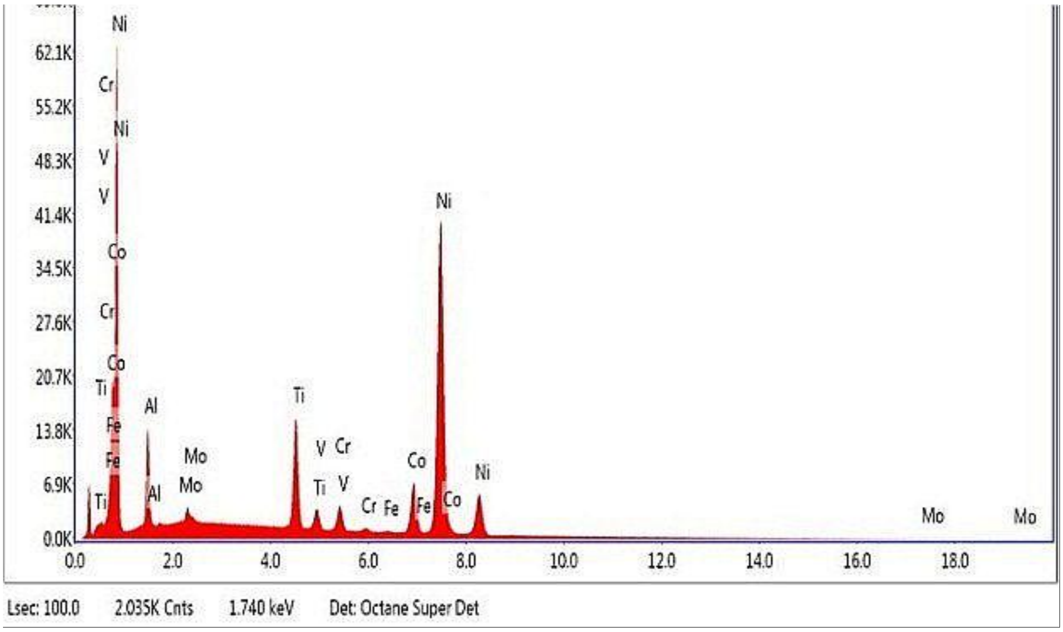

Figure 4. 59: EDS spectrum of selected area 1

EDS spots 1 in Fig. 4.60 depicted a significant increase in $M_{23}C_6$ carbides of Cr and Co. Carbides of Mo and V had slightly increased while Ti carbides had dropped. Traces of Si were identified with inactivity of both inward Al and outward Ni diffusion recorded.

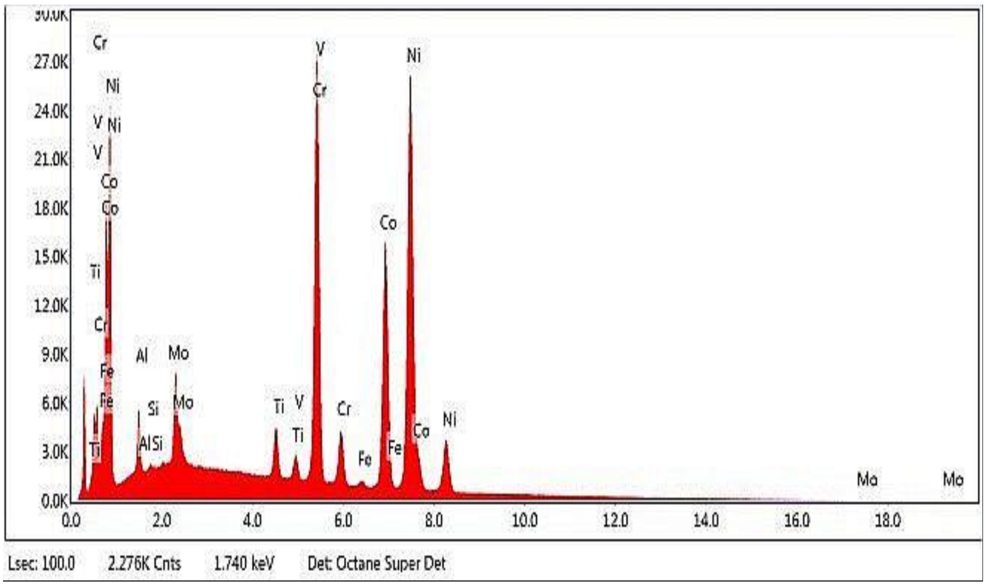

Figure 4. 60: EDS spectrum of spot 1

EDS spot 2 adjacent to MC carbides of Mo and Cr in Fig. 4.61 indicated slight increase in carbides of Ti. Co carbides dropped while V completely disappeared. Significant fall in activity of both inward Al and outward Ni diffusion was noted as Si and Fe presence remained unaltered.

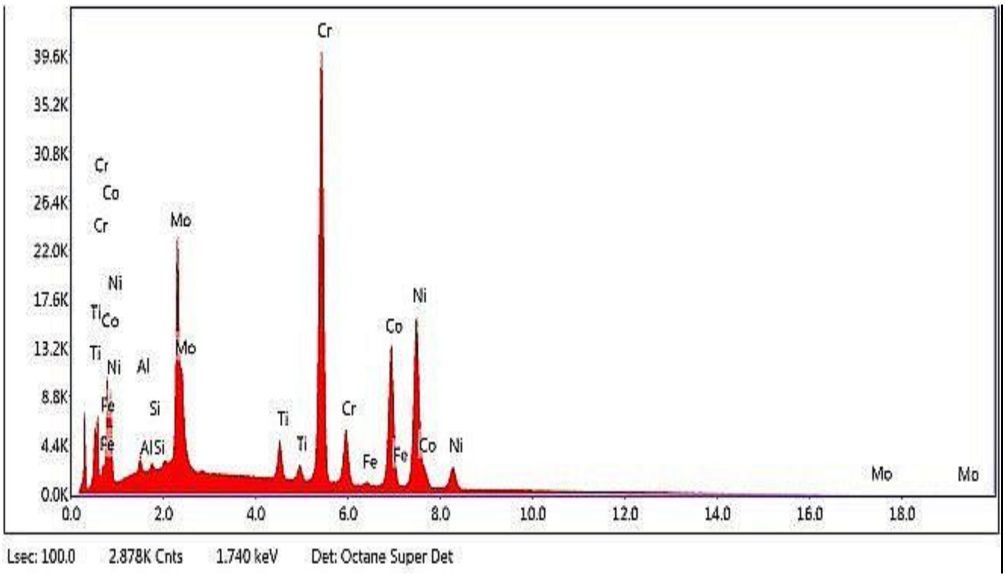

Figure 4. 61: EDS spectrum of spot 2

EDS spot 3 in Fig. 4.63 affirmed occurrence of white MC carbides of Cr with a slight drop of diffusion activity for both Al and Ni. Si had also significantly risen.

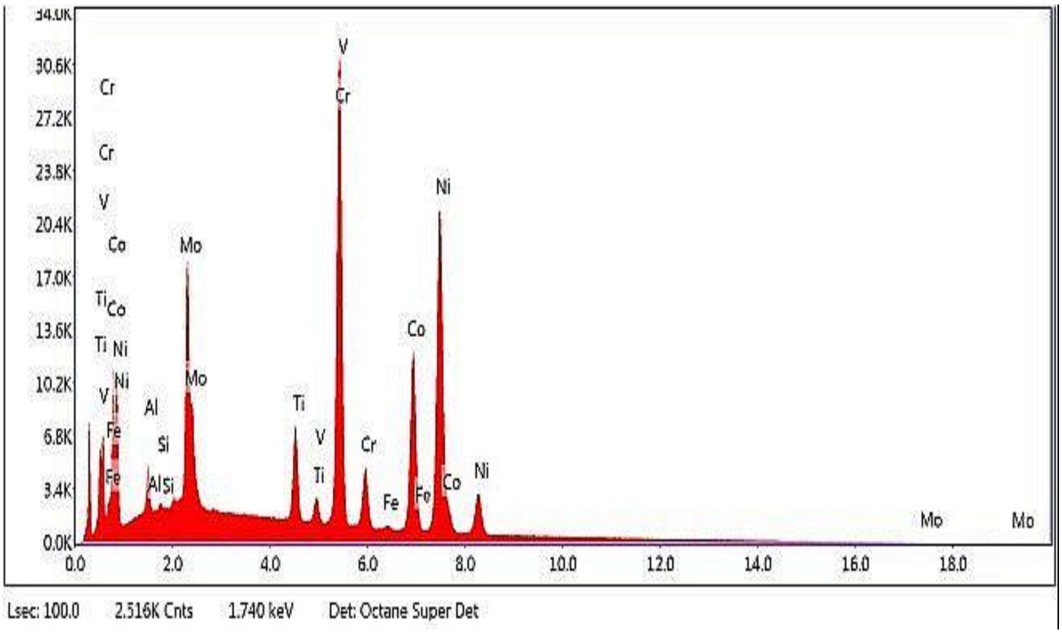

Figure 4. 62: EDS spectrum of spot 3

EDS spot 4 in Fig. 4.63 recorded an increase in carbides of Mo, Ti and Cr, while $M_{23}C_6$ carbides of Co dropped. There was a fall in V and Fe. Relative to EDS spot 2, Al activity had slightly increased, while Ni activity significantly dropped.

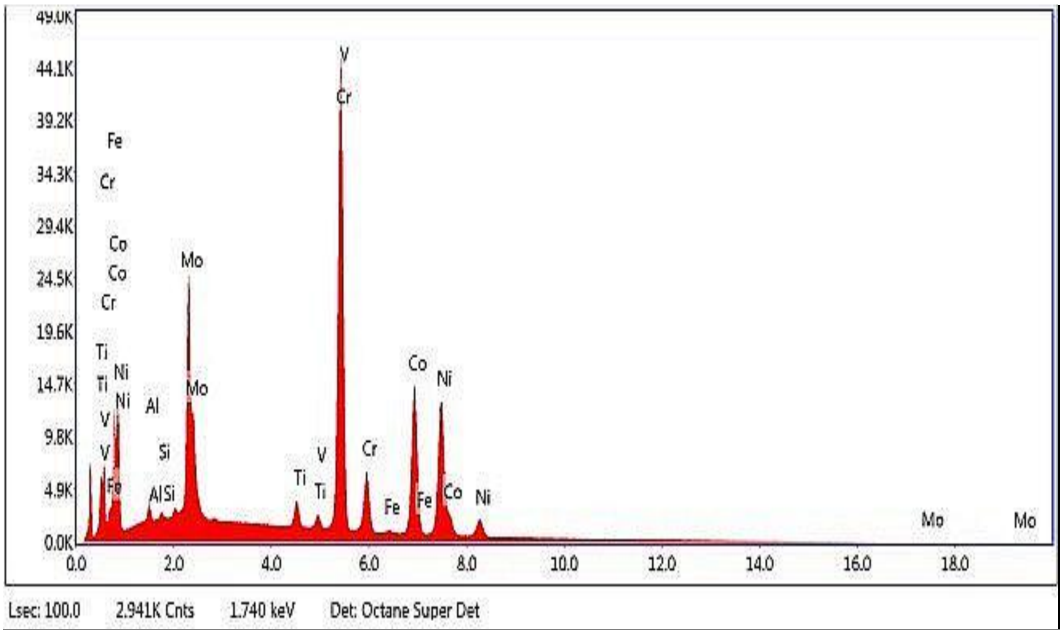

Figure 4. 63: EDS spectrum of spot 4

Table 4.15 denotes the EDS elemental composition of the airfoil's inner material within the depletion zone for selected area 1 and EDS spots 1-4, in Figs. 4.59 – 4.63.

Table 4. 15: Elemental composition of airfoil at selected areas 1-4; the depletion zone

Element	**AlK**	**SiK**	**MoL**	**TiK**	**VK**	**CrK**	**FeK**	**CoK**	**NiK**
% Weight Selected Area 1	6.2	-	1.5	9.0	0.6	2.4	0.2	9.1	70.9
% Weight EDS Spot 1	1.9	0.1	4.7	1.9	0.9	21.4	0.5	22.7	45.9
% Weight EDS Spot 2	0.6	0.1	15.8	2.3	-	33.7	0.4	19.5	27.6
% Weight EDS Spot 3	1.5	0.6	12.3	4.0	0.7	26.1	0.3	17.4	37.5
% Weight EDS Spot 4	0.7	0.2	16.4	1.6	0.8	37.2	0.5	20.7	22.1

4.6.3.3 The Base

Pores which are manufacturing defects were identified at the base as shown in Fig. 4.64. However, contrary to presence of pores being thought to create potential weak points within the material, the base seemingly had a nearer uniform distribution of cuboidal phase as likened to the tip and airfoil. M_6C eutectic carbides were also noticed occasioned by slow heating up in this region, resulting in much longer heat retention. As such, upon cooling, gradual precipitation was inevitable. Dispersions of white MC carbides of Cr at the grain boundaries were similarly evident from incomplete solutioning of the material as it ages.

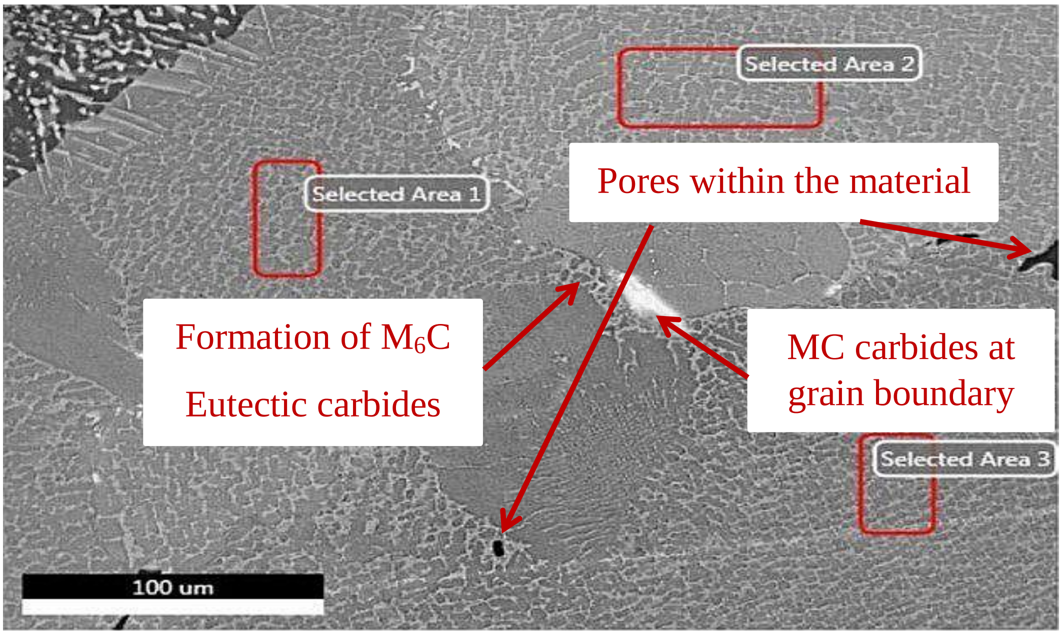

Figure 4. 64: Sectioned base

Carbides of Mo, V and Cr, were averagely uniformly distributed. A fairly similar inward Al as well as outward Ni diffusions was noted at the selected areas 1-3 at the base represented in Figs. 4.65, 4.66 and 4.67.

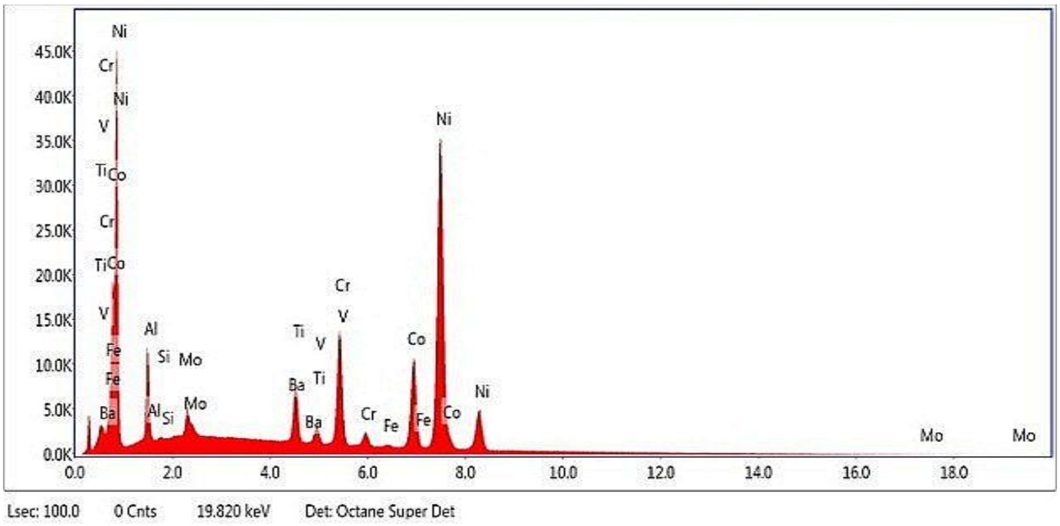

Figure 4. 65: EDS spectrum of selected area 1

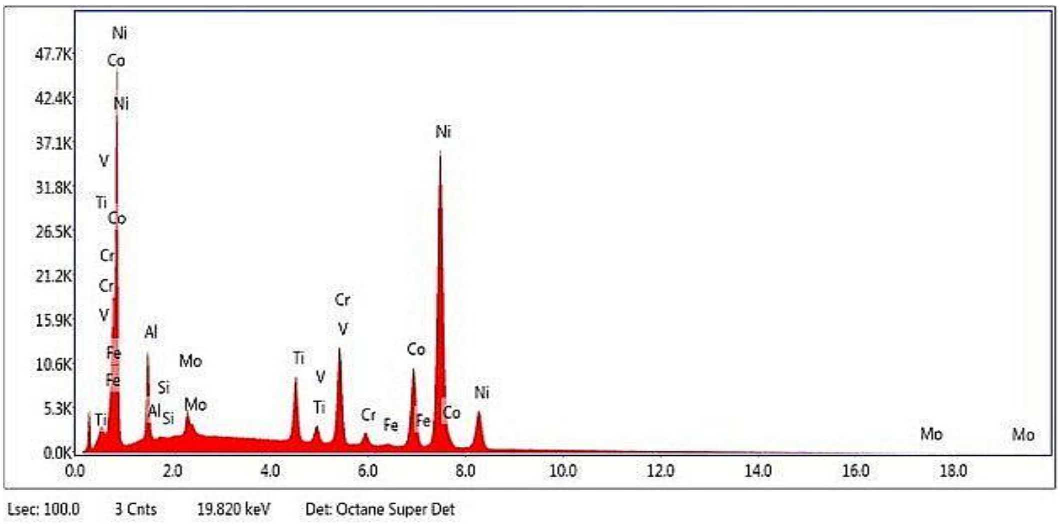

Figure 4. 66: EDS spectrum of selected area 2

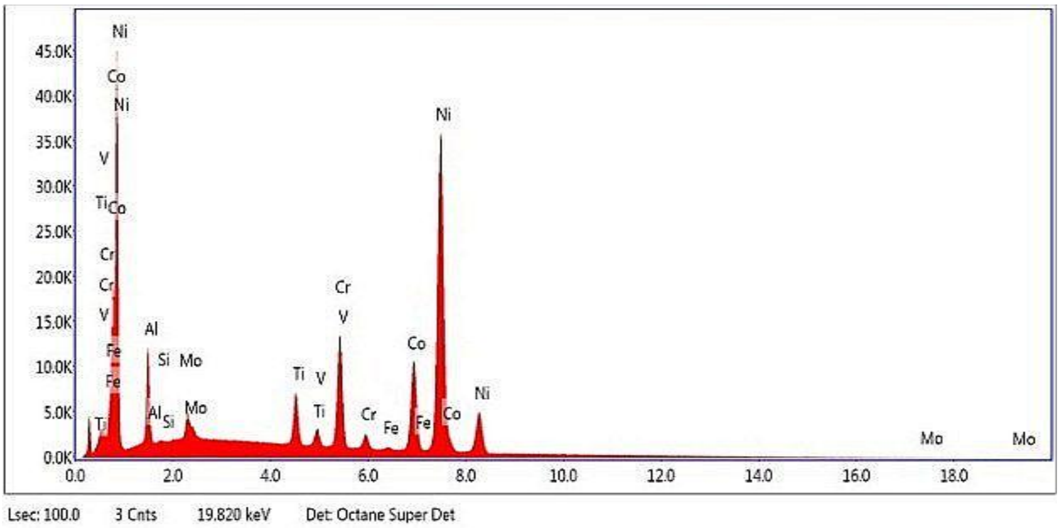

Figure 4. 67: EDS spectrum of selected area 3

Table 4.16 indicates the EDS elemental composition of the base for selected areas 1-3, in Figs. 4.65 – 4.67.

Table 4. 16: Elemental composition of the base at selected areas 1-3

Element	AlK	MoL	TiK	VK	CrK	FeK	CoK	NiK
% Weight Selected Grain Area 1	5.1	2.0	3.7	0.8	9.8	0.3	14.9	62.7
% Weight Selected Grain Area 2	5.3	2.0	4.6	0.8	9.1	0.3	14.2	63.8
% Weight Selected Grain Area 3	5.2	2.0	3.4	0.9	9.6	0.4	15.0	63.5

Further within the base in the depleted zone too, phases had formed as illustrated by the sets of selected areas pairing within the grains in Fig. 4.68. Selected areas 1 and 2 in Figs. 4.69 and 4.70, selected areas 3 and 4 in Figs. 4.71 and 4.72, selected areas 5 and 6 in Figs. 4.73 and 4.74, and, selected areas 7 and 8 in Figs. 4.75 and 4.76. Their spectra however reported averagely similar quantities of material composition, an indicator of uniform aging of material in that region. Active inward Al and outward Ni diffusions were evident. No traces of oxidation were noted, with primary MC carbides evenly distributed throughout the region.

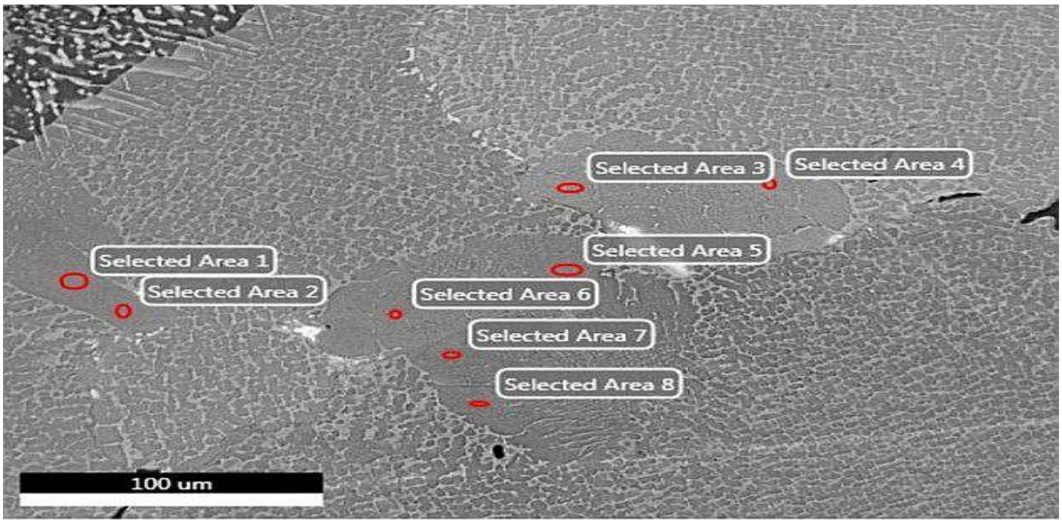

Figure 4. 68: Sectioned base; phases within the depleted zone in the grain

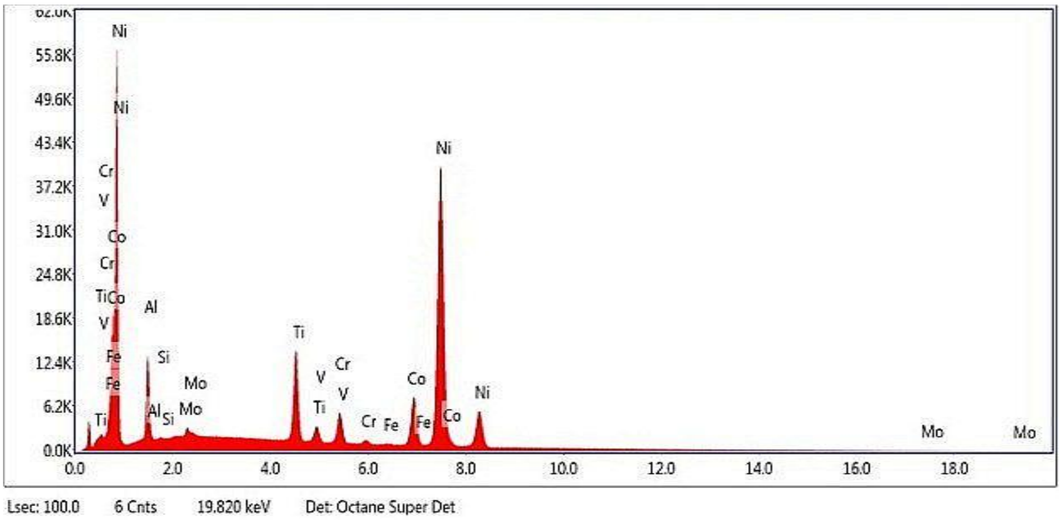

Figure 4. 69: EDS spectrum of selected area 1

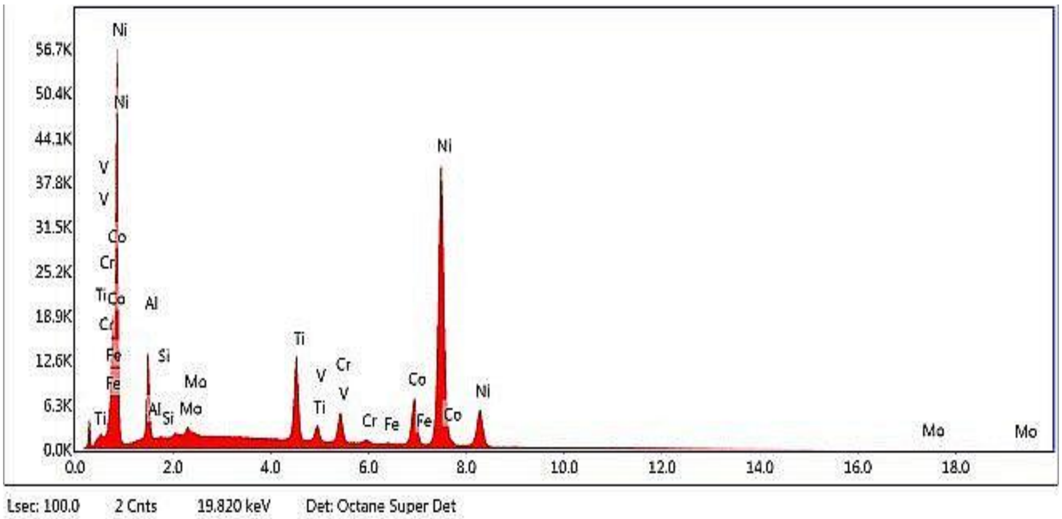

Figure 4. 70: EDS spectrum of selected area 2

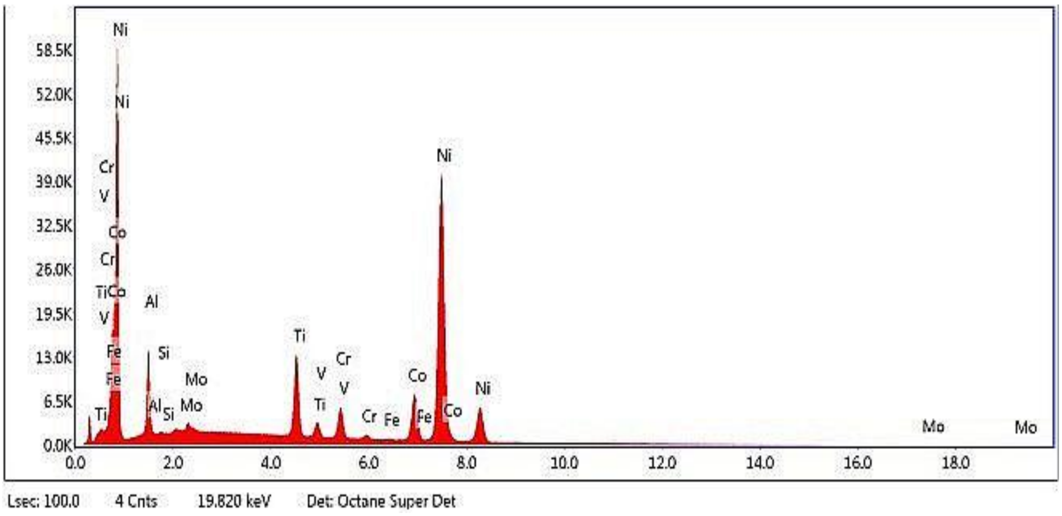

Figure 4. 71: EDS spectrum of selected area 3

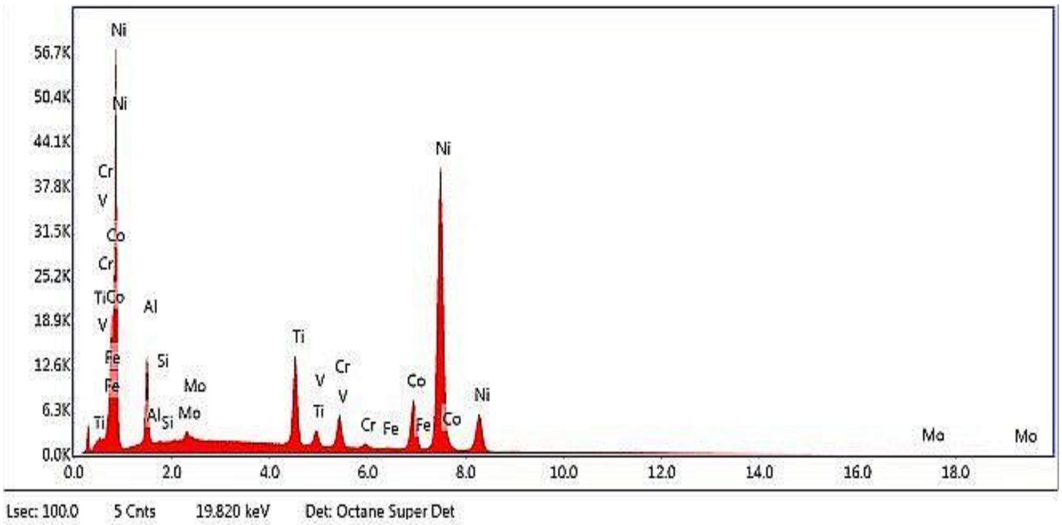

Figure 4. 72: EDS spectrum of selected area 4

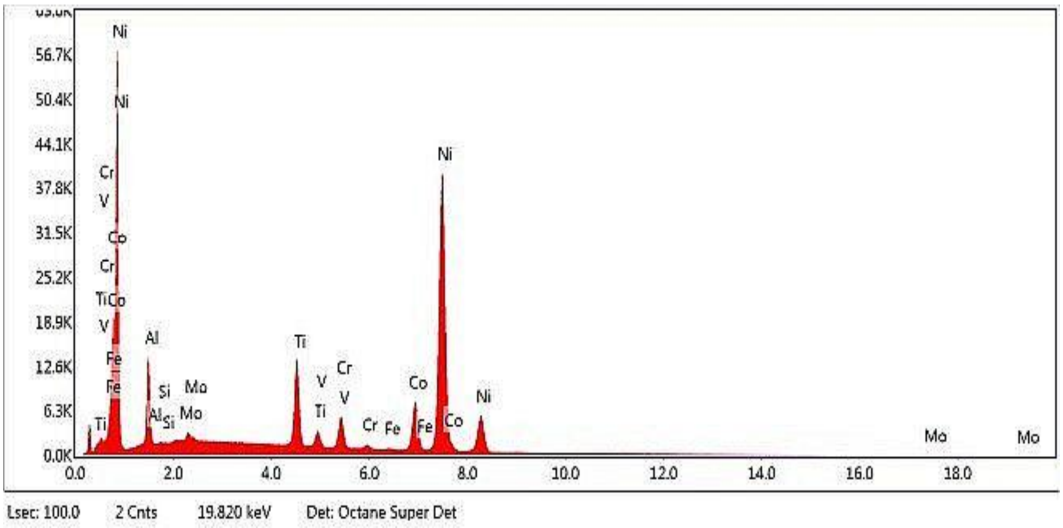

Figure 4. 73: EDS spectrum of selected area 5

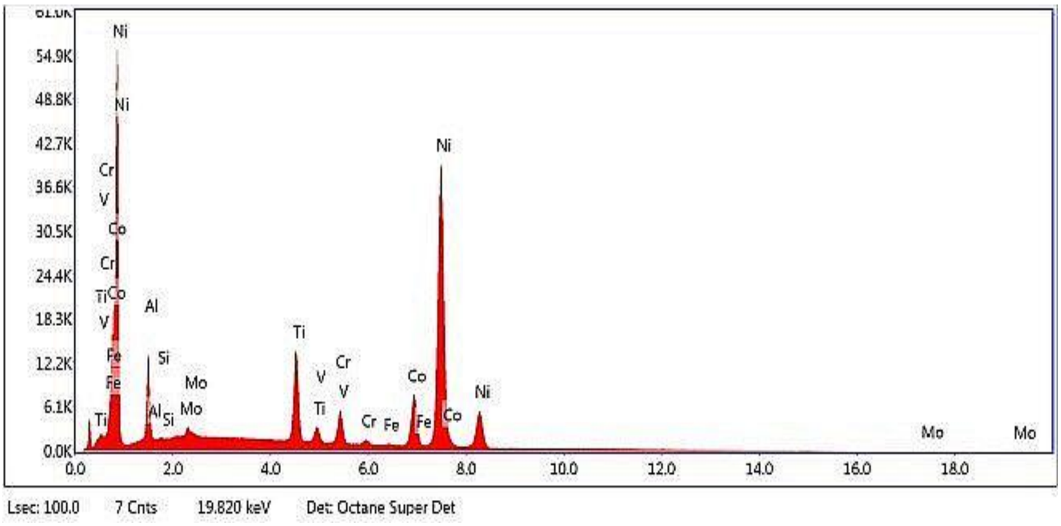

Figure 4. 74: EDS spectrum of selected area 6

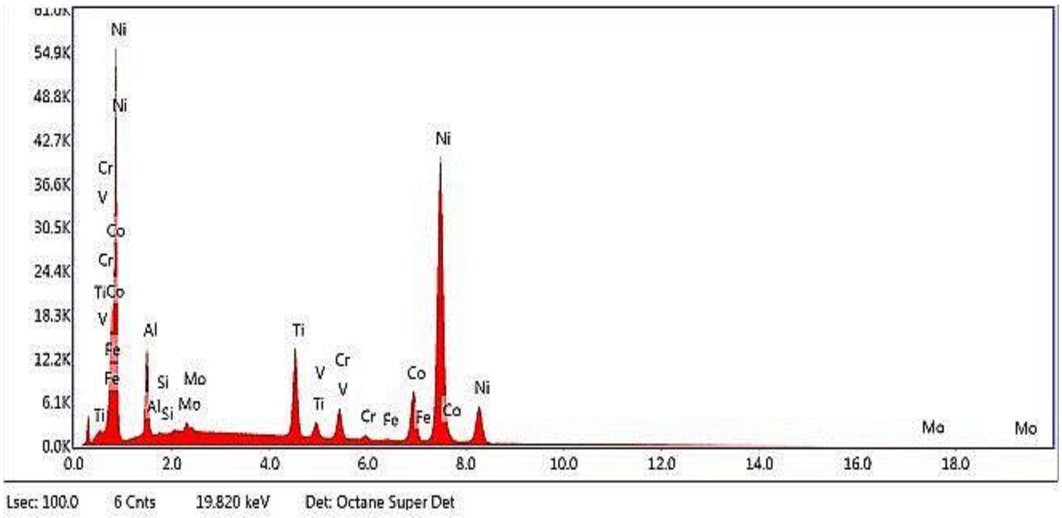

Figure 4. 75: EDS spectrum of selected area 7

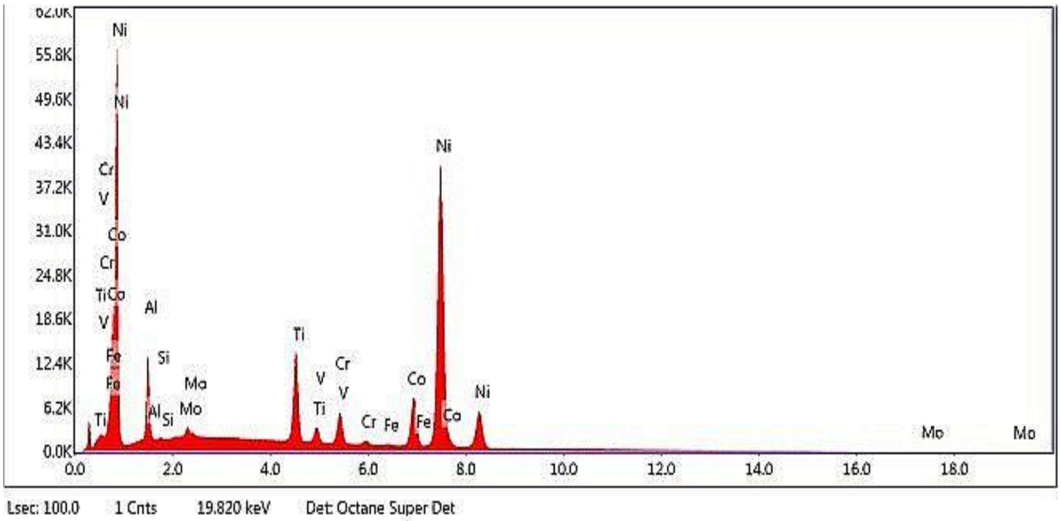

Figure 4. 76: EDS spectrum of selected area 8

Table 4.17 depicts the EDS elemental composition of the base for selected areas 1-8, in Figs. 4.69 – 4.76.

Table 4. 17: Elemental composition of the base at selected areas 1-8

Element	**AlK**	**MoL**	**TiK**	**VK**	**CrK**	**FeK**	**CoK**	**NiK**
% Weight Selected Area 1	6.1	0.8	7.6	0.6	3.4	0.2	10.1	71.4
% Weight Selected Area 2	6.3	0.8	7.0	0.6	3.2	0.2	9.6	72.2
% Weight Selected Area 3	6.5	0.9	7.0	0.6	3.5	0.2	10.1	71.3
% Weight Selected Area 4	6.2	0.8	7.5	0.5	3.3	0.1	10.1	71.6
% Weight Selected Area 5	6.3	0.8	7.2	0.6	3.4	0.2	10.1	71.4
% Weight Selected Area 6	6.1	0.8	7.4	0.6	3.4	0.2	10.5	71.1
% Weight Selected Area 7	6.1	0.8	7.2	0.6	3.2	0.2	10.3	71.6
% Weight Selected Area 8	6.0	0.8	7.3	0.5	3.4	0.2	10.1	71.6

4.7. Closure

Chapter 4 investigated the microstructural and metallurgical degradation of the protective coating as well substrate material of CT blades. The XRF results affirmed the existence of the bulk base elements from the manufacturers' specification, while the XRD analyses enabled positive identification of the resultant compounds that constituted both the diffusion aluminide protective coating as well as the substrate material after exposure to service. The EDS-SEM results established that the protective coating at the tips had been greatly damaged compared to the airfoils and the bases. The pores at the bases of the CT blades were found not influence distribution of uniform cuboidal phase at the bases in comparison the rafted tips and airfoils. This confirmed that degradation of the substrate material occurred as a result of creep and fatigue and not from manufacturing defects. The following chapter reports mechanical testing to evaluate the residual strength of the CT blade at time of retire from service.

CHAPTER 5: DETERMINATION OF MECHANICAL STRENGTH OF RETIRED CT BLADES

5.1. Preamble

This chapter presents mechanical testing to ascertain the strength of the CT blade samples in context at the time of their premature retire. An overview of the procedure is outlined, sample preparation and data collection discussed, and results thereof presented.

5.2. Microhardness testing

Strength analysis is a key factor in assessing health status of CT blades. Nonetheless, HP, PT6A-114A CT blades present a whole new challenge in extracting this vital data. Owing to the complexity in profile and their relatively small sizes to allow preparation of a geometrically standard specimen, micro-hardness testing provided a rather perfect match for strength information (Barbosa et al., 2005; Juliš et al., 2010; Kargarnejad et al., 2012; Ngoret et al., 2016).

In practice, there exist a number of methods that could be employed to determine material hardness. However, the robustness, accuracy and versatility of application to a vast array of alloy, makes Vickers micro hardness a technique of choice (Chicot et al., 2007). Moreover, the experimental hardness value (HV) thereof obtained and as depicted in Eq. 5.1 (Oliver et al., 2004) could be used to evaluate the Youngs' Modulus of the CT blade material (Antunes et al., 2002).

$$HV = {}^{F}\!\big/_{A_{AC}} = {}^{F}\!\Big/_{d^2/2.Sin\left({}^{\varphi}\!/_{2}\right)} = {}^{2FSin\,{}^{136°}\!/_{2}}\!\Big/_{d^2} \approx 1.8544\,{}^{F}\!\big/_{d^2} \qquad 5.1$$

Where F is the applied force in N, A_{AC} is the actual area of contact between the indenter and the surface of the material in mm^2, φ is the angle between the two opposite sides of the diamond square pyramid =136° while d is the arithmetic mean of the length of the two diagonals of the indentation, in mm.

Equivalent yield strength of a sample material specimen can then be approximated by Eq. 5.2 (Mareš et al., 2017) in MPa.

$$\sigma_u \approx HV * c \approx 0.3 \qquad 5.2$$

Where the c is dependent on the geometry of the test material specimen, typically lying in the ranges of between 2-4.

5.2.1. Sample preparation

Both the transverse as well as the longitudinal CT blades specimens which had been initially prepared in the microstructural and metallurgical investigations in section 4.3.3 in conformity to ASTM E3-11 were used in these experiments.

5.2.2. Loading and data collection

Innovatest, Nexus 4000TM, Vickers micro-hardness tester equipped with a microscope, captured in Fig. 5.1 was used for data acquisition.

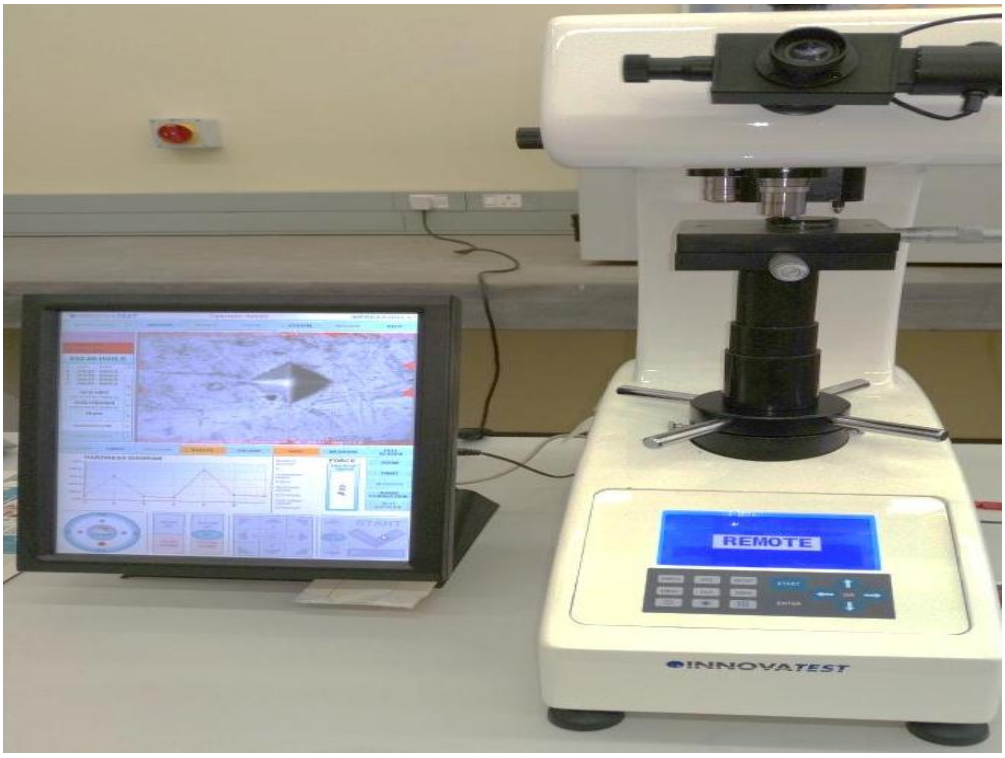

Figure 5. 1: Innovatest Nexus 4000TM, Vickers micro-hardness tester

In conformity with ASTM E384, a load of 500 g force was administered with a dwell time of 10 seconds for each application. Data for the transverse sections were taken at heights of $33.3\%, 66.7\%\ and\ 83.3\%$; the tip, airfoil and base of the CT blade from the root, corresponding to the longitudinal data points. In order to increase accuracy, reliability and statistical significance of collected data, for each section of the tip, airfoil and base, five indentations were taken on each of the surfaces.

5.3. Results and discussions

The experimental results for the transverse sections are captured in Table 5.1 while those for the longitudinal section are conveyed in Table 5.2.

Table 5. 1: Results of the transverse sections

Tip	**Test 1**	**Test 2**	**Test 3**	**Test 4**	**Test 5**	**Average**	**Equivalent Yield Strength**
Diagonal 1	0.0537	0.0537	0.0542	0.0545	0.0584		
Diagonal 2	0.0504	0.0542	0.0549	0.0544	0.0501		
Vickers No.	316.11	318.39	311.42	312.94	315.02	314.78 [2.72]	3078 MPa
Airfoil							
Diagonal 1	0.0515	0.0524	0.0525	0.0518	0.0514		
Diagonal 2	0.0528	0.0523	0.0525	0.0528	0.0532		
Vickers No.	340.64	338.11	336.45	339.10	339.77	338.81 [1.61]	3323 Mpa
Base							
Diagonal 1	0.0511	0.0519	0.0506	0.0512	0.0512		
Diagonal 2	0.0519	0.0512	0.0524	0.0519	0.0513		
Vickers No.	350.10	348.40	349.49	348.67	352.36	349.80 [1.58]	3430 MPa

[*] – Standard Deviation

Table 5. 2: Results of the longitudinal section

Tip	**Test 1**	**Test 2**	**Test 3**	**Test 4**	**Test 5**	**Average**	**Equivalent Yield Strength**
Diagonal 1	0.0542	0.0526	0.0539	0.0521	0.0527		
Diagonal 2	0.0517	0.0534	0.0526	0.0536	0.0535		
Vickers No.	330.35	330.07	326.81	331.46	329.29	329.60 [1.74]	3232 MPa
Airfoil							
Diagonal 1	0.0515	0.0534	0.0522	0.0519	0.0523		
Diagonal 2	0.0526	0.0513	0.0521	0.0527	0.0519		
Vickers No.	342.01	338.45	340.82	339.33	341.38	340.40 [1.47]	3338 MPa
Base							
Diagonal 1	0.0517	0.0505	0.0521	0.0491	0.0514		
Diagonal 2	0.0508	0.0522	0.0506	0.0535	0.0513		
Vickers No.	352.71	351.76	351.91	352.37	351.75	352.10 [0.42]	3453 MPa

[*] – Standard Deviation

In either of the cases, the results depicted that strength of the CT blades material decreased upward from the base towards the tip. The average hardness values, standard deviation and corresponding strength values for transverse sections at the tip, airfoil and base were HV 314.78 [2.72] = 3078 MPa, HV 338.81 [1.61] = 3323 MPa and HV 349.80 [1.58] = 3430 MPa respectively. Likewise, the results for the longitudinal section at the tip, airfoil and base were HV 329.60 [1.74] = 3232 MPa, HV 340.40 [1.47] = 3338 MPa and HV 352.10 [0.42] = 3453 MPa respectively.

A comparison was drawn between experimental HVs and the manufacturer's original specification HV 440 for Ni-base super alloy CT blades (Barbosa et al., 2005) before exposure to service. It was deduced that for the transverse sections; the strengths of the CT blade had fallen by 28.5%, 23% and 20.5% at the tip, airfoil and base respectively. For the longitudinal section on the other hand, in a similar fashion a drop of 25.1%, 22.6% and 20% for the tip, airfoil and base respectively was observed as presented in Fig. 5.2.

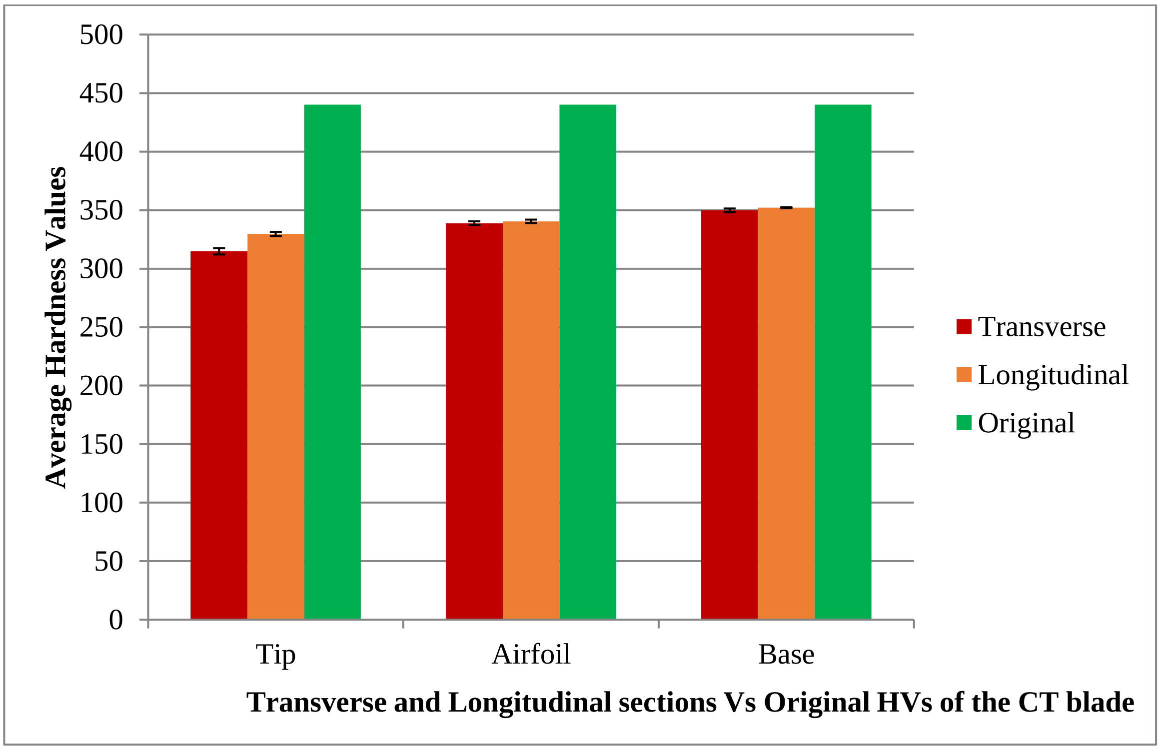

Figure 5. 2: Average hardness values of the transverse and longitudinal sections in comparison to the manufacturer's original specification

The relatively lower HV and consequently the residual strength at the tips relative to the airfoil and the base, could have been prompted by the severity of heat at the tip in operation compared to the airfoil and the base as was evident from temperature distribution results in modeling. In a similar fashion, the microstructure and metallurgical characterization attested to of the rigorous deterioration at the tips in comparison to the airfoil and the base.

To augment the strength of Inconel 713 LC, the thermal expansion coefficient of the substrate material needs to be boosted to enable higher thermal handling capabilities by the CT blades. In conformity to literature, this could be achieved by inclusion and variation of refractory elements in the chemical composition of the substrate material such as ruthenium, iridium, rhenium and among others (Murakami et al., 2000; Pyczak et al., 2004; Siebörger et al., 2001).

Literature also identifies that an increasing the percentage of carbon content in the substrate material and heat treatment during manufacture could make the material better creep resistant too (Barbosa et al., 2005). However, the treated samples may increase carbide networking and void formation within the substrate material, in turn affect the profile of protective coating.

Ultimately, use of smart protective coatings with greater integrity and adoption of advanced application techniques could significantly increase longevity of CT blade material and consequently the strength.

5.4. Closure

Chapter 5 presented mechanical testing to determine mechanical strength of the retired CT blade samples. Although the experiments indicated that the tested materials were still of reasonably high strength, in the ranges of 71.5%-80%, in the weakest and strongest regions respectively, the CT blades could not warranty continued exploitation since pronounced damage on the protective coating especially at the tips had been noted from the microstructural and metallurgical characterization. The final and concluding chapter follows next.

CHAPTER 6: CONCLUSION

6.1. Preamble

In this thesis, characteristic influence of thermo-mechanical stresses occasioning premature failure of HP CT blades for short-haul aircraft fleet was investigated from an assimilative approach. Review of literature had revealed that it was necessary to have a more robust, safety-guaranteed, reliable and cost-effective technique to investigate degradation of CT blade material. In the current work, the CT blade was modeled in an environment that mimics the operational conditions, detailed characterization of the microstructure was done and experiments conducted to ascertain residual strength of the retired CT blades. This concluding chapter thus reports on validation of the methods used in research against the manufacturer's specifications and actual operational data, it summarizes the contributions made to the body of knowledge and outlines the scope of future work.

6.2. Validation of the findings in research against manufacturer's specifications and actual operational data

The manufacturer recommends that PT6A-114A engine HP CT blades operate for 5000 creep-fatigue hours when newly installed, and 3000 creep-fatigue hours after OVH for a period of up to 18000 creep-fatigue hours before their eventual removal. BHSI were to be conducted after every 400 hours to further ascertain their status. Random and unscheduled inspections were to be instituted after 10800 creep-fatigue hours to closely monitor their deterioration every now and then (North Star Turbines, 2016). With this available data and making comparison to the premature retire service time of 6378 creep-fatigue hours of the CT blades in research as presented by the operator, the selected CT blades must have undergone an OVH and were in the second phase of service. Similarly, the CT blades must have been subjected to at least three BHSI and served for a total of only 59.1% of their life expectancy. In light of this therefore:

The modeling results revealed that in the transient regime; the most thermo-mechanically stressed phase of flight, the CT blades could have still served for another approximately 1.44% of the actual life. The author however opines that for utmost safety of short-haul aircraft fleet, considering the possibility of in adherence to the engine's set operation limits, long and overexploitation of engine and not sticking to flight environments set for engine operations, that, when OVH is due, random and unscheduled inspections should immediately commence.

Microstructure of the new CT blade material is a near perfect cuboidal phase (Pollock et al., 2006; Shourangiz et al., 2016). However, from exposure to the harsh thermo-mechanical environment, the cuboidal phase on the CT blade was already damaged, noticeably with greater attack at the tips, lesser at the airfoils, and least at the base. This is in agreement with the modeling results which depicted that the tips experienced highest heat concentration which was decreasing towards the airfoil and the base. Affirmation of hot corrosion and pitting were also pronounced at the tips and decreased towards the airfoils and the base respectively. The cracked and disintegrated diffusive aluminide protective coating was more at the tips and decreased towards the bases, sufficient attestation of premature failure.

The hardness value for a typically new CT blade material is in the range of HV 440, translating to strength values of approximately 4315 MPa. The average hardness values and corresponding strength values for the transverse sections at the; tip, airfoil and base were HV 314.78 [2.72] = 3078 MPa, HV 338.81 [1.61] = 3323 MPa and HV 349.80 [1.58] = 3430 MPa. For the longitudinal section; the tip, airfoil and base are HV 329.60 [1.74] = 3232 MPa, HV 340.40 [1.47] = 3338 MPa and HV 352.10 [0.42] = 3453 MPa. Despite the CT blades being of high strength values, in the ranges of 71.5% at the tips and 80 % at the bases of the CT blades, the material could not warranty continuity of service and posed a potential safety threat on such high flight turnover aircraft. This submitted that OVH might not have added much value in lengthening the service life of the CT blades.

From this research, the author found out that the compromised integrity of the diffusion aluminide protective coating played a key role on degradation of the substrate material.

6.3. Objective Conclusions

The following conclusions have been drawn from each specific objective and are summed up as follows;

Objective 1: To review the techniques currently used to investigate CT blade material degradation.

Objective 1 was comprehensively discussed in Chapter 2. It alludes that monitoring of protective coating and substrate material of the CT blades is crucial to avert un forewarned catastrophic failures and maintain their health status. The techniques used to investigate degradation in CT blade material could be classified as; optical methods, microstructural-metallurgical approaches, use of sensors, experimental approaches, numerical modeling approaches, probabilistic-modeling approaches, statistical modeling approaches, reliability modeling approaches and vibro-modeling approaches. Synthesis through literature reveals that:

1. Current techniques used to investigate failure of CT blades either estimate the life or only inform of after exposure to service with hardly any information accounting for numerous premature failures. As such, the health of CT blade material; the real-time material status, the magnitude of accrued damage and the RUL cannot be told.

2. Very little work has been done on assimilating existing and new techniques to investigate degradation of CT blade material.

3. In this regard, current research opted to assimilate FEA, microstructure and metallurgical studies as well as mechanical testing, to offer a more formidable, robust and an easy to adopt approach in CT blade material investigations. This will enhance safety, increases operational availability of aircrafts and make planning for maintenance easier.

Objective 2: To model, extract and evaluate thermo-mechanical degradation on the CT blade using finite element analysis (FEA).

The results to objective 2 which are investigated in Chapter 3 and depicted that thermal stresses were concentrated on the leading edge than the trailing edge. The tips were seemingly too greatly affected as compared to the airfoil and the base. Stress and strain concentration were centered at the leading-edge joint between the airfoil and the base as a result of rotational speeds. The results further suggested that the CT blade could have served for another 1.44% of the actual life it was in service. However, their premature degradation could have been occasioned by; long and over exploitation of engine, in adherence to the exploitation limits of the engine and changes in flight environments which potentially could have accelerated the degradation process.

Objective 3: To characterize microstructural and metallurgical degradation of the protective coating and the substrate material of the CT blades using XRF, XRD and EDS-SEM.

This objective was investigated in Chapter 4 from various microstructural and metallurgical approaches; the XRF, the XRD and EDS-SEM. The XRF results affirmed the existence of the bulk base elements from the manufacturers' specification, while the XRD analyses enabled positive identification of the resultant compounds that constituted both the diffusion aluminide protective coating as well as the substrate material after exposure to service. The EDS-SEM results established that the protective coating at the tips had been greatly damaged compared to the airfoils and the bases. The pores at the bases of the CT blades were found not influence distribution of uniform cuboidal phase at the bases in comparison the rafted tips and airfoils. This confirmed that degradation of the substrate material occurred as a result of creep and fatigue and not from manufacturing defects.

Objective 4: To determine mechanical strength of the prematurely retired CT blades.

This objective is presented in Chapter 5. The experimental results indicated that although the tested materials were still of reasonably high strength, in the ranges of 71.5%-80%, in the weakest and strongest regions respectively, the CT blades could not warranty continued exploitation since pronounced damage on the protective coating especially at the tips had been noted from the microstructural and metallurgical characterization.

Objective 5: To validate the research results against the manufacturer's specifications and actual operator's data.

The results of assimilative approach used in the current research was weighed against the manufacturer's specifications and actual operator's data and are as detailed in this very same Chapter 6, section 6.2.

6.4. Contributions to pool of knowledge

Thermo-mechanical degradation of HP, PT6A-114A engine CT blade was modeled in an environment that mimics the actual operational conditions for the first time in order to comprehend the reasons for their premature failure.

This research has immensely contributed a large amount of research data to the existing body of knowledge and also shown a new dimension for investigation of failure mode analysis and characterization of CT blade materials.

6.5. Challenges encountered in the course of the Study

In realization of this research, the following challenges were encountered:

1. Prohibitive cost of new CT blades to enable Fatigue-Creep analyses to be conducted.
2. Quite a significant amount of time was spent on sourcing for funds to purchase the samples as CT blades are typically expensive.
3. Equipment to be used for various complex strength tests are expensive to buy and hire, limiting variety of experiments from being explored.

6.6. Future Work

To enhance accuracy in application of the assimilative approach to investigate CT blade material degradation, the author proposes that:

1. An investigation in the role played by other minute factors such as; vibration, flexural loads and aerodynamic stresses on CT blade material degradation.

2. In future a time step analysis-based study be applied to explore the combined degradation of all phases of flight, as in the current research, the transient regime was modeled to represent the most aggressively stressed phase of flight.
3. Further research should be carried out to explore ways of lengthening the life of the protective coating and substrate material to enhance thermal expansion coefficient, oxidation and corrosion resistance.
4. This study be extended to medium and long-haul fleets in future.

6.7. Closure

This chapter is dedicated to summarize the work conducted in current research; validating the modeling, characterization and residual strength results of the CT blades against the manufacturer's specifications and operator's data. A summary of the individual objectives, contributions to the body of knowledge has been drawn and the recommendations for future work are outlined.

BIBLIOGRAPHY

Aero Assurance. (2015). Micro FOD: Cessna 208B Grand Caravan Engine Failure & Forced Landing. Retrieved 05/07, 2016, from http://aerossurance.com/wp-content/uploads/2015/11/pt6-ct.jpg

Antunes, J., Cavaleiro, A., Menezes, L., Simoes, M., & Fernandes, J. (2002). Ultra-microhardness testing procedure with Vickers indenter. *Surface and Coatings Technology, 149*(1), 27-35.

Bai, C.-Y., Luo, Y.-J., & Koo, C.-H. (2004). Improvement of high temperature oxidation and corrosion resistance of superalloy IN-738LC by pack cementation. *Surface and Coatings Technology, 183*(1), 74-88.

Balikci, E., & Raman, A. (2000). Characteristics of the γ′ precipitates at high temperatures in Ni-base polycrystalline superalloy IN738LC. *Journal of Materials Science, 35*, 3593-3597.

Barbosa, C., Nascimento, J., Caminha, I., & Abud, I. (2005). Microstructural aspects of the failure analysis of nickel base superalloys components. *Engineering Failure Analysis, 12*, 348-361.

Becker, W. T., Shipley, R. J., Lampman, S. R., Sanders, B. R., Anton, G. J., Hrivnak, N., . . . Henry, S. D. (2002). ASM handbook. *Failure analysis and prevention, 11*, 1072.

Bovsunovskii, A., & Bovsunovskii, O. (2010). Application of nonlinear resonances for the diagnostics of closing cracks in rodlike elements. *Strength of materials, 42*(3), 331-343.

Bovsunovsky, A., & Surace, C. (2015). Non-linearities in the vibrations of elastic structures with a closing crack: A state of the art review. *Mechanical Systems and Signal Processing, 62*, 129-148.

Boyce, M. P. (2011). *Gas turbine engineering handbook*: Elsevier.

Broda, D., Staszewski, W., Martowicz, A., Uhl, T., & Silberschmidt, V. (2014). Modelling of nonlinear crack–wave interactions for damage detection based on ultrasound—a review. *Journal of Sound and Vibration, 333*(4), 1097-1118.

Bryg, D. J., Mink, G., & Jaw, L. C. (2008). *Combining Lead Functions and Logistic Regression for Predicting Failures on an Aircraft Engine.* Paper presented at the ASME Turbo Expo 2008: Power for Land, Sea, and Air.

Byington, C. S., & Roemer, M. J. (2002). *Prognostic enhancements to diagnostic systems for improved condition-based maintenance [military aircraft].* Paper presented at the Aerospace Conference Proceedings, 2002. IEEE.

Callister, W., & Rethwisch, D. G. (2011). Materials Science and Engineering, eight ed: Wiley.

Cardwell, D., Chana, K., & Russhard, P. (2008). *The Use of Eddy Current Sensors for the Measurement of Rotor Blade Tip Timing: Sensor Development and Engine Testing.* Paper presented at the ASME Turbo Expo 2008: Power for Land, Sea, and Air.

Carter, T. J. (2005). Common failures in gas turbine blades. *Engineering Failure Analysis, 12*, 237-247.

Chen, Chen, & Dong. (2013). Chirplet Wigner–Ville distribution for time–frequency representation and its application. *Mechanical Systems and Signal Processing, 41*(1), 1-13.

Chen, Jie, Patton, & J, R. (2012). *Robust model-based fault diagnosis for dynamic systems* (Vol. 3): Springer Science & Business Media.

Chicot, D., Mercier, D., Roudet, F., Silva, K., Staia, M., & Lesage, J. (2007). Comparison of instrumented Knoop and Vickers hardness measurements on various soft materials and hard ceramics. *Journal of the European Ceramic Society, 27*(4), 1905-1911.

Choi, Y.-S., & Lee, K.-H. (2010). Investigation of blade failure in a gas turbine. *Journal of mechanical science and technology, 24*(10), 1969-1974.

Choux, C., Kulińska, A., & Chevalier, S. (2008). High temperature reactivity of nickel aluminide diffusion coatings. *Intermetallics, 16*(1), 1-9.

Cookson, R., & Haslam, A. (2008). Mechanical design of turbomachinery. *MSc Course Notes, Cranfield University*.

Durand-Charre, M. (2017). *The microstructure of superalloys*: Routledge.

El-Maksoud, R. M. A. (2013). Binary Brayton cycle with two isothermal processes. *Energy Conversion and Management, 73,* 303-308.

El-Sayed, A. F. (2017). *Aircraft propulsion and gas turbine engines*: CRC Press.

Eliaz, N., Shemesh, G., & Latanision, R. (2002). Hot corrosion in gas turbine components. *Engineering Failure Analysis, 9*(1), 31-43.

Evans, A. G., Mumm, D., Hutchinson, J., Meier, G., & Pettit, F. (2001). Mechanisms controlling the durability of thermal barrier coatings. *Progress in Materials Science, 46*(5), 505-553.

Everitt, S. (2012). *Developments in advanced high temperature disc and blade materials for aero-engine gas turbine applications.* University of Southampton.

FCAA. (2014). Accident on 5 September 2010 at Anse-Bertrand (971) to the Cessna 208B registered F-OIXZ operated by Tropic Airlines.

Fei, C., & Bai, G. (2012). Extremum selection method of random variable for nonlinear dynamic reliability analysis of turbine blade deformation. *Propulsion and Power Research, 1*(1), 58-63.

Fernandes, F., Cavaleiro, A., & Loureiro, A. (2012). Oxidation behavior of Ni-based coatings deposited by PTA on gray cast iron. *Surface and Coatings Technology, 207*, 196-203.

Fernandes, F., Lopes, B., Cavaleiro, A., Ramalho, A., & Loureiro, A. (2011). Effect of arc current on microstructure and wear characteristics of a Ni-based coating deposited by PTA on gray cast iron. *Surface and Coatings Technology*, *205*(16), 4094-4106.

Gatto, A., Bassoli, E., & Fornari, M. (2004). Plasma Transferred Arc deposition of powdered high performances alloys: process parameters optimisation as a function of alloy and geometrical configuration. *Surface and Coatings Technology, 187*(2), 265-271.

Gelman, L. (2007). Adaptive time–frequency transform for non-stationary signals with nonlinear polynomial frequency variation. *Mechanical systems and signal processing, 21*(6), 2684-2687.

Gelman, L. (2010). The new frequency response functions for structural health monitoring. *Engineering Structures, 32*(12), 3994-3999.

Gelman, L., Giurgiutiu, V., & Petrunin, I. (2004). Advantage of using the Fourier components pair instead of power spectral density for fatigue crack diagnostics. *International Journal of COMADEM, 7*(2), 18-22.

Gelman, L., & Gorpinich, S. (2000). Non-linear vibroacoustical free oscillation method for crack detection and evaluation. *Mechanical Systems and Signal Processing, 14*(3), 343-351.

Gelman, L., Gorpinich, S., & Thompson, C. (2009). Adaptive diagnosis of the bilinear mechanical systems. *Mechanical systems and signal processing, 23*(5), 1548-1553.

Gelman, L., & Petrunin, I. (2016). THE HIGHER ORDER SPECTRA FOR CONDITION MONITORING/NDT IN NON-STATIONARY CONDITIONS: PART II.

Giggins, C., & Pettit, F. (1980). Corrosion of metals and alloys in mixed gas environments at elevated temperatures. *Oxidation of Metals, 14*(5), 363-413.

Goel, N., Kumar, A., Narasimhan, V., Nayak, A., & Srivastava, A. (2008). *Health risk assessment and prognosis of gas turbine blades by simulation and statistical methods.* Paper presented at the Electrical and Computer Engineering, 2008. CCECE 2008. Canadian Conference on.

Granta, D. (2018). Nickel-chromium alloy, INCONEL 713. 2018, from http://data.grantadesign.com/materialuniverse/metalsandalloys/nickel-chromiumalloy_inconel713l_cast_ascast

Gurrappa, I. (2001). Identification of hot corrosion resistant MCrAlY based bond coatings for gas turbine engine applications. *Surface and Coatings Technology, 139*(2), 272-283.

Hardwicke, C. U., & Lau, Y.-C. (2013). Advances in thermal spray coatings for gas turbines and energy generation: a review. *Journal of Thermal Spray Technology, 22*, 564-576.

Hetmańczyk, M., Swadźba, L., & Mendala, B. (2007). Advanced materials and protective coatings in aero-engines application. *Journal of Achievements in Materials and Manufacturing Engineering, 24*(1), 372-381.

Hou, J., Wicks, B. J., & Antoniou, R. A. (2002). An investigation of fatigue failures of turbine blades in a gas turbine engine by mechanical analysis. *Engineering Failure Analysis, 9*(2), 201-211.

Huang, Z., Wang, Z., Zhu, S., Yuan, F., & Wang, F. (2006). Thermomechanical fatigue behavior and life prediction of a cast nickel-based superalloy. *Materials Science and Engineering: A, 432*, 308-316.

Jaw, L. C. (2005). *Recent advancements in aircraft engine health management (EHM) technologies and recommendations for the next step.* Paper presented at the ASME Turbo Expo 2005: Power for Land, Sea, and Air.

Joly, R., Ogaji, S., Singh, R., & Probert, S. (2004). Gas-turbine diagnostics using artificial neural-networks for a high bypass ratio military turbofan engine. *Applied Energy, 78*(4), 397-418.

Juliš, M., Obrtlík, K., Pospíšilová, S., Podrábský, T., & Poláka, J. (2010). Effect of Al-Si diffusion coating on the fatigue behavior of cast Inconel 713LC at 800 C. *Procedia Eng., 2*, 1983-1989.

Kargarnejad, S., & Djavanroodi, F. (2012). Failure assessment of Nimonic 80A gas turbine blade. *Engineering Failure Analysis, 26*, 211-219.

Kartal, M. E., Başağa, H. B., & Bayraktar, A. (2011). Probabilistic nonlinear analysis of CFR dams by MCS using response surface method. *Applied Mathematical Modelling, 35*(6), 2752-2770.

Khajavi, M., & Shariat, M. (2004). Failure of first stage gas turbine blades. *Engineering Failure Analysis, 11*(4), 589-597.

Kianicová, M. (2009). Microstructural Behaviour of Protective AlSi Coatings under Thermal Load. *Adv. Mil. Technol., 4*, 23-29.

Kim, K. M., Park, J. S., Lee, D. H., Lee, T. W., & Cho, H. H. (2011). Analysis of conjugated heat transfer, stress and failure in a gas turbine blade with circular cooling passages. *Engineering Failure Analysis, 18*(4), 1212-1222.

Kong, C. (2014). Review on Advanced Health Monitoring Methods for Aero Gas Turbines using Model Based Methods and Artificial Intelligent Methods. *International Journal of Aeronautical and Space Sciences, 15*(2), 123-137.

Kontis, P., Yusof, H. M., Pedrazzini, S., Danaie, M., Moore, K., Bagot, P., . . . Reed, R. (2016). On the effect of boron on grain boundary character in a new polycrystalline superalloy. *Acta Materialia, 103*, 688-699.

Kucher, O., Kharyton, V., Laine, J.-P., & Thouverez, F. (2009). Detection of cracked blade from bladed disk forced response using tip-timing method: simulation study. *Авиационно-космическая техника и технология*(7), 155–165-155–165.

Kumar, S., Roy, N., & Ganguli, R. (2007). Monitoring low cycle fatigue damage in turbine blade using vibration characteristics. *Mechanical Systems and Signal Processing, 21*(1), 480-501.

Lee, K. N. (2006). Protective coatings for gas turbines (Vol. 4): Section.

Li, Guo, Wang, Zhang, Gong, & Xu. (2013). Cyclic oxidation of β-NiAl with various reactive element dopants at 1200° C. *Corrosion Science, 66*, 125-135.

Li, & Nilkitsaranont. (2009). Gas turbine performance prognostic for condition-based maintenance. *Applied energy, 86*(10), 2152-2161.

Litt, J. S., Simon, D. L., Garg, S., Guo, T.-H., Mercer, C., Millar, R., . . . Jensen, D. T. (2004). A survey of intelligent control and health management technologies for aircraft propulsion systems. *Journal of Aerospace Computing, Information, and Communication, 1*(12), 543-563.

Liu, L., Jin, T., Zhao, N., Sun, X., Guan, H., & Hu, Z. (2003). Formation of carbides and their effects on stress rupture of a Ni-base single crystal superalloy. *Materials Science and Engineering: A, 361*, 191-197.

Loboda, I., Yepifanov, S., & Feldshteyn, Y. (2007). A generalized fault classification for gas turbine diagnostics at steady states and transients. *Journal of Engineering for Gas Turbines and Power, 129*(4), 977-985.

Locq, D., Caron, P., Ramusat, C., & Mévrel, R. (2011). *Chromium-Based Alloys Strengthened by Ordered Phase Precipitation for Gas Turbine Applications.* Paper presented at the Advanced Materials Research.

Madhavan, S., Jain, R., Sujatha, C., & Sekhar, A. (2014). Vibration based damage detection of rotor blades in a gas turbine engine. *Engineering Failure Analysis, 46*, 26-39.

Mareš, V., Kraus, M., & Podeprelova, A. (2017). *The Effect of Applied Load on Hardness of Steels.* Paper presented at the Materials Science Forum.

Mattingly, J. D. (2002). *Aircraft engine design*: Aiaa.

Matveev, V., & Boginich, O. (2006). Vibrodiagnostic parameters of fatigue damage in rectangular plates. Part 3. Through-the-thickness and surface semi-elliptical cracks. *Strength of materials, 38*(5), 466-480.

Matveev, V., Boginich, O., & Yakovlev, A. (2010). Approximate analytical method for determining the vibration-diagnostic parameter indicating the presence of a crack in a distributed-parameter elastic system at super-and subharmonic resonances. *Strength of materials, 42*(5), 528-543.

Muktinutalapati, N. R. (2011). Materials for gas turbines–an overview *Advances in Gas Turbine Technology*: InTech.

Murakami, H., Honma, T., Koizumi, Y., & Harada, H. (2000). Distribution of platinum group metals in Ni-base single-crystal superalloys. *Superalloys 2000*, 747-756.

Naeem, M. T., Rezamahdi, N., & Jazayeri, S. (2009). Failure analysis of gas turbine blades. *Engineering Technology Opens the Door to a World of Opportunity*, 29.

Natke, H. G., & Cempel, C. (2012). *Model-aided diagnosis of mechanical systems: Fundamentals, detection, localization, assessment*: Springer Science & Business Media.

Ngoret, J. K., & Kommula, V. P. (2016). *Monitoring Material Degradation in Aircraft Turbine Blades: A Comprehensive Survey on Current Techniques.* Paper presented at the Proceedings of Sustainable Research and Innovation Conference.

Nicholls, J. (2003). Advances in coating design for high-performance gas turbines. *MRS Bulletin, 28*(9), 659-670.

Nickel Institute. (2017). Engineering Properties of ALLOY 713C. Retrieved 25/05, 2017, from https://www.nickelinstitute.org/~/media/Files/TechnicalLiterature/Alloy713C_337_.ashx

Nijdam, T., Marijnissen, G., Vergeldt, E., Kloosterman, A., & Sloof, W. (2006). Development of a pre-oxidation treatment to improve the adhesion between thermal barrier coatings and NiCoCrAlY bond coatings. *Oxidation of Metals, 66*(5-6), 269-294.

North Star Turbines. (2016). PT6A Engine. *PT6A Engine.* Retrieved 20/06/2016, 2016, from http://standardaero.com/Engines/PrattWhitney/PT6A.aspx

Oliver, W. C., & Pharr, G. M. (2004). Measurement of hardness and elastic modulus by instrumented indentation: Advances in understanding and refinements to methodology. *Journal of Materials Research, 19*(1), 3-20.

Onyszko, A., & Kubiak, K. (2009). Method for production of single crystal superalloys turbine blades. *Archives of metallurgy and materials, 54*(3), 765-771.

Petrunin, I., & Gelman, L. (2008). Novel optimisation of bicoherence estimation for fatigue monitoring. *Insight-Non-Destructive Testing and Condition Monitoring, 50*(3), 133-135.

Pineau, A., & Antolovich, S. D. (2009). High temperature fatigue of nickel-base superalloys–a review with special emphasis on deformation modes and oxidation. *Engineering Failure Analysis, 16*, 2668-2697.

Pinelli, M., & Venturini, M. (2001). Operating State Historical Data Analysis to Support Gas Turbine Malfunction Detection. *ASME Paper No. IMECE2001/AES-23665*.

Pollock, & Tin, S. (2006). Nickel-based superalloys for advanced turbine engines: chemistry, microstructure and properties. *Journal of Propulsion and Power, 22*, 361-374.

Pollock, T., & Field, R. (2002). Dislocations and high-temperature plastic deformation of superalloy single crystals. *Dislocations in solids, 11*, 547-618.

Pollock, T. M., & Tin, S. (2006). Nickel-based superalloys for advanced turbine engines: chemistry, microstructure and properties. *Journal of Propulsion and Power, 22*(2), 361-374.

Pomeroy, M. (2005). Coatings for gas turbine materials and long term stability issues. *Materials & design, 26*(3), 223-231.

Poręba, M., Ziaja, W., & Kubiak, K. (2008). Microstructure and heat resistance of aluminide coating developed on Rene 77 superalloy in low activity CVD process. *Materials Engineering, 6*, 745-748.

Poursaeidi, E., Aieneravaie, M., & Mohammadi, M. (2008). Failure analysis of a second stage blade in a gas turbine engine. *Engineering Failure Analysis, 15*(8), 1111-1129.

Pratt&Whitney. (2014). Accident on 5 September 2010 at Anse-Bertrand (971) to the Cessna 208B registered F-OIXZ operated by Tropic Airlines.

Procházka, P., & Vaněk, F. (2011). *Contactless diagnostics of turbine blade vibration and damage.* Paper presented at the Journal of Physics: Conference Series.

Pyczak, F., Devrient, B., & Mughrabi, H. (2004). The effects of different alloying elements on the thermal expansion coefficients, lattice constants and misfit of nickel-based superalloys investigated by X-ray diffraction. *Superalloys 2004*, 827-836.

Qin, X., Guo, J., Yuan, C., Chen, C., Hou, J., & Ye, H. (2008). Decomposition of primary MC carbide and its effects on the fracture behaviors of a cast Ni-base superalloy. *Materials Science and Engineering: A, 485*, 74-79.

Qin, X., Guo, J., Yuan, C., Hou, J., & Ye, H. (2008). Thermal stability of primary carbides and carbonitrides in two cast Ni-base superalloys. *Materials Letters, 62*, 2275-2278.

Qin, X., Guo, J., Yuan, C., Hou, J., Zhou, L., & Ye, H. (2012). Long-term thermal exposure responses of the microstructure and properties of a cast Ni-base superalloy. *Materials Science and Engineering: A, 543*, 121-128.

Qin, X., Guo, J. T., Yuan, C., Hou, J. S., & Ye, H. Q. (2007). *Degeneration of primary MC carbide in a cast Ni-base superalloy.* Paper presented at the Materials Science Forum.

Qu, S., Fu, C., Dong, C., Tian, J., & Zhang, Z. (2013). Failure analysis of the 1st stage blades in gas turbine engine. *Engineering Failure Analysis, 32*, 292-303.

Rajendran, R. (2012). Gas turbine coatings–An overview. *Engineering Failure Analysis, 26*, 355-369.

Ramezanpour, R., Ghayour, M., & Ziaei-Rad, S. (2012). Dynamic behavior of Jeffcott rotors with an arbitrary slant crack orientation on the shaft.

Rao, V. N., Kumar, I. N., Madhulata, N., & Abhijeet, A. (2014). Mechanical analysis of 1st stage marine gas turbine blade. *International Journal of Advanced Science and Technology, 68*, 57-64.

Rapp, R. A., & Goto, K. (1981). *The hot corrosion of metals by molten salts.* Paper presented at the Proceedings of the Second International Symposium on Molten Salts.

Red Sky Ventures. (2017). CESSNA MODEL 208B G1000. Retrieved 23/04, 2018, from https://www.redskyventures.org/doc/cessna-poh/Cessna_208_C208B-G1000_Grandcaravan_POH-PIM_2008.pdf

Ricci, R., & Pennacchi, P. (2012). Discussion of the dynamic stability of a multi-degree-of-freedom rotor system affected by a transverse crack. *Mechanism and Machine Theory, 58*, 82-100.

Roemer, M. J., & Kacprzynski, G. J. (2000). *Advanced diagnostics and prognostics for gas turbine engine risk assessment.* Paper presented at the Aerospace Conference Proceedings, 2000 IEEE.

Romessis, C., Kamboukos, P., & Mathioudakis, K. (2007). The use of probabilistic reasoning to improve least squares based gas path diagnostics. *Journal of Engineering for Gas Turbines and Power, 129*(4), 970-976.

Scott-Emuakpor, O., Schwartz, J., George, T., Holycross, C., Cross, C., & Slater, J. (2015). Bending fatigue life characterisation of direct metal laser sintering nickel alloy 718. *Fatigue & Fracture of Engineering Materials & Structures, 38*(9), 1105-1117.

Sexton, L., Lavin, S., Byrne, G., & Kennedy, A. (2002). Laser cladding of aerospace materials. *Journal of Materials Processing Technology, 122*(1), 63-68.

Shourangiz, H. A., Rahmanian, S., Shamsabadi, A., Zare, A., & Zare, I. (2016). Analysis of the Fracture of a Turbine Blade.

Siebörger, D., Brehm, H., Wunderlich, F., Möller, D., & Glatzel, U. (2001). Temperature dependence of lattice parameter, misfit and thermal expansion coefficient of matrix, γ'phase and superalloy. *Zeitschrift fuer Metallkunde, 92*(1), 58-61.

Sieniawski, J. (2003). Nickel and titanium alloys in aircraft turbine engines. *Advances in Manufacturing Science and Technology, 27*(3), 23-33.

Simmons, H. (2004). Root Cause Failure Diagnosis. Retrieved 25th July, 2016, from http://www.swri.org/4org/d18/mechflu/planteng/gasturb/pdfs/simmons.pdf

Simon, D. L. (2010). *Propulsion Diagnostic Method Evaluation Strategy (ProDiMES) User's Guide*: Citeseer.

Simon, D. L., Bird, J., Davison, C., Volponi, A., & Iverson, R. E. (2008). *Benchmarking gas path diagnostic methods: a public approach.* Paper presented at the ASME Turbo Expo 2008: Power for Land, Sea, and Air.

Singh, H., Puri, D., & Prakash, S. (2007). An overview of Na 2 SO 4 and/or V 2 O 5 induced hot corrosion of Fe-and Ni-based superalloys. *Rev. Adv. Mater. Sci, 16*(1-2), 27-50.

Smith, G., & Patel, S. (2005). The role of niobium in wrought precipitation-hardened nickel-base alloys. *Proceedings of Superalloys, 718*, 625-706.

Stamatis, A. G. (2014). Engine Condition Monitoring and Diagnostics: Engine Condition Monitoring and Diagnostics, Progress in Gas Turbine Performance.

Steiner, A. (2000). Techniques for blade tip clearance measurements with capacitive probes. *Measurement Science and Technology, 11*(7), 865.

Stolle, R. (2009). Conventional and advanced coatings for turbine airfoils. *Journal of MTU Aero Engines*(D-90955).

Struers. (2017). Materialographic Consumables Catalogue. Retrieved 30/08, 2017, from http://www.masontechnology.ie/files/documents/stru70.pdf

Sudhangshu, B. (2007). High temperature coatings: Butterworth-Heinnemann, Oxford.

Sujata, M., Madan, M., Raghavendra, K., Venkataswamy, M., & Bhaumik, S. (2010a). Identification of failure mechanisms in nickel base superalloy turbine blades through microstructural study. *Engineering Failure Analysis, 17*(6), 1436-1446.

Sujata, M., Madan, M., Raghavendra, K., Venkataswamy, M., & Bhaumik, S. (2010b). Microstructural study: an aid to determination of failure mechanism in nickel base superalloy blades. *Transactions of the Indian Institute of Metals, 63*(2-3), 681-685.

Szczepanik, R., Rokicki, E., Spychała, J., Kaźmierczak, K., Majewski, P., & Przysowa, R. (2012). *Application of blade-tip sensors to blade-vibration monitoring in gas turbines*: INTECH Open Access Publisher.

Tadayon, A. (2014). *Vibration Analysis of Multi Degree of Freedom Self-excited Systems.* Eastern Mediterranean University (EMU)-Doğu Akdeniz Üniversitesi (DAÜ).

Talbot, D. E., & Talbot, J. D. (2018). *Corrosion science and technology*: CRC press.

Tamarin, Y. (2002). *Protective coatings for turbine blades*: ASM international.

Tappert, P., Von Flotow, A., & Mercadal, M. (2001). *Autonomous PHM with blade-tip-sensors: algorithms and seeded fault experience.* Paper presented at the Aerospace Conference, 2001, IEEE Proceedings.

Tarafder, M., Sujata, M., Ranganath, V., Tarafder, S., & Bhumik, S. (2013). Microstructural damage evaluation in Ni-based superalloy gas turbine blades by fractal analysis. *Procedia Engineering, 55*, 289-294.

Thulin, R. D., Howe, D. C., & Singer, I. D. (1982). Energy efficient engine high-pressure turbine detailed design report.

Vakhtin, A. B., Chen, S.-J., & Massick, S. M. (2009). *Optical probe for monitoring blade tip clearance.* Paper presented at the 47th AIAA Aerospace Sciences Meeting Including The New Horizons Forum and Aerospace Exposition.

Von Flotow, A., Mercadal, M., & Tappert, P. (2000). *Health monitoring and prognostics of blades and disks with blade tip sensors.* Paper presented at the Aerospace Conference Proceedings, 2000 IEEE.

Wang, Q., Wu, Y., Ke, P., Cao, H., Gong, J., Sun, C., & Wen, L. (2004). Hot corrosion behavior of AIP NiCoCrAlY (SiB) coatings on nickel base superalloys. *Surface and Coatings Technology, 186*(3), 389-397.

Witek, L. (2011). Crack propagation analysis of mechanically damaged compressor blades subjected to high cycle fatigue. *Engineering Failure Analysis, 18*(4), 1223-1232.

Witoś, M., & Szczepanik, R. (2009). *Turbine engine health/Maintenance status monitoring with use of phase-discrete method of blade vibration monitoring.* Paper presented at the Solid State Phenomena.

Wu, Z., Qi, Z., Jiang, W., Wang, Z., & Liu, B. (2014). Influence of niobium addition on microstructure, mechanical properties and oxidation resistance of ZrN coatings. *Thin Solid Films, 570*, 256-261.

Yan, B., Zhang, J., & Lou, L. (2008). Effect of boron additions on the microstructure and transverse properties of a directionally solidified superalloy. *Materials Science and Engineering: A, 474*, 39-47.

Yang, Y., Peng, Z., Meng G, & Zhang WM. (2012). Characterize highly oscillating frequency modulation using generalized Warblet transform. *Mechanical Systems and Signal Processing, 26*, 128-140.

Yavorska, M., Poręba, M., & Sieniawski, J. (2008). Development of microstructure of aluminide layer on Ni-base superalloys in the low-activity CVD process. *Materials Engineering, 6*, 749-752.

Yeh, J.-W. (2013). Alloy design strategies and future trends in high-entropy alloys. *JOM Journal of the Minerals Metals and Materials Society, 65*(12), 1759-1771.

Yoo, K. B., & Lee, H. S. (2010). *The microstructure and mechanical properties of Ni-based superalloy after service exposure in gas turbine.* Paper presented at the Materials Science Forum.

Yoshioka, Y., Saito, D., Takaku, R., Itou, S., Sato, I., Ishibashi, K., & Sakai, Y. (2010). Development, reliability evaluation and service experiences of gas turbine blade life regeneration technology. *Transactions of the Indian Institute of Metals, 63*(2-3), 289-295.

Young, D., & Watson, S. (1995). High-temperature corrosion in mixed gas environments. *Oxidation of Metals, 44*(1-2), 239-264.

Zhang, Peng, Dong, Zhang, & Meng. (2016). Location identification of nonlinearities in MDOF systems through order determination of state-space models. *Nonlinear Dynamics*, 1-16.

Zhang, & Zhao. (2016). *Aerospace materials handbook*: CrC Press.

Zhao, X., Chen, J., Lin, X., & Huang, W. (2008). Study on microstructure and mechanical properties of laser rapid forming Inconel 718. *Materials Science and Engineering: A, 478*(1), 119-124.

Zielińska, M., Kubiak, K., & Sieniawski, J. (2009). Surface modification, microstructure and mechanical properties of investment cast superalloy. *Arch. Metall. Mat., 35,* 55-62.

Zielińska, M., Sieniawski, J., Yavorska, M., & Motyka, M. (2011). Influence of chemical composition of nickel based superalloy on the formation of aluminide coatings. *Archives of metallurgy and materials, 56*(1), 193-197.

Žmindák, M., Novák, P., & Nozdrovický, J. (2008). Thermo-mechanical transient analysis of concrete structure around the nuclear reactor.

Zwingenberg, M., Dobrzynski, B., Klumpp, S., Werner, K., & Benra, F.-K. (2012). *Generation of Gas Turbine Component Maps on Basis of Operational Data.* Paper presented at the ASME Turbo Expo 2012: Turbine Technical Conference and Exposition.